Multiscale study of the electric field induced transition in the Mott phase of GaMo4S8 crystals and TaSe2 monolayers

Houda Koussir

University of Lille

Doctoral School ENGSYS Engineering and Systems Sciences

Thesis defended by **Houda KOUSSIR**

Defended on **30thJanuary, 2024**

In order to become Doctor from Université de Lille

Academic Field **Electronics, microelectronics, nanoelectronics and micro-waves**

Multiscale study of the electric field induced transition in the Mott phase of $GaMo_4S_8$ crystals and $TaSe_2$ monolayers

Thesis supervised by Bruno GRANDIDIER Supervisor
Pascale DIENER Co-supervisor

Committee members:

Referees	Marie-Paule BESLAND	Research Director at IMN	
	Christophe BRUN	Researcher at INSP	
Examiners	Xavier WALLART	Research Director at IEMN	Committee President
	Ivan K. SCHULLER	Professor at University of California	
Supervisors	Bruno GRANDIDIER	Research Director CNRS at IEMN	
	Pascale DIENER	Teacher-researcher (HDR) at JUNIA-IEMN	

Université de Lille

Ecole Doctorale ENGSYS Sciences de l'ingénierie et des systèmes

Thèse soutenue par **Houda KOUSSIR**

Soutenue le **30 Janvier 2024**

Pour obtenir le grade de Docteur de l'Université de Lille

Domaine académique **Électronique, microélectronique, nanoélectronique et micro-ondes**

Étude multi-échelle de la transition induite par le champ électrique dans la phase de Mott des cristaux de $GaMo_4S_8$ et des monocouches de $TaSe_2$

Thèse dirigée par	Bruno GRANDIDIER	Directeur de thèse
	Pascale DIENER	Co-directrice

Membres du jury:

Rapporteurs	Marie-Paule BESLAND	Directrice de recherche à IMN	
	Christophe BRUN	Chargé de recherche à INSP	
Examinateurs	Xavier WALLART	Directeur de recherche à IEMN	Président du jury
	Ivan K. SCHULLER	Professeur à l'université de Californie	
Directeurs de thèse	Bruno GRANDIDIER	Directeur de recherche à IEMN	
	Pascale DIENER	Enseignante-chercheuse (HDR) à JUNIA-IEMN	

Contents

Abstract

In the realm of condensed matter physics, Mott insulators are essential for exploring complex electronic phenomena, with significant implications for high-temperature superconductivity and quantum spin liquids. This thesis investigates two types of such materials, distinguished by their dimensionality: $GaMo_4S_8$ crystals and monolayer 1T-$TaSe_2$.

After presenting their properties in the first chapter, the second chapter addresses the local-scale characterization techniques used to characterize both materials, namely scanning tunneling microscopy and spectroscopy for structural and electronic studies, and multi-tip scanning tunneling microscopy for transport measurements. The latter technique was particularly employed to analyze transport in $GaMo_4S_8$. The study then delved into the material's response to external electric fields, examining the threshold electric field in relation to the electrode geometry and exploring the temporal evolution of switching times in connection with inter-electrode distances. The achievement of volatile transitions opens prospects for applications such as the operation of a microneuron at room temperature.

To enhance the control over phase transition properties of Mott insulators, it is beneficial to consider two-dimensional systems where the current flow is restricted within the crystal plane. The final chapter focuses on the 1T phase of $TaSe_2$, epitaxially grown on gallium phosphide (GaP) semiconductor substrates. Low-temperature scanning tunneling microscopy studies reveal that 1T-$TaSe_2$ monolayers exhibit not only the characteristic charge density modulation (Star of David) of the charge density wave phase but also a unique Moiré pattern due to the monolayer interaction with the GaP substrate. Scanning tunneling spectroscopy has identified a bandgap, hallmark of the Mott insulating state. This state is further substantiated by temperature-dependent transport measurements that show the persistence of the insulating phase up to 400 K. Notably, spectroscopic measurements with varying tip-to-surface distances have unveiled insulator to metal transitions at low temperatures. The observation of such transitions suggests that this large-scale heterostructure could be a material of choice for neuromorphic applications.

Résumé

Dans le domaine de la physique de la matière condensée, les isolants de Mott sont essentiels pour explorer des phénomènes électroniques complexes, ayant des implications significatives pour la supraconductivité à haute température et les liquides de spin quantiques. Cette thèse porte sur deux types d'isolants de Mott qui se distinguent l'un de l'autre par leur dimensionalité: des cristaux de $GaMo_4S_8$ et des monocouches de 1T-$TaSe_2$.

Après avoir introduit leurs propriétés dans le premier chapitre, le second chapitre traite des techniques utilisées pour caractériser ces matériaux à l'échelle locale, d'une part la microscopie et spectroscopie à effet tunnel pour mener une étude structurale et électronique et d'autre part la microscopie à effet tunnel à pointes multiples pour effectuer des mesures de transport. Cette dernière technique a notamment servi à analyser le transport dans $GaMo_4S_8$. Nous nous sommes alors intéressés à la réponse du matériau aux champs électriques externes, examinant le champ électrique seuil en fonction de la géométrie des électrodes et explorant l'évolution temporelle des temps de commutation en relation avec les distances inter-électrodes. L'obtention de transitions volatiles ouvre la voie à des applications telles que l'opération d'un microneurone à température ambiante.

Pour mieux contrôler les propriétés de transition de phase des isolants de Mott, il est intéressant de considérer des systèmes bidimensionnels dans lesquels le passage du courant est confiné dans le plan du cristal. Aussi, le dernier chapitre se rapporte à la phase 1T du $TaSe_2$, épitaxiée sur des substrats semi-conducteurs de phosphure de gallium (GaP). Comme le révèle l'étude réalisée par microscopie à effet tunnel à basse température, les monocouches de 1T-$TaSe_2$ ne présentent pas seulement la modulation de la densité de charge (étoile de David) caractéristique de la phase onde de densité de charge, mais aussi un motif de Moiré original dû à l'interaction de la monocouche avec le substrat de GaP. Dans cette phase, caractérisée par spectroscopie tunnel, une bande interdite a été mise en évidence, signature de l'état isolant de Mott à basse température. L'état de Mott est corroboré par des mesures de transport dépendant de la température, qui indiquent la persistance de la phase isolante jusqu'à 400 kelvins. De plus, des mesures spectroscopiques à distance pointe-surface variable ont montré l'existence de transitions isolant-métal à basse température. L'observation de telles transitions permet d'envisager l'utilisation de cette hétérostructure à grande échelle comme candidat potentiel en tant que matériau neuromorphique.

Acknowledgments

A few years back, I could hardly believe that I would make it this far in my academic career. Yet, here I am, having overcome numerous challenges, mostly personal ones.

This journey would not have been possible without the help and guidance of my supervisor, Bruno Grandidier, and my co-supervisor, Pascale Diener. I am profoundly thankful for their support and availability throughout my PhD adventure. I consider myself fortunate to have been part of the amazing physics group at IEMN over the past few years. I want to express my gratitude to the entire group for their invaluable assistance and genuine support.

Maxime Berthe ensured that my experiences with the complex instruments were as smooth and easy as possible. I am also grateful to Nemanja Peric, from whom I learned so much about STM. My gratitude extends to Louis Biadala for his advice and unwavering support for the PhD students in our group. A special thanks to Isabelle Lefebvre for her help with COMSOL, and to Yannick Lambert, with whom I spent significant time working on AFM. Pierre Capiod generously shared his knowledge, enriching my research experience. Additionally, I thank Xavier Wallart from the EPIPHY group for his collaboration on our project.

I must acknowledge Emmanuelle Gillman, Cintia Ayres Pereira, and Nora Benbahlouli for their indispensable administrative assistance.

Living in Lille, far from my family, was made easier thanks to my wonderful colleagues: Yevheniia, Nemanja, Thomas, Louis, Simon, Wijden and Huu Thoai. Thank you all for your support throughout this journey. I also wish the best of luck to the other PhD students in our group, whose presence made stressful periods more bearable.

I would like to express my deepest gratitude to the most important people in my life, my parents, Mina and Lahoucine. Without your unwavering support and love, I would not be the person I am today. Your belief in me has been my greatest source of strength. My younger brothers, Mohamed and Ayoub, have also been pillars of support, always there to lift my spirits. I cannot forget my cousin Naima, whose help was crucial in facilitating my move and stay in France. I am forever grateful to her, as well as to all my family members who have always kept me in their thoughts.

A heartfelt thanks to my friends for their constant presence and endless support. My best friend, Halima, has been with me through the toughest times, always reminding me that it's worth it. My friends in Morocco, Bahija and Ahlam, have not let distance come between us and always remembering me. I am deeply grateful to Kaoutar and Noura for the sake of old times and the wonderful memories we share abroad. Yassine, your unwavering belief in me means a lot to me and has been a constant source of strength and encouragement. And to Zakaria, whose regular check-in calls during the writing of my thesis kept me grounded. Your support and love have been immeasurable.

Introduction

Condensed matter physics has broadened its scope through the study of Mott insulators, a class of materials where electron interactions defy conventional theoretical models, thereby facilitating research into high-temperature superconductivity and quantum spin liquids. These investigations hold substantial promise for advancements in technology, particularly in the development of neuromorphic computing systems. This dissertation investigates the distinct properties of two such materials: $GaMo_4S_8$ crystals and monolayer 1T-$TaSe_2$. Each material is analyzed using specific investigative techniques appropriate to their respective and singular nanoscale behaviors.

The experimental exploration of $GaMo_4S_8$ crsystals has been marked by the deployment of a novel methodological approach, utilizing a sophisticated nanoprobe system. This system's key feature is the inclusion of a scanning electron microscope (SEM), allowing for detailed analysis across a multitude of scales, precisely from 200 nm to 2 μm, within a highly controlled environment. The study meticulously rationalizes the threshold electric field as a function of electrode geometry, integrating these observations with existing theoretical frameworks. Furthermore, it investigates the temporal evolution of the switching time with respect to the inter-electrode distance, engaging in a dialogue with established models. This research also proceeds into the practical realm, demonstrating the operation of a micrometer sized artificial neuron at room temperature.

The study of monolayer 1T-$TaSe_2$ presents the identification of a novel Mott insulator within the $TaSe_2$/GaP system, expanding our understanding beyond the previously studied $TaSe_2$/graphene or HOPG, which is limited to the formation of isolated islands. This research provides a detailed rationalization of the superstructures observed, including Charge Density Waves (CDW), Moiré patterns, and other phenomena down to atomic resolution. Moreover, the investigation delves into the resistive switching mechanisms, elucidating a change in the density of states influenced by the tip effect.

The structure of this thesis is laid out in four chapters, each contributing to the comprehensive narrative of nanoscale Mott insulators. The initial chapters establish the theoretical framework and introduce the experimental techniques that enable precise probing of these materials. The following chapters detail the experimental procedures and findings in $GaMo_4S_8$ crystals and 1T-$TaSe_2$ monolayer.

In terms of future perspectives for $GaMo_4S_8$, this thesis contemplates the characteristic energy of transition, setting the stage for subsequent investigations into this critical parameter. Similarly, for monolayer 1T-$TaSe_2$, these findings pave the way for the application in neuromorphic computing, proposing new avenues for resistive switching technologies, indicative of the material's vast potential in future technological applications.

Chapter 1

State of art

1.1 Mott insulating state

Mott insulators, emerging as a significant subset of quantum materials, challenge traditional understanding in solid-state physics [1]. Rooted in conventional band theory, the electronic properties of materials are predominantly determined by their band structures, especially the relative positions of their valence and conduction bands to the Fermi level.

For Mott insulators, their unique electronic configuration, characterized by an odd number of electrons per unit cell, results in a partially filled electronic band. Conventional band theory posits that materials with a partially filled band should exhibit metallic behavior. This is based on the premise that in such a band, there are unoccupied energy states that electrons can readily occupy, facilitating electrical conductivity. [2].

However, Mott insulators defy conventional expectations. Despite their partially filled bands, they predominantly exhibit insulating behavior. This deviation from conventional understanding prompted deeper investigations into the underlying physics. At the forefront of this exploration was Nevill Francis Mott.

The term "Mott insulator" honors Nevill Francis Mott's seminal mid-20th-century work. He highlighted the shortcomings of the predominant band theory in explaining the insulating behavior of certain transition metal oxides [3]. Mott theorized that intense electron-electron correlations, particularly when the Coulomb repulsion between electrons surpasses the bandwidth, lead to the localization of electrons, giving rise to an insulating state.

Several materials, including transition metal oxides like V_2O_3 and $LaTiO_3$ as well as specific organic systems, have been identified as Mott insulators [4]. A common trait among these materials is the presence of a partially filled electronic band. In the absence of strong electron-electron interactions, this band would facilitate conductivity. However, these interactions give rise to the splitting of the band into two bands, resulting in an energy gap and the observed insulating behavior [5].

To delve deeper into the role of electron-electron interactions and their profound impact on the behavior of materials, it is essential to consider a theoretical framework that captures these complexities.

1.1.1 The Hubbard Model: A framework for understanding electron correlations

Central to the understanding of Mott insulators is the Hubbard model. This theoretical framework describes electrons in a lattice by accounting for their kinetic and interaction energies. The model considers the kinetic energy associated with electrons hopping (represented by the parameter t) between lattice sites and the potential energy due to electron-electron interactions

when they occupy the same site, as seen in Figure 1.1a. When the interaction energy, represented by the parameter U in the model, significantly exceeds the bandwidth, the electrons tend to localize to minimize energy, resulting in an insulating state. This model effectively captures the strong electron-electron correlations observed in Mott insulators and provides a robust foundation for understanding their insulating behavior.

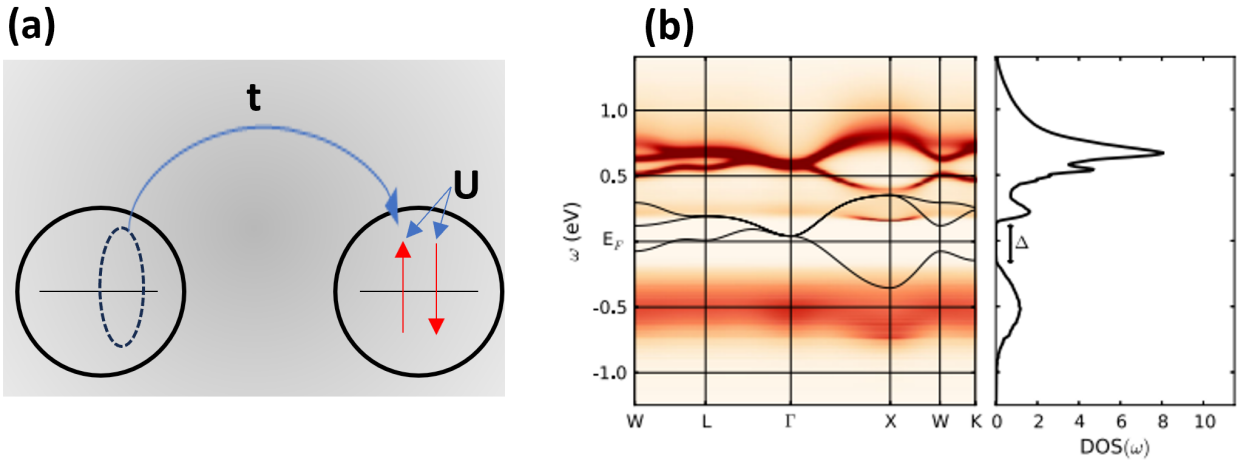

Figure 1.1: (a) Schematic of the parameters entering in the Hubbard model. The circles indicate atomic sites, the red arrows are electrons of spin up and down, t is the hopping term and U is the onsite Coulom interaction. (b) The result of the LDA + DMFT calculations illustrates the emergence of a gap δ due to the on-site Coulomb repulsion (U), characteristic of a Mott insulator; effectively separating the Lower Hubbard Band (LHB) and the Upper Hubbard Band (UHB) [6].

The mathematical representation of the Hubbard model is given by:

$$H = -t \sum_{\langle ij \rangle, \sigma} (c^{\dagger}_{i\sigma} c_{j\sigma} + h.c.) + U \sum_{i} n_{i\uparrow} n_{i\downarrow}$$

Where:

- t represents the hopping parameter, describing the kinetic energy associated with an electron moving from one lattice site to another.
- $c^{\dagger}_{i\sigma}$ and $c_{j\sigma}$ are the creation and annihilation operators, respectively, for an electron with spin σ at lattice sites i and j.
- U is the on-site Coulomb repulsion between electrons of opposite spins when they are on the same lattice site.
- $n_{i\sigma}$ is the number operator, indicating the presence (1) or absence (0) of an electron with spin σ at site i.

This Hamiltonian captures the essence of the Hubbard model, with the first term representing the kinetic energy and the second term depicting the interaction energy.

However, while the Hubbard model offers profound insights, it also comes with its limitations. For instance, the model inherently assumes a perfect lattice and primarily focuses on nearest-neighbor hopping. This means that more intricate lattice structures or interactions that span over longer ranges necessitate modifications of the model.

Furthermore, the model's predictions may not always align with experimental observations for materials where non-local interactions are dominant or where other interactions, such as

electron-phonon couplings, play a pivotal role. Nevertheless, the Hubbard model's strength resides in its ability to simplify complex problems, providing foundational insights into electron correlations.

Solving the Hubbard model, especially in higher dimensions, is not straightforward. Several methods have been employed over the years:

- **Exact Diagonalization (ED):** A technique that numerically diagonalizes the Hamiltonian for small systems. Its application is limited by system size due to the exponential growth of the Hilbert space, making it unsuitable for larger systems.
- **Quantum Monte Carlo (QMC):** A powerful method for various systems, but it faces challenges, specifically the "sign problem" (when positive and negative contributions nearly cancel each other out), when dealing with frustrated systems or systems at finite temperatures.
- **Mean Field Theory:** This approach reduces the many-body problem to a single-particle problem, offering qualitative insights. However, it might miss crucial correlated effects present in strongly interacting systems.
- **Dynamical Mean Field Theory (DMFT):** An extension of the mean field idea, DMFT has, in recent times, merged with first-principles methods to study real materials' electronic properties. Suited for systems with strong local correlations.

DMFT, in particular, has garnered significant attention due to its unique capabilities [7]. Esteemed for its ability to incorporate local quantum fluctuations, DMFT effectively captures the strong local electron correlations prevalent in many materials. The integration of DMFT with first-principles methods like density functional theory (DFT) augments the realism in modeling Mott insulators, thereby bridging the theoretical and experimental realms [8].

Through DMFT, the complex landscape of electron behaviors and phase transitions in Mott insulators is rendered with clarity. The method's precision and adaptability make it a valuable tool for both theoretical and experimental physicists, contributing to the ongoing discourse on the enigmatic nature of Mott insulators [2]. When coupled with LDA (Local Density Approximation), DMFT capturs the complexities of the Mott metal-insulator transition as seen in materials like V_2O_3 and $GaTa_4Se_8$ [6]. As shown in Figure 1.1b, LDA calculations tend to predict a multitude of bands at the Fermi level, obscuring a clear depiction of Hubbard model physics and underscoring the necessity to consider additional factors such as orbital degrees of freedom and electron correlation effects. These strong correlations in $GaTa_4Se_8$ are attributed to the large intercluster distance resulting in narrow partially filled conduction bands.

1.2 Phase transitions in Mott insulators

The transition from an insulating to a metallic state in Mott insulators, often termed as the Mott transition, can be induced by several external stimuli including temperature, pressure, and doping. These stimuli alter the balance between the kinetic and potential energy of the electrons, thereby affecting the electronic correlation and inducing a phase transition. Additionally, the Mott transition can also be triggered by the application of an electric field, a phenomenon that will be extensively discussed in Section 1.3. This transition is fundamental in understanding the rich physics of Mott insulators and has implications for various applications including electronic devices. A schematic of the Mott trnasitions with temperature, pressure and doping, from [9] is shown in Figure 1.2.

1.2.1 Temperature

The Mott transition near the Mott line is distinguished by a unique temperature-dependent phase transition, where the system transitions from a low-temperature paramagnetic metallic phase to a high-temperature paramagnetic insulating phase [10]. This is contrary to conventional transitions in other materials, such as many magnetic transitions, that shift from a low-temperature insulating phase to a high-temperature metallic phase, often accompanied by structural changes. Such transitions are distinctly categorized from Mott transitions, as exemplified in materials like VO_2 at temperatures exceeding 340 K [11].

1.2.2 Pressure

Pressure is another potent agent in inducing the Mott transition. An increase in pressure augments the orbital overlap, leading to an expansion of the bandwidth W and a consequent reduction in the correlation strength U/W [12]. The electronic structure, and by extension the phase of the material, is sensitive to changes in pressure, offering a pathway to modulate the electronic and structural properties of Mott insulators.

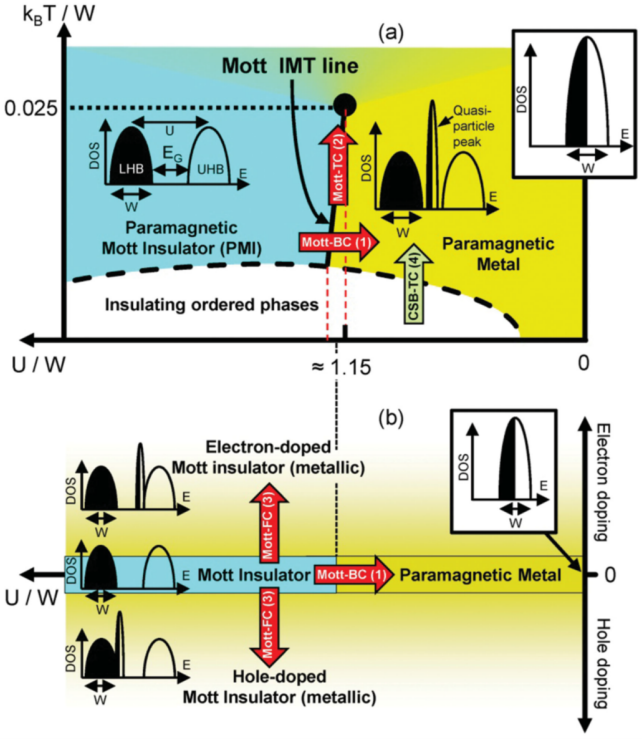

Figure 1.2: (a) Phase diagram showing the Mott insulator-to-metal transition for half-filled compounds in two and three dimensions, plotted with temperature (T) normalized by bandwidth (W) against the Hubbard repulsion (U) normalized by W. The diagram includes typical electronic Density of States (DOS) for three regions: no electron correlation (U/W = 0), the correlated metal state just below U/W = 1.15, and the Mott insulating state for ($U/W > 1.15$). (b) The behavior of doped Mott insulators, mapping electron and hole doping levels relative to half-filling against U/W, for a temperature range between the ordered phase and the endpoint from part (a). Red arrows highlight the universal transitions from the Paramagnetic Mott Insulator: "type 1" Mott-bandwidth controlled (Mott-BC), "type 2" Mott-temperature controlled (Mott-TC), and "type 3" filling-controlled (Mott-FC) insulator-to-metal transitions. The green arrow indicates a "type 4" non-universal, temperature-controlled transition leading to a state with long-range order and associated Crystallographic Symmetry Breaking (CSB-TC). [9].

1.2.3 Doping

Doping introduces additional carriers into the system, offering another avenue to induce the Mott transition [9]. The transition occurs when the number of electrons per site changes, moving away from having a whole or half-filled band. The intricate balance of electronic correlations is thus disturbed, facilitating a transition from the insulating to the metallic state. This manipulation not only provides insights into the complex electron interactions within Mott insulators but also presents a methodology for tuning their electronic properties. Figure 1.2 illustrates the effect of electron and hole doping away from half-filling on the Mott transition, highlighting the pathways through which the electronic structure evolves as a result of doping.

1.3 Electric field-driven transition in AM_4X_8

The exploration of Mott insulator-to-metal transitions has traditionally been dominated by pressure and doping mechanisms. However, their applicability in the realm of modern microelectronics is constrained. A rich area of research is the induction of insulator-to-metal transitions (IMT) through electric fields, a phenomenon characterized by nonlinear electrical behaviors and both volatile and resistive switching in Mott insulators. Various mechanisms, contingent on the material type, underpin these out-of-equilibrium behaviors. This section is devoted to a meticulous examination of electric field-driven transitions in AM_4X_8 compounds, unearthing the underlying mechanisms and their implications for both theoretical comprehension and technological applications.

1.3.1 Properties of AM_4X_8 compounds

Having explored the intricate dynamics induced by temperature, pressure, and doping in Mott insulators, we now narrow our focus to the unique behavior exhibited by the AM_4X_8 compounds under the influence of electric fields. These compounds, a distinctive subset of Mott insulators, present an opportunity to unravel the complex interplay between structural and electronic properties under external stimuli.

The AM_4X_8 compounds consist of a series of chalcogenides, denoted by the general formula AM_4X_8, where A is Ga or Ge, M represents transition metals like V, Nb, Ta, or Mo, and X includes chalcogen elements S, Se, or Te [13]. They are characterized as deficient spinels with tetrahedral transition metal clusters and are represented by the cubic lacunar spinel structural archetype, as seen in Figure 1.3. This structural uniqueness underscores their distinct molecular orbital arrangements and electronic configurations.

The electronic structure of the AM_4X_8 clusters, particularly for combinations $A = Ga/Ge$, $M = Nb/V$, and $X = S$, has been a subject of extensive study across various temperature regimes [14–16]. The findings from these studies offer insights into the complex interplay of electronic states, influenced by the compounds unique structural configurations and intrinsic electronic properties.

In addition to their complex electronic structure, the AM_4X_8 compounds exhibit a series of distinct characteristics that are emblematic of Mott insulators. These properties are outlined as follows:

- **Temperature stability:** The compounds are *paramagnetic insulators* above 55K and do not exhibit any temperature-controlled transition up to 800 K at ambient pressure [5, 16].
- **Pressure transition:** $GaTa_4Se_8$ and $GaNb_4X_8$ (for $Q = S, Se$) undergo a bandwidth-controlled insulator to metal transition under pressure, initiating superconductivity at $T_C \approx 2 - 7$ K above 11 GPa [5, 18].

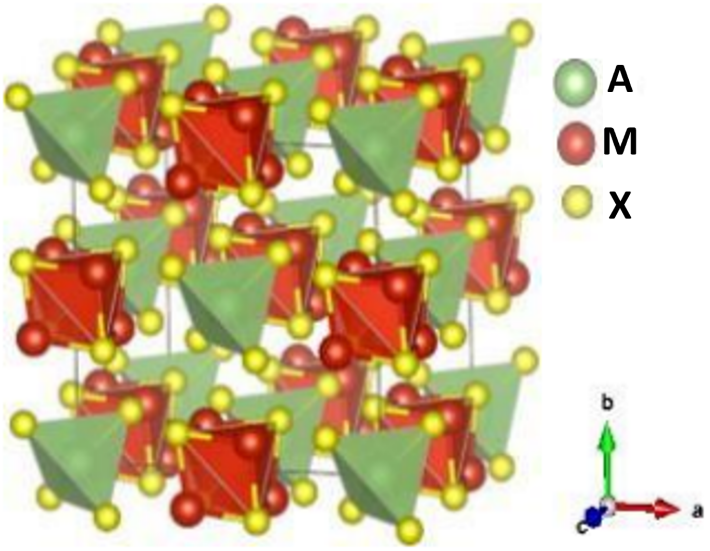

Figure 1.3: The cubic lattice structure of the lacunar spinel AM_4X_8. [17].

- **First-order transition:** A first-order pressure-induced bandwidth-controlled IMT is confirmed by a hysteresis in $GaTa_4Se_8$ transport property measurements [6].
- **Correlated metal:** Optical conductivity measurements under pressure reveal the formation of a quasi-particle peak, indicating a transition to a correlated metal state [19].
- **Doping-induced transition:** The AM_4X_8 compounds experience a filling-controlled IMT when doped on the A or M site, a characteristic behavior of Mott insulators [20].

In addition to these transition behaviors, the AM_4X_8 compounds are known to exhibit a variety of exotic electronic phenomena. These are attributed to the intricate interplay of electronic, magnetic, and structural elements within these materials. Notable phenomena include negative colossal magnetoresistance, ferromagnetic half metallicity, multiferroicity, and Néel type skyrmion lattice [20–22].

1.3.2 The electric Mott transition

A hallmark of Electric Mott Transition in Mott insulators, including $GaTa_4Se_8$, $(V_{2-x}Cr_x)_2O_3$ and $NiSe_{2-x}S_x$, is the occurrence of a volatile resistance drop or resistive switching when exposed to an electric field [23]. This phenomenon is typically initiated by voltage pulses that exceed a certain threshold value, approximately a few kV/cm. The switching is characterized by a delay time that diminishes as the applied voltage increases. Remarkably, post-switching, the electric field within the sample consistently aligns with the threshold electric field, a pattern also observable in DC measurements. Figure 1.4 illustrates the experimental signature of the electric field induced transition, consistently seen in three families of Mott insulators.

As shown Figure 1.4, Mott insulator compounds are known for their distinct I(V) characteristics, which are divided into two specific branches. The first branch is associated with the non-transited state and exhibits behavior closely aligning with Ohm's law. The second branch, almost vertical, emerges at the threshold field and is indicative of the transited state, marking the onset of resistive switching.

Furthermore, all Mott insulators, including AM_4X_8 compounds, exhibit a consistent I(V) characteristic with a threshold electric field ranging between 1-10 kV/cm. The carrier-driven collapse of the Mott gap has been also observed in non canonical narrow gap Mott insulators such as 1T-TaS_2 thin films, where the Mott phase coexist with a charge density wave [25].

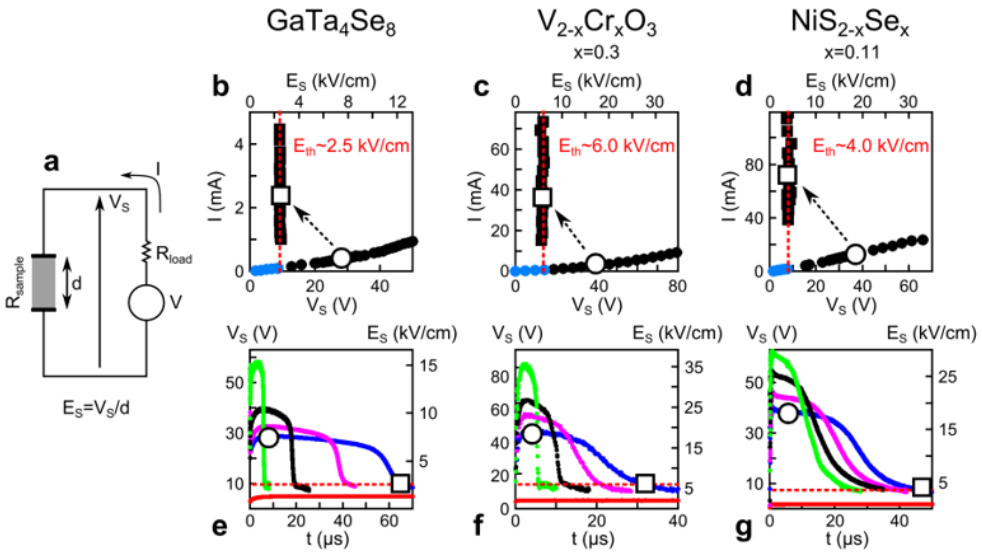

Figure 1.4: a) Diagram illustrating the experimental arrangement. b-g) Standardized I-V curves (depicted in panels b, c, d) and the temporal evolution of the sample voltage $V_S(t)$ (shown in panels e, f, g) for three distinct categories of narrow-gap Mott insulators. Data points in blue represent the phase below E_{th}, where no breakdown is evidenced. Black markers delineate the I-V curve in the resistive switching region, beyond E_{th}. Initial I-V characteristics before the breakdown are denoted by black dots, while the black squares represent the post-breakdown state. Open markers emphasize a specific breakdown transition for enhanced clarity. Tests on GaT_4Se_8 were conducted at 77 K, on $(V_2 - xCr_x)O_3$ (x=0.3) at 164 K, and on $(NiSe_2 - xS_x)$ (x=0.11) at 4 K. Detailed experimental procedures are elaborated in. [24]

1.3.3 Mechanism of the electric Mott transition

The consistency in the electrical response of narrow gap Mott insulators has been observed in the context of avalanche breakdowns in narrow-gap semiconductors, leading to the proposition that resistive switching in AM_4X_8 Mott insulators is akin to an avalanche breakdown. In the realm of semiconductors, the avalanche threshold field and the bandgap are related by a power-law [26,27], a relationship echoed in the threshold field's dependence on the Mott-Hubbard gap in AM_4X_8 compounds, providing supporting evidence for the avalanche breakdown hypothesis [28].

Insights from a resistance network modelisation have provided comprehensive scenarios for the transition onset [24].

Empirical studies have unveiled electric pulse-driven insulator-to-metal transitions and suggested potential electric field induced superconductivity within Mott insulators [29], while observations of resistive switching at the nanoscale have added complexity to our understanding of these transitions [30].

In another hand, Joule heating has been ruled out to explain the electric field-induced Mott transition in AM_4X_8. Stoliar et al. study on the family of narrow gap Mott insulators AM_4X_8 provides strong evidence against the Joule heating effect in such transitions. By comparing experimental observations with simulations of both thermal and electronic models, it was concluded that the resistive switching observed is driven primarily by electronic mechanisms. Their findings, which show experimental results aligning with the purely electronic model and not with the thermal model, strongly suggest that the resistive switching in these systems, including compounds like $GaMo_4S_8$, is primarily electronic rather than thermal [31].

Kalcheim and al., and Okazaki et al. added depth to this narrative, emphasizing that the

resistive transitions observed in other narrow-gap Mott insulators and the current-induced gap suppression in Ca_2RuO_4 cannot be exclusively attributed to Joule heating [32, 33].

1.3.4 Fröhlich's model for electric field-driven transition

Fröhlich and Seitz's seminal contributions to the theory of dielectric breakdown in semiconductors offer a comprehensive framework for understanding the electric field-driven transitions in Mott insulators [34, 35]. They elucidated two distinct regimes of dielectric breakdown, offering invaluable insights into the mechanisms underlying these phenomena.

The first regime, associated with the "clean" limit, is predominantly observed at low temperatures in ultrapure semiconductors characterized by extensive mean free paths. This process unfolds as the sparse electron population independently accumulates energy, initiating an avalanche process. In conventional semiconductors like Silicon (Si), Germanium (Ge), or Gallium Arsenide (GaAs), the breakdown arises from impact ionization. Electrons, once accelerated by the electric field, are excited to energy levels sufficient to instigate impact ionization, thus proliferating electron-hole pairs and elevating additional electrons to the conduction band. This cascade continues if the ionization rate surpasses the recombination rate of electron-hole pairs. In this context, the threshold electric field (E_{th}) escalates with temperature due to intensified electron-phonon scattering.

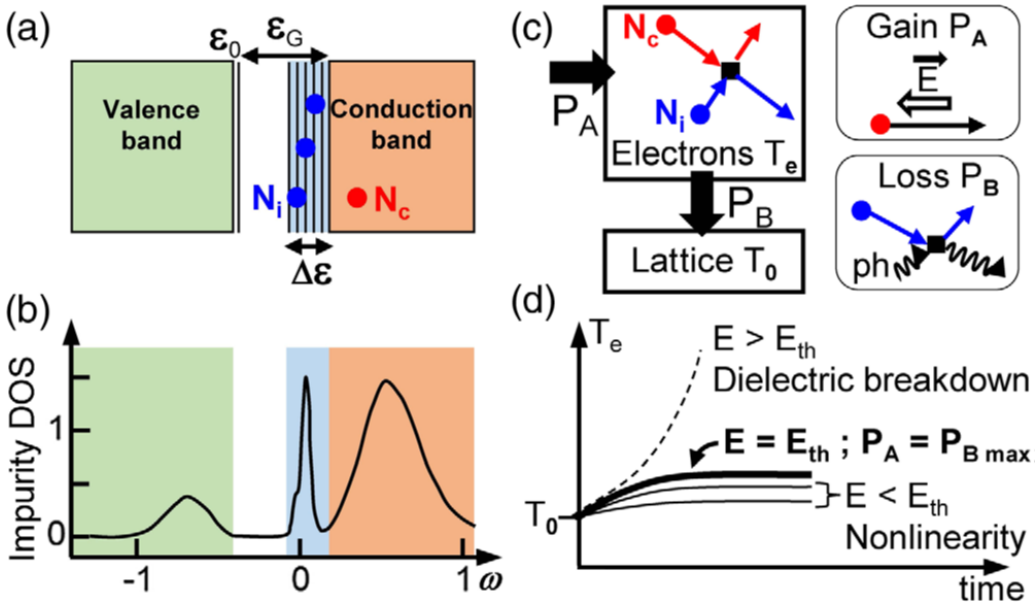

Figure 1.5: Illustration of the breakdown mechanism in the presence of impurities. (a) The energy state density reveals a gap ϵ_G separating the primary impurity level ϵ_0 and the conduction band (highlighted in red), accompanied by distinct impurity levels dispersed across an energy width $\Delta\epsilon$ (depicted in blue). Electrons situated in the impurity levels (Ni) and the conduction band (Nc) are marked by blue and red dots, respectively. (b) A simulated energy state density of the Mott insulator $GaTa_4Se_8$ at a specific temperature, T = 116 K, exhibits an in-gap peak (blue area) at the brink of the upper Hubbard band (red area), an outcome of slight electronic doping (n = 1.045). (c) The electronic system's thermal equilibrium is portrayed, where electrons sustain a temperature T_e, divergent from the lattice temperature T_0. P_A and P_B represent the respective electron heating and cooling powers. (d) The progression of the electronic temperature under various electric field intensities is depicted over time. [35]

Conversely, the second regime emerges when electron-electron scattering becomes significant. This scenario is expected in materials where defects introduce discrete energy levels

within the gap (Figure 1.5a), leading to a characteristic energy width ($\Delta\varepsilon$). In this scenario, trapped electrons, unable to be accelerated by the electric field, significantly influence the dynamics by scattering with conduction electrons and phonons. Such model has been proposed by Fröhlich in the early time of the semiconductor theory, and was eventually abandoned for the modern model, where the localized in-gap states due to impurities or doping are zero-temperature filled states. However, the Fröhlich description hopefully provides an efficient model for the description of Mott semiconductors under electric field. Indeed the in-gap empty states of the Fröhlich model coincide with the localized empty states found systematically by DMFT in Mott insulators close to a Mott transition (See figure 1.5b).

Figure 1.5c shows the equilibrium of the electronic system is maintained by the balance between the energy influx from the electric field to the conduction electrons and the energy outflow from the electrons localized in shallow levels to the lattice. Under an electric field, the electronic temperature escalates until an equilibrium between energy gain and loss is reached, as seen in Figure 1.5d. However, beyond a certain threshold field, this equilibrium is disrupted, precipitating a surge in electronic temperature and culminating in electrical breakdown.

Empirical evidence from studies on AM_4X_8 compounds corroborates the theoretical propositions of Fröhlich and Seitz. Notably, the observed nonlinear electrical behavior at low fields and the temperature-dependent nature of the threshold electric field align remarkably with the model's predictions [35]. The bifurcation into two temperature regimes and the activated dependence of E_{th} at elevated temperatures affirm the applicability of Fröhlich's model in elucidating the electric field-induced transitions in canonical Mott insulators.

1.3.5 Formation and characteristics of the conductive filament

The Electric Mott Transition is characterized by the generation of hot carriers, leading to a specially localized transition from a Mott insulating state to a correlated metal phase under the influence of an electric field. A model that encapsulates this complex behavior envisages a two-minima energy landscape, with the Mott insulator (MI) state occupying the lower energy minimum and the correlated metal (CM) state residing at a higher energy level (Figure 1.6i and j).

This landscape is manifested in a resistor network [24], where the transition probability from the MI to the CM state is voltage-dependent, while the reverse transition is thermally activated over a fixed energy barrier. A volatile resistance drop is associated with the emergence of a metallic filamentary path between the electrodes. This filament forms when the production rate of metallic sites, triggered by the electric field, surpasses their relaxation rate, leading to a critical threshold where a runaway process initiates the filament's formation.

Integrating this energy landscape model with a thermal model supports the notion that the resistive transition's onset is instigated by a purely electronic transition, with Joule heating commencing upon the metallic filament's formation and the subsequent rise in circuit current.

The dynamics of the Electric Mott Transition and associated resistive switching during an electric pulse can be summarized as follows (refer to Figure 1.6): When subjected to an electric field above the threshold electric field, light carriers within the Mott insulators are accelerated. This escalation in electronic temperature fosters a surge in metallic site generation, culminating in an electronic avalanche breakdown. The ensuing formation of a metallic filamentary path within the material occurs after a time delay (t_{delay}), that decreases with the increase of the applied voltage. The resistive switching is realized once this filament bridges the electrodes.

Post pulse, one possible outcome is that the filamentary path fully dissolves, as shown in Figure 1.6h, resulting in a return to the initial resistance value. This characterizes a volatile resistive switching, typically observed for voltages slightly exceeding the threshold field. Such transitions, where the filamentary path is not stable beyond the pulse, represent a transient

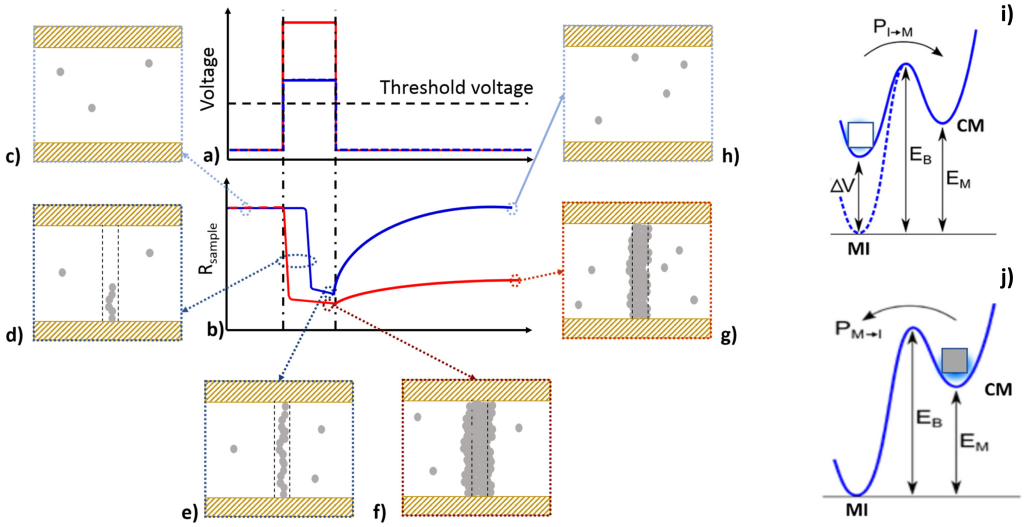

Figure 1.6: Illustration of the electrical transition in a Mott insulator. (a) A depiction of the voltage pulse applied to the Mott insulator, with blue and red representing distinct voltages exceeding the threshold level. (b) The resistance behavior of the sample is tracked before, during, and after the application of voltage pulses. Frames (c) to (h) capture the progressive development of a conductive filamentary pathway within the sample, which correlates with the act of resistive switching. The electrodes are denoted by the brown crosshatched rectangles. Energy diagram of Mott insulator and correlated metal states showing the probability (i) to induce the Mott insulator-metal transition is driven by an external electric field and (j) to relax is thermally activated. [36]

change in the material's resistive state. Conversely, the filament may remain post-pulse, in scenarios commonly occurring at applied voltages significantly surpassing the threshold, marking the non-volatile transition where the reduced resistance state is maintained.

1.3.6 Non-volatile transition

As shown in Figure 1.6g, applying an electric field that exceeds the threshold in narrow gap Mott insulators can result in a persistent metallic filament even after the pulse has ceased. This behavior signals a non-volatile Mott transition, a phenomenon that is consistently observed in such materials [37]. The stability of these filaments is believed to be governed by the elastic properties of the system [38]. Filaments smaller than a critical size tend to dissolve, while larger, metastable filaments can remain stable post-pulse. Importantly, these larger filaments exemplify a reversible aspect of the non-volatile state: they can be reset through a thermally activated process [39]. This reset transition, driven by Joule heating, is typically triggered by applying a prolonged low-voltage pulse, which heats the material to a degree that it switches back to its high-resistance state [38, 40].

Continuing with insights from a detailed study on $GaTa_4Se_8$, the nature of the electric field-induced phase transition in this Mott insulator becomes clearer. The research highlights a nanoscale electronic phase separation, prompted by an electric field [41], that leads to the formation of metallic and super-insulating regions within an insulating matrix. Remarkably, these regions not only follow the filamentary patterns aligned with the electric field but also share a reduced lattice parameter, akin to that observed when the material is under pressure [42]. This congruence suggests that the phase separation and the subsequent filament formation are indeed indicative of a genuine Mott transition, further affirmed by the significant interplay

between electronic behavior and topographic features. This understanding is crucial for the development of memory devices that use these non-volatile transitions to store information reliably.

1.3.7 Neuromorphic applications of AM_4X_8 compounds

The resistive switching attributes of AM_4X_8 compounds are not only a scientific curiosity but also hold promising practical applications, particularly in the burgeoning field of neuromorphic engineering.

The compounds unique ability to undergo electric field-induced transitions is especially relevant for the development of artificial neurons. In the realm of neuromorphic computing, where the objective is to mimic the brain's neural architecture and functionality, AM_4X_8 compounds play a pivotal role. The materials' switching characteristics, induced by an electric field, are akin to the action potentials in biological neurons, facilitating signal transmission and processing within artificial neural networks.

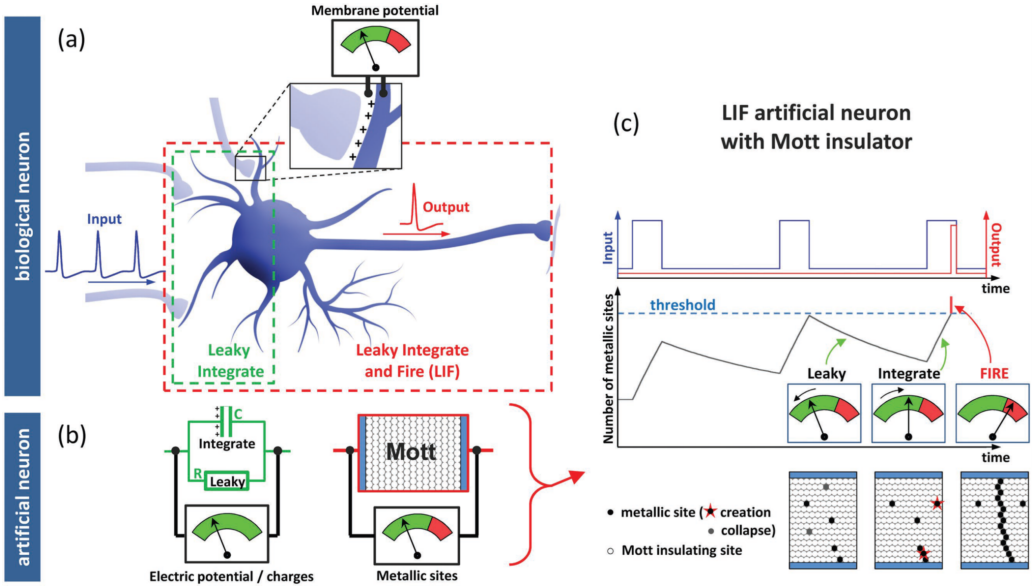

Figure 1.7: a) An illustration of a biological neuron that receives input spikes from neighboring neurons, initiating an output action potential once the membrane potential surpasses a specific threshold. b) LIF artificial neurons, inspired by Lapicque's model, mimic the dynamics of the membrane potential using a Resistance Capacitance (RC) circuit to accumulate electrical charges. c) The Mott artificial neuron, shown in this panel, emulates the LIF functionality by accumulating correlated metallic sites. [43]

As illustrated in Figure 1.7, there exists a striking analogy between biological neurons, Leaky Integrate-and-Fire (LIF) artificial neurons, and Mott artificial neurons. Figure 1.7a provides a schematic representation of a biological neuron that accumulates input spikes and triggers an output action potential upon reaching the threshold membrane potential. Similarly, the LIF model (Figure 1.7b), based on Lapicque's pioneering work, employs a Resistance Capacitance (RC) circuit to emulate the charge accumulation and release dynamics intrinsic to biological neurons.

In a parallel development, the Mott artificial neuron, depicted in Figure 1.7c, mirrors the LIF behavior, thanks to the accumulation of correlated metallic sites. This innovative approach leverages the unique properties of AM_4X_8 compounds, underscoring their potential as building blocks for advanced neuromorphic systems. The figure eloquently captures the equivalence in variable and equation dynamics between the LIF and Mott neuron models, reinforcing the

potential of Mott systems to implement LIF functionalities using a simple two-terminal device rooted in Mott insulator compounds.

The threshold and switching behaviors of AM_4X_8 compounds emulate the excitatory and inhibitory responses of biological neurons. This emulation enables the execution of complex computations, akin to pattern recognition and adaptive learning, central to brain-like processing. The integration of AM_4X_8 compounds into artificial neurons underscores a convergence of computational efficiency and energy conservation, opening avenues for advanced real-time processing and analytics in various applications, including machine learning and artificial intelligence.

The LIF function has been observed in several narrow gap Mott insulators, AM_4X_8, organic materials, and V_2O_3:Cr in crystalline samples and thin films [36, 44]. Figure 1.8 shows the experimental signature of the LIF function in $GaMo_4S_8$ single crystals at 74 K.

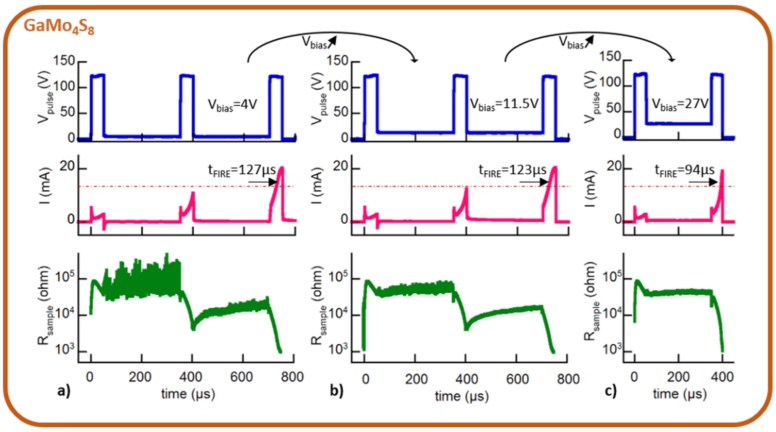

Figure 1.8: The response of $GaMo_4S_8$ to a train of pulses with $t_{ON} = 50\mu s$ and $t_{OFF} = 300\mu s$, subjected to different bias voltages at 74 K. The distinct panels illustrate the nuanced variations in resistive switching characteristics, contingent on the applied bias voltage [36].

In these experiments, a train of pulses, each with a duration of $t_{ON} = 50\mu s$ and separated by an interval of $t_{OFF} = 300\mu s$, was applied, with the bias voltage V_{bias} varying from 4 V to 27 V. A key observation is that the number of pulses needed to trigger a resistive switching event, denoted as N_{FIRE}, is dependent on the bias voltage. An increase in bias voltage correlates with a reduction in N_{FIRE}, indicating a shortened time delay before the switching event.

Additionally, the extent of resistance relaxation between pulses is modulated by the bias voltage. Elevated bias voltages result in reduced resistance relaxation, indicating that a larger proportion of metallic sites is retained during the t_{OFF} periods. These observations underscore the complex dynamics that characterize the resistive responses of Mott insulators, further highlighting their potential in neuromorphic applications.

1.4 A room temperature 2D Mott insulator: $TaSe_2$

While the electrically induced Mott transition in AM_4X_8 compounds reveals a fascinating interplay of electronic correlations, the practical application of this phenomenon necessitates a journey beyond bulk crystals. The quest for materials that are not only governed by intricate electronic interactions but are also amenable to integration into functional devices directs our attention to two-dimensional Mott insulators.

In the world of 2D materials, Mott insulators are rare. One well known example is the bilayer of graphene sheets, rotated by an angle of 1.1° [45]. However, the difficulty of the process used to obtain the precise rotation angle between the exfoliated graphene sheets hinder the potential of such system for applications.

Recent studies on Pb/Si(111) have further elucidated the role of electron correlations and spin-orbit interactions in 2D materials. Investigations by Tresca et al. have shown that even within a monolayer, complex electronic behaviors such as charge density waves and correlated metallic states emerge, driven by intricate interactions between lattice structures and electron dynamics [46, 47]. Moreover, studies on Sn/Si(111) reveal that this system undergoes a Mott insulating phase, in stark contrast to the correlated metallic state observed in Pb/Si(111), thereby showcasing the diversity of electronic behaviors in two-dimensional materials [48]

In this quest for alternative 2D Mott insulators that shows intricate electronic behaviors with application potentials, the transition metal dichalcogenide 1T-$TaSe_2$ emerges as a compelling candidate. Distinct from other known 2D materials, 1T-$TaSe_2$ boasts a rich phase diagram that offers a playground for exploring complex electronic interactions and responses to external stimuli.

As we pivot our focus to 1T-$TaSe_2$, the ensuing sections will delve into its electronic, structural, and dynamical properties. We aim to unravel how 1T-$TaSe_2$ embodies the exemplar of 2D Mott insulators.

1.4.1 General properties on transition metal dichalcogenides (TMDs)

Transition Metal Dichalcogenides (TMDs) form a broad category of layered materials, typically denoted by the chemical formula MX_2, where M stands for a transition metal, and X represents a chalcogen element such as sulfur, selenium, or tellurium, as shown in Figure 1.9a. These compounds are characterized by their distinctive layered structure, consisting of strong in-plane bonds and weaker van der Waals forces between the layers (Figure 1.9b). This unique bonding arrangement makes it possible to exfoliate TMDs into thin two-dimensional layers.

The electronic properties of TMDs are remarkably diverse, influenced not only by the choice of transition metal and chalcogen elements but also by their structural polytypes. For instance, MoS_2 exhibits semiconductor behavior in its 2H form, where atoms are stacked in a trigonal prismatic arrangement, leading to an indirect band gap. In contrast, the 1T form of MoS_2, with a metallic octahedral arrangement of atoms, results in a direct overlap of electron orbitals that contribute to metallic properties [51]. This family of materials includes not only semiconductors like WS_2, semimetals such as WTe_2 and $TiSe_2$, but also metals exemplified by NbS_2 and VSe_2, and even superconductors like $NbSe_2$ and TaS_2 [50]. Within these structural variations, phenomena such as charge density waves (CDWs) can emerge, particularly in systems like 1T-$TaSe_2$, where the unique stacking and electronic interactions foster complex physical behaviors.

1.4.2 Charge Density Waves in transition metal dichalcogenides

Charge Density Waves (CDWs) in Transition Metal Dichalcogenides (TMDs) represent a collective electronic phenomenon arising from strong electron-phonon interactions. Manifested as

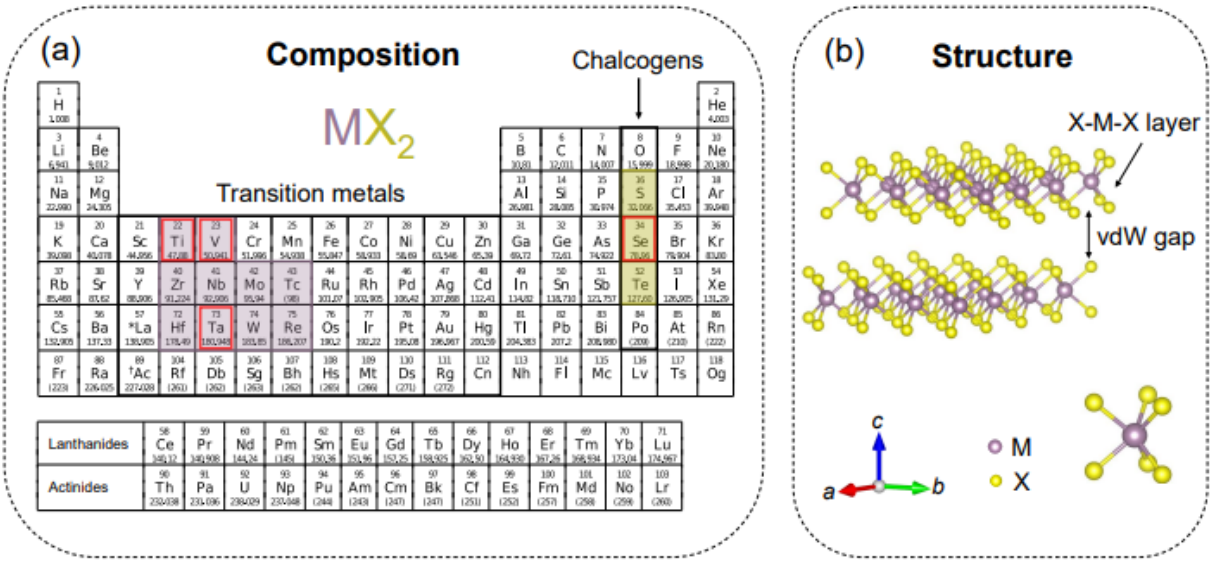

Figure 1.9: (a) A periodic table showing transition metals and chalcogens marked by black borders. The shaded regions specify the particular transition metals (M) and chalcogens (X) that constitute TMD compounds with the stoichiometry MX_2. (b) Schematic of the TMD crystal structure, illustrating the layers constructed from triple atomic planes (X-M-X), interspaced by van der Waals gaps. [49]

periodic modulations in electron density, CDWs are accompanied by a small distortion of the crystal lattice. Their presence causes notable anomalies in temperature-dependent transport properties, such as electronic, magnetic, and thermal behaviors, indicative of underlying phase transitions [52–55].

While CDWs are primarily explored within the context of TMDs, similar phenomena are observed in other quasi-one-dimensional and low-dimensional systems, illustrating the universality and diversity of CDW effects. For instance, the blue bronze oxides $Rb_0.3MoO_3$ exhibit a Peierls transition, a common mechanism behind CDW formations, showcasing significant electron-lattice interactions that lead to CDW states [56]. This example underscores the varied structural dependencies and behaviors CDWs can exhibit across different material systems. Further insights into the complex interactions between multiple CDW states can be observed in the study of $NbSe_3$. This quasi-one-dimensional metal reveals detailed interplays between different CDW wave vectors at low temperatures. The interactions are so intricate that they produce new domain superstructures along the chain axis [57], offering insights into potential behaviors in TMDs under similar low-dimensional constraints.

Table 1.1 presents a comparative overview of CDW transitions in various TMDs, highlighting the diversity of observed behaviors. The CDW states range from commensurate (C-CDW), where the electron density modulation aligns with the lattice, to incommensurate (I-CDW) and nearly commensurate (NC-CDW), each associated with unique structural and electronic properties [58].

In a C-CDW, the periodicity of the CDW matches the atomic lattice, forming a stable superlattice. I-CDW states, however, exhibit a CDW period mismatched with the lattice, causing continuous phase shifts within the material. NC-CDWs exist between these extremes, displaying periodic disruptions known as phase slips, which maintain an average periodicity close to the lattice constant. These varied CDW states influence the electronic properties of TMDs and their responses to external stimuli such as temperature and pressure.

Among the TMDs, 1T-$TaSe_2$ stands out due to its high CDW transition temperature of

Bulk Materials	**Phase**	**CDW Transition Temperature (T_{CDW}) and Structure**
VS_2	1T	∼305 K [59]
VSe_2	1T	∼107 K [60]
NbS_2	2H	No CDW phase transition [[61], [62]]
$NbSe_2$	2H	35 K (3×3 structure) [63]
TaS_2	1T	C-CDW at 180 K NC-CDW at 350 K I-CDW at 550 K [64, 65]
$TaSe_2$	1T	C-CDW at 473 K ($\sqrt{13} \times \sqrt{13}$ structure) I-CDW at 600 K [66]
$TaSe_2$	2H	C-CDW at 122 K [67] I-CDW at 90 K [67]
$TiSe_2$	1T	C-CDW at 90 K (3×3 structure) I-CDW at 123 K [68, 69]

Table 1.1: Phase transition of bulk CDW materials. C-CDW, commensurate CDW; NC-CDW, nearly-commensurate CDW; IC-CDW, incommensurate CDW.

473 K, well above standard room temperature (298 K). This characteristic ensures the stability of the CDW state at temperatures useful to many practical applications. The ability to maintain a CDW state at such temperatures makes 1T-$TaSe_2$ a particularly intriguing material for technological use, as it promises operational consistency in conditions that surpass typical laboratory environments.

The pronounced CDW states in TMDs, such as those observed in 1T-$TaSe_2$, are often associated with the formation of a superlattice structure, a periodic rearrangement of the atoms that extends beyond the basic crystal lattice [70]. In the case of 1T-$TaSe_2$, the superlattice emerges below the CDW transition temperature, manifesting as a "Star of David" pattern as shown in Figure 4.4. This structure consists of thirteen tantalum atoms forming a cluster, with each cluster creating a repeating pattern that resembles the historical symbol. This $\sqrt{13} \times \sqrt{13}$ reconstructed lattice is not just a fascinating structural feature but also has profound implications for the material's electronic properties.

The formation of the SOD superlattice in 1T-$TaSe_2$ induces a profound transformation in the electronic band structure. At lower temperatures, this superlattice pattern emerges, leading to band folding, which narrows the bandwidth. Such a restructuring of the electronic landscape is a precursor to the Mott insulating state observed as the system approaches the monolayer limit. This structural intricacy sets the stage for a dimensionality-induced Mott transition, highlighting the intricate relationship between lattice arrangements and electronic properties in TMDs.

1.4.3 Dimensionality-induced Mott transition in 1T-$TaSe_2$

The transition from bulk to monolayer 1T-$TaSe_2$ epitomizes the significant impact of dimensionality on electronic properties. In its bulk form, 1T-$TaSe_2$ typically exhibits metallic behavior, with electrons free to move and conduct electricity [72, 73]. However, as the dimensionality is reduced to a monolayer, the nature of electron interactions undergoes a dramatic shift. Strong electron correlations, magnified in the two-dimensional limit, dominate, leading to the emergence of a Mott insulating state. This state is characterized by electron localization, which inhibits conductivity despite the presence of free electrons that would ordinarily facilitate a metallic state.

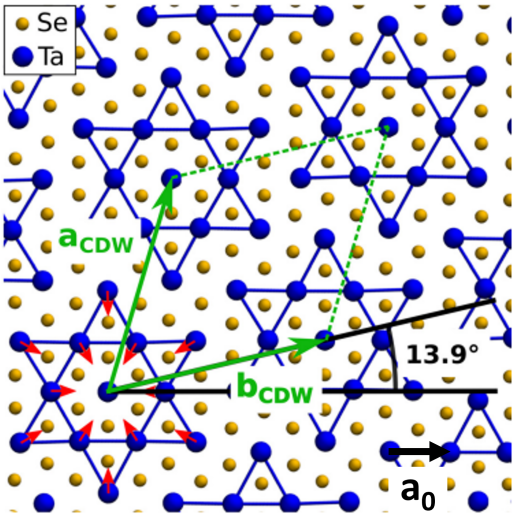

Figure 1.10: Schematic of the C-CDW in a single layer of 1T-$TaSe_2$, with selenium atoms represented in orange and tantalum atoms in blue. The tantalum lattice displays a star-of-David-like configuration composed of a central atom surrounded by 12 outwardly displaced tantalum atoms, as denoted by the red arrows. The lattice vectors a_{CDW} and b_{CDW} delineate the unit cell of the commensurate superstructure, illustrating the transformation from the original lattice (a_0) to the expanded $\sqrt{13} \times \sqrt{13}a_0$ superstructure. This superstructure exhibits a rotation of approximately 13.9° relative to the undistorted lattice. [71]

The dimensionality-induced Mott transition in 1T-$TaSe_2$ is discernible at a critical thickness that has been a subject of active research. Studies indicate that the Mott insulating state manifests at a thickness of merely three layers [74], a phenomenon that is clearly depicted in Figure 1.11a. This figure presents STM dI/dV spectra for single-layer, bilayer, and trilayer 1T-$TaSe_2$, highlighting a diminishing energy gap with increased layer count and interlayer coupling. Conversely, temperature-dependent resistivity measurements further elucidate the changes induced by dimensionality. Figure 1.11b demonstrates a metal-to-insulator transition upon thinning the material, pinpointing a critical thickness at seven layers. This behavior is in stark contrast to the intrinsic metallic nature of bulk 1T-$TaSe_2$, which is also depicted for reference [75]. The data from these figures compellingly illustrate the dependency of 1T-$TaSe_2$ electronic properties on the number of layers, underscoring the profound impact of dimensionality on the material electronic phases.

1.4.4 High-temperature stability of the Mott state in monolayer 1T-$TaSe_2$

The robustness of the Mott insulating state in monolayer 1T-$TaSe_2$ extends surprisingly to high temperatures, a characteristic that distinguishes it from similar bulk materials. Experimental breakthroughs have disclosed that the Mott state not only forms in monolayer 1T-$TaSe_2$ but also endures well beyond standard room temperature conditions [76].

Comprehensive angle-resolved photoemission spectroscopy (ARPES) studies have confirmed the high-temperature stability of the Mott insulating state in monolayer 1T-$TaSe_2$. The spectral features captured by ARPES at various temperatures, as depicted in Figures 1.12a-c, consistently demonstrate the presence of the Mott gap across a broad temperature range. The energy distribution curves (EDCs) at the Γ point, as shown in Figure 1.12d, further corroborate the persistence of the Mott insulating behavior at temperatures as high as 450 K, highlighting the notable difference in the thermal stability of the monolayer compared to its bulk form.

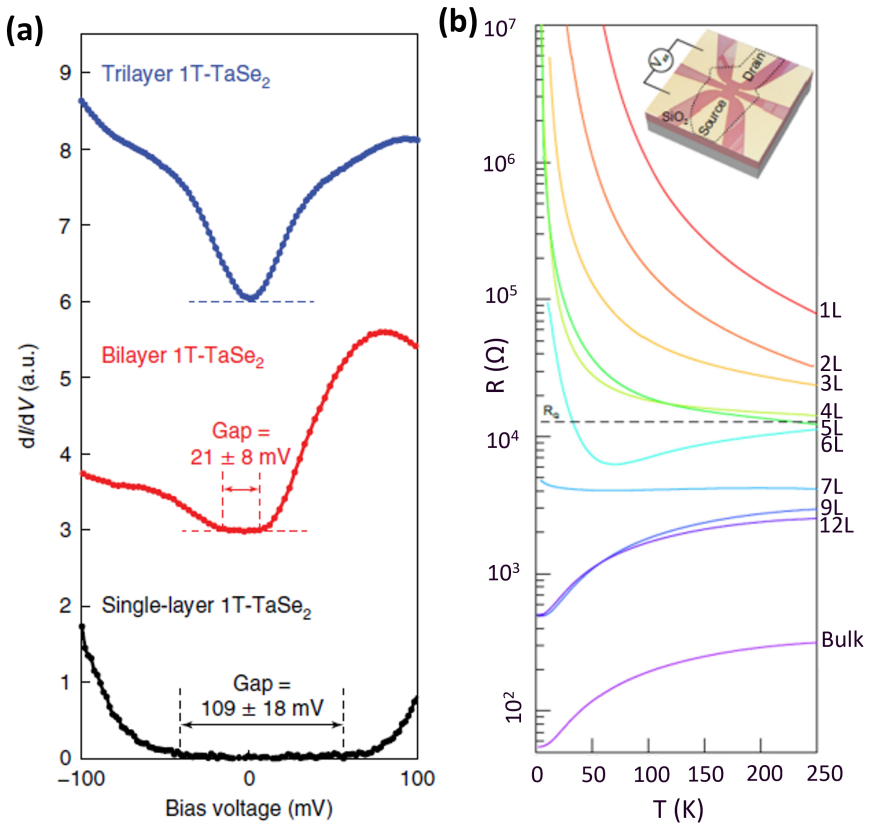

Figure 1.11: (a) STM dI/dV spectra for single-layer, bilayer and trilayer 1T-$TaSe_2$ grown on graphene substrate, show how interlayer coupling reduces the energy gap with an increasing number of layers. The spectra are shifted vertically for viewing (the horizontal dashed lines mark dI/dV = 0, f = 401 Hz, Vr.m.s. = 2 mV) [74]. (b) Temperature-dependent resistivity of 1T-$TaSe_2$ flakes with varying number of layers, the substrate used is Si wafer covered with 285 nm layer of SiO_2. A metal to insulator transition is clearly visible at the critical thickness of seven layers. Data from bulk 1T-TaSe2 is also shown as a reference [75].

Further analysis is presented in Figure 1.12e, where the squared leading-edge midpoint (Δ_{LEM}) at the Γ point is plotted against temperature for monolayer 1T-$TaSe_2$. These findings, along with semiphenomenological fittings should be dfined, suggest a CDW-Mott transition temperature ($T_{CDW-Mott}$) around 530 K for the monolayer, significantly exceeding that of bulk 1T-$TaSe_2$. The error bars account for uncertainties from the energy resolution and standard deviation in the peak positions of EDCs, indicating the precision of these measurements. This body of evidence points to a strongly coupled CDW-Mott phase in monolayer 1T-$TaSe_2$, with the unusual orbital texture observed within this state suggesting a complex interplay between electron and lattice dynamics. The resilience of the Mott state in monolayer 1T-$TaSe_2$ at elevated temperatures not only challenges our fundamental understanding of low-dimensional systems but also indicates the potential for high-temperature electronic applications.

1.4.5 Substrate influence on the properties of 1T-$TaSe_2$ monolayers

The selection of an appropriate substrate is critical in the synthesis of 2D materials, significantly influencing their physical properties. The substrate can impose strain, alter electronic structures, and affect surface interactions, which are all pivotal in determining the behavior of monolayer materials. Notably, lattice mismatches between the monolayer and the substrate can profoundly influence both structural and electronic properties. Such mismatches are known

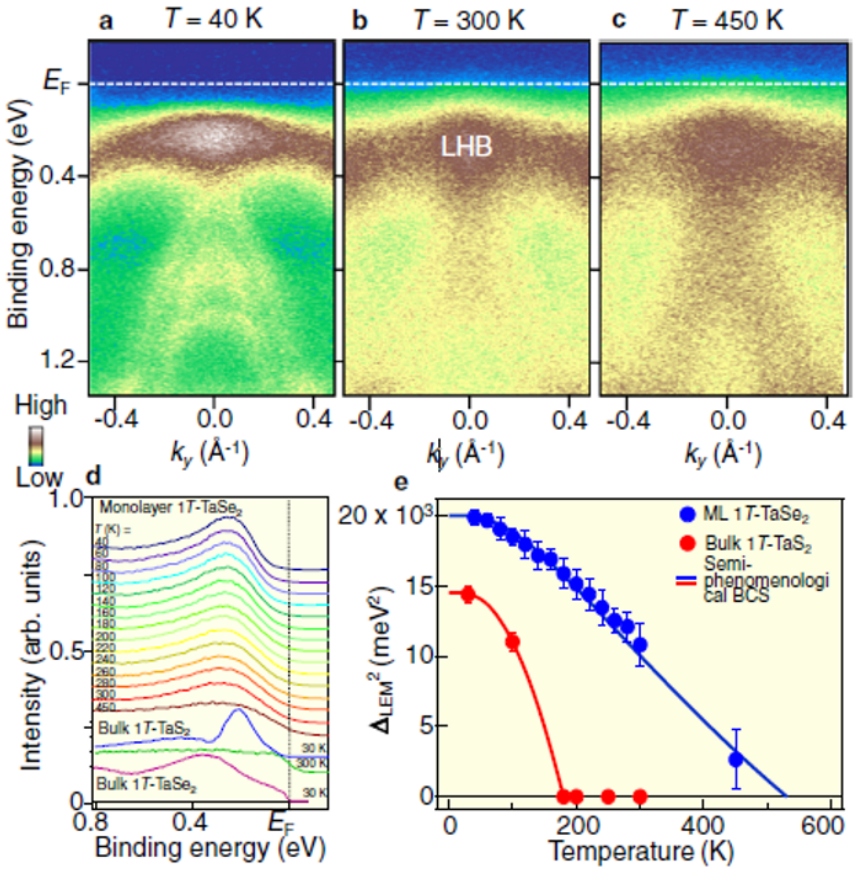

Figure 1.12: (a)-(c) ARPES-measured intensities near the Fermi level along the ΓK direction at temperatures of 40 K, 300 K, and 450 K, respectively. (d) The temperature-dependence of the Energy Distribution Curves (EDCs) at the Γ point, with comparative EDCs for bulk 1T-TaS_2 at 30 K and 300 K, and bulk 1T-$TaSe_2$ at 30 K, provided for reference. (e) The squared leading-edge midpoint (Δ_{LEM}) at the Γ point plotted against temperature for monolayer 1T-$TaSe_2$ (blue circles), alongside numerical fits using BCS (Bardeen–Cooper–Schrieffer) gap function models (blue solid curve). Comparable Δ_{LEM} data and fits for bulk 1T-TaS_2 are shown in red. [76].

to induce strain within the monolayer, potentially altering its intrinsic behavior and the nature of its phase transitions, as evidenced in the study of graphene/VX_2 heterostructures for example [77].

For 1T-$TaSe_2$ monolayers, the choice of substrate has been shown to be particularly influential. While graphene and other metallic substrates have been extensively used [74,78], they can introduce challenges for device integration. Charge transfer and screening effects from these conductive substrates may obscure the intrinsic properties of the monolayer, making it difficult to isolate and study the pure effects of the Mott insulating state.

In this research, we pioneer the use of Gallium Phosphide (GaP) as a novel substrate for the growth of 1T-$TaSe_2$ monolayers. Drawing inspiration from prior studies with GaAs(111) [79–81], GaP(111)B is a semiconductor with a wide bandgap and provides a distinct interaction landscape for the monolayer. Its use could offer a more insulated environment that minimizes substrate-induced perturbations. This approach could potentially allow for a more authentic representation of the monolayer's intrinsic properties, such as preserving the Mott insulating state without the confounding effects of substrate-induced electronic screening.

Preliminary studies suggest that GaP(111)B might improve the integration of 1T-$TaSe_2$ into electronic devices by maintaining the monolayer's essential electronic properties. Although a

detailed exploration of the specific effects of GaP on 1T-$TaSe_2$ monolayers will be presented in subsequent chapters, it is important to recognize that such substrates may prove to be more advantageous for applications that rely on the unique electronic characteristics of 1T-$TaSe_2$.

1.5 Open questions

The study of nanoscale Mott insulators such as $GaMo_4S_8$ and monolayer 1T-$TaSe_2$ has opened up questions that challenge our understanding of their complex behaviors. Despite significant progress, key aspects of their electronic transitions, interactions with varying substrates, and potential technological applications remain elusive. This thesis aims to address these critical questions through an in-depth experimental and theoretical investigation.

The following questions guide our exploration:

- How the resistive switching in $GaMo_4S_8$ is affected by the electrode geometry and a spatially varying electric field?
- How does the temporal evolution of the switching time with respect to the inter-electrode distance correlate with the mechanisms of resistive switching in $GaMo_4S_8$?
- How does a semiconductor substrate affect the formation and stability of the Mott insulating state in 1T-$TaSe_2$ compared to traditional substrates like graphene or HOPG?
- What superstructures are formed within the 1T-$TaSe_2$/GaP system, and how do these influence its electronic properties at the atomic scale, and can we induce a resistive switching in 1T-$TaSe_2$ grown on a GaP substrate?
- Can the insights gained from resistive switching phenomena in monolayer 1T-$TaSe_2$ contribute to the development of advanced neuromorphic devices?

As we progress through the chapters of this thesis, we will methodically unravel the answers to these questions, with each chapter delving deeper into the investigations.

Chapter 2

Experimental techniques

The exploration of the properties of Mott materials necessitates the precise utilization of sophisticated experimental techniques across different scales. This chapter describes the essential role of each method used in this research. Molecular Beam Epitaxy (MBE) is employed for the growth of two-dimensional $TaSe_2$ transition metal dichalcogenides (TMD) Mott materials, which are subsequently studied at the atomic scale using Scanning Tunneling Microscopy/Spectroscopy (STM/STS). For $GaMo_4S_8$ bulk material, four-probe STM is utilized to investigate its electronic properties at the microscale. To complement and provide deeper insights into the experimental results obtained through the four-probe STM, COMSOL Multiphysics simulations are employed. Each of these techniques contributes uniquely to gain a comprehensive understanding of the electronic properties and phase transitions of Mott materials. The ensuing sections detail the methodology and illustrate how each technique is integrated into the larger framework of this study.

2.1 Scanning Tunneling Microscopy

Quantum mechanics, with its revolutionary principles, has profoundly altered our perception of the world at a microscopic scale. Among these principles, the quantum tunneling effect is instrumental in nanoscience, especially in the realm of surface analysis through the STM.

The STM, conceived by Gerd Binnig and Heinrich Rohrer at the IBM Zurich Research Laboratories [82] [83], is offering insights into the surface and electronic structure of electrically conductive materials at the nanometer scale. STM operates based on the tunneling effect, where a metallic probe tip is brought within a few angströms of a (semi)conducting sample. Upon applying a bias voltage between the tip and the sample, electrons have a non-negligible probability of tunneling through the barrier, giving rise to a tunneling current.

This current, which is dependent on the tip position, applied voltage, and the local density of states (LDOS) of the sample, allows STM to map the surface with remarkable precision. STM operates in two primary modes - constant height mode and constant current mode [84]. In the constant current mode, a feedback mechanism adjusts the height of the tip to maintain a constant tunneling current, rendering a detailed representation of the surface structure.

For our study of nanoscale Mott materials, STM plays a role in examining the surface structures and electronic behaviors.

2.1.1 Theoretical background

In quantum mechanics, particles can exhibit counter-intuitive behavior. One such phenomenon is quantum tunneling, where particles have a finite probability of crossing potential energy barriers that would be insurmountable in classical mechanics. This is central to the operation

of STM. A classic analogy, though simplistic, is to imagine a ball spontaneously appearing on the other side of a hill, despite not having sufficient energy to climb over it. Figure 2.1 below provides a schematic representation of the quantum tunneling process in the context of STM.

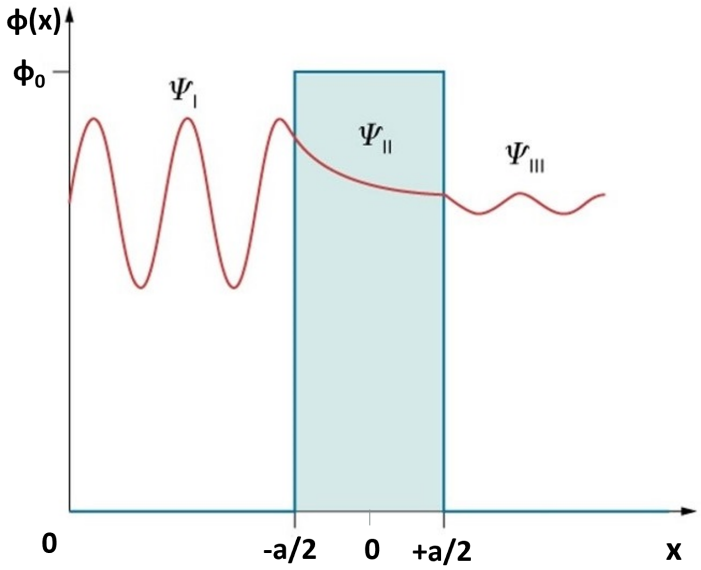

Figure 2.1: Schematic of one-dimensional tunnel barrier.

While the analogy and figure provide a conceptual understanding, a rigorous and precise grasp of quantum tunneling necessitates an exploration into its mathematical foundations. In particular, the Schrödinger equation, a fundamental equation in quantum mechanics [85], offers valuable insights into the behavior of wave functions, which represent the quantum states of particles. By solving the Schrödinger equation for different regions in our tunneling scenario, we can gain a deeper understanding of the tunneling process and the factors that influence it. Let's consider the time-independent Schrödinger equation in one dimension, which can be written as:

$$\frac{-\hbar^2}{2m}\frac{d^2\Psi}{dx^2} + \Phi(x)\Psi = E\Psi \tag{2.1}$$

where $\hbar$ is the reduced Planck constant, m is the mass of an electron, Φ(x) is the potential barrier, and E is the energy of the state. Now, let's consider the potential energy variation in three distinct regions:

Region I (x < -a/2): Before the electron encounters the barrier, it is in a region of potential energy Φ=0. In this region, the Schrödinger equation simplifies to:

$$\frac{d^2\Psi}{dx^2} = -\frac{2mE}{\hbar^2}\Psi \tag{2.2}$$

The general solution of this equation is a superposition of a right-moving wave and a left-moving wave:

$$\Psi_I(x) = Ae^{iKx} + Be^{-iKx} \tag{2.3}$$

Where K=$\sqrt{\frac{2m}{\hbar^2}E}$

Region II (-a/2 < x < a/2): Within the barrier, the potential energy Φ is greater than the energy E of the electron. This leads to an imaginary wave vector, representing the exponential decay of the wave function inside the barrier. The Schrödinger equation in this region becomes:

$$\frac{d^2\Psi}{dx^2} = \frac{2m(\Phi - E)}{\hbar^2}\Psi \tag{2.4}$$

and the solution is:

$$\Psi_{II}(x) = Ce^{K'x} + De^{-K'x} \tag{2.5}$$

where K'=$\sqrt{\frac{2m}{\hbar^2}(\Phi - E)}$

Region III (x > a/2): After the barrier, the potential energy is again Φ=0. The wave function in this region is given by a right-moving wave, representing the electron that has tunneled through the barrier:

$$\Psi_{III}(x) = Fe^{ikx} \tag{2.6}$$

The single term in this solution is a consequence of the electron having tunneled through the barrier. Unlike Region I, where we considered waves moving towards and reflecting off the barrier, in Region III, the electron will not reflect back into the barrier since it encounters no further obstacle.

The coefficients A, B, C, D, and F are linked together by applying the boundary conditions at x=-a/2 and x=a/2, which state that the wave function and its derivative must be continuous across the boundaries. An important quantity in understanding the tunneling phenomenon is the transmission coefficient (T), which represents the probability of an electron tunneling through the barrier. For a barrier of height V and width a, the transmission coefficient is given by:

$$T(E) = \left|\frac{F}{A}\right|^2 = \frac{1}{1 + \frac{\Phi^2}{4E(\Phi - E)}sinh^2(K'a)} \tag{2.7}$$

The transmission coefficient T(E) embodies the probability of an electron successfully tunneling through a potential barrier. As an integral part of quantum mechanics, it represents the likelihood of discovering an electron on the other side of the barrier, even though the energy barrier surpasses that of the electron. Notably, the value of this coefficient ranges between 0 and 1. A value of 0 indicates complete reflection with no tunneling, while a value of 1 signifies unhindered transmission or successful tunneling.

As an illustrative example, consider a case where the STM employs tungsten electrodes, which possess a work function Φ of 4.5 eV. Let's assume that the electron energy E is quite small compared to V, implying that K', which characterizes the decay constant of the tunneling probability, is approximately 1 $Å^{-1}$. This means that for every 1 Å increase in the barrier thickness, the transmission coefficient decays by a factor of e^{-2}, nearly one-tenth of its previous value—an exponential drop indeed.

This rapid decay illustrates the sensitivity of quantum tunneling to the tip-sample separation, which is central to the operation of STM. Given these conditions, we can simplify the expression for the transmission coefficient to:

$$T(E) \simeq \frac{16E(\Phi - E)}{\Phi^2} exp(-2a\sqrt{\frac{2m}{\hbar^2}(\Phi - E)}) \tag{2.8}$$

This equation captures the interplay between the electron energy, barrier thickness, and the material work function in determining the efficiency of quantum tunneling.

Building upon the foundational theory of quantum tunneling and the transmission coefficient, we now turn our attention to an empirical milestone that has significantly advanced our understanding of the tunneling process. In 1982, G. Binnig and H. Rohrer documented the variation of tunneling current with respect to distance [82], a landmark experiment that entailed tunneling through a controlled vacuum gap. Their pivotal work laid the groundwork for the contemporary Scanning Tunneling Microscope, enabling precise quantification of the tunneling current - a vital step in unraveling the intricacies of quantum mechanical processes at the nanoscale.

2.1.2 The tunneling current

Until now, our discussion has centered around the concept of an unpolarized junction, which is primarily useful for the theoretical understanding of the quantum tunneling effect. However, STM involves a polarized junction wherein a voltage bias is applied across the tunneling barrier, leading to the flow of a net current. This current, known as the tunneling current, is a critical measurable quantity in STM and is influenced by various parameters including the applied voltage and the tip-sample separation, as illustrated in Fig 2.2.

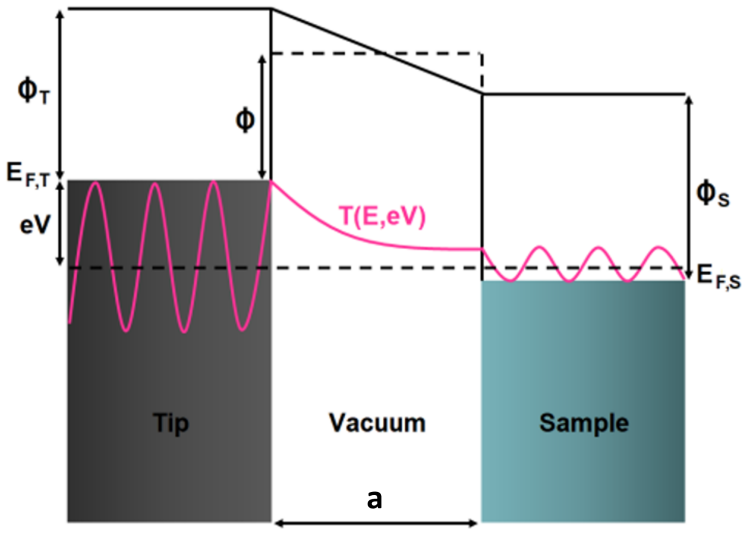

Figure 2.2: Schematic diagram of the tunnel junction in a STM. Φ_T and Φ_S are respectively the tip and the sample work functions, $E_{F,T}$ and $E_{F,S}$ are respectively the tip and the sample Fermi levels, Φ is the average barrier potential, T(E,eV) is the transmission barrier and a is the distance between the tip and the sample. [86]

The tunneling current can be calculated by integrating the transmission coefficient, $T(E,V)$, across all electron energy states in the sample, from the Fermi level of the sample ($E_{f,Sample}$) to that of the tip ($E_{f,Tip} = E_{f,Sample}$ + eV), assuming zero temperature (T=0K).

$$I = \int_0^{eV} T(E,V)\rho_{tip}(E-eV)\rho_{sample}(E)dE \tag{2.9}$$

Here, ρ_{tip} and ρ_{sample} represent the local densities of states for the tip and the sample, respectively. This equation underscores that tunneling current is influenced not only by the transmission coefficient but also by the electron distribution within the sample and the tip.

There are two key approximations which simplify the calculation of the tunneling current in STM:

- The polarization of the electrodes is typically small compared to the tunneling barrier height. This allows us to approximate the trapezoidal barrier as a square barrier with a height of Φ:

$$\Phi = \frac{\phi_{tip} + \phi_{sample}}{2} - \frac{eV}{2} \tag{2.10}$$

- Considering that the distance between the electrodes is about of a few angströms, the transmission coefficient equation can be further simplified:

$$T(E) \approx \frac{16E(\Phi - E + eV)}{\Phi^2} exp\left(-2a\sqrt{\frac{2m}{\hbar^2}(\Phi - E + eV)}\right) \tag{2.11}$$

Substituting this into equation 2.9, we obtain:

$$I \approx \int_0^{eV} \frac{16E(\Phi - E + eV)}{\Phi^2} \exp\left(-2a\sqrt{\frac{2m}{\hbar^2}(\Phi - E + eV)}\right) \rho_{tip}(E - eV)\rho_{sample}(E)dE \tag{2.12}$$

Assuming much lower biases than the average barrier height, it becomes:

$$I \approx 16 \exp\left(-2a\sqrt{\frac{2m}{\hbar^2}}\Phi\right) \int_0^{eV} \frac{E - eV}{\Phi} \rho_{tip}(E - eV)\rho_{sample}(E)dE \tag{2.13}$$

The exponential dependence of the current on the distance between the tip and the sample is crucial for the high-resolution capabilities of STM. For example, with tungsten electrodes which have a work function of ϕ=4.5 eV, a mere 1 Å increase in the tip-sample separation results in a tenfold decrease in the current. This highlights the tunneling current sensitivity to the tip-sample separation and forms the basis for the remarkable resolution achievable with STM.

2.1.3 STM lateral resolution

Resolution is a critical factor in the operation of STM. As demonstrated in Equation 2.13, the tunneling current exhibits an exponential dependence on the distance between the electrodes. From this dependence, it can be inferred that the tunneling process predominantly involves final atom at the tip.

Let's assume that the tip atom has an s-type wave function. It is characterized by:

$$|\Psi|^2 = \frac{e^{-2K'r}}{r^2} \tag{2.14}$$

where $r = \sqrt{x^2 + z^2}$ as illustrated in Figure 2.3. The STM resolution is intricately linked to both the physical and electronic structure of the tip apex. If $z >> x$, r can be approximated as:

$$r \approx z + \frac{x^2}{2z} \tag{2.15}$$

which leads to:

$$|\Psi|^2 \approx \frac{e^{-2K'z}}{z^2} e^{-K'\frac{x^2}{z}} \tag{2.16}$$

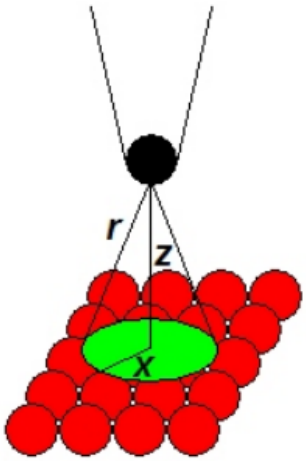

Figure 2.3: Lateral resolution of the STM. [87]

This expression represents a Gaussian function in x, which implies a full width at half maximum (FWHM):

$$\Delta x \approx \frac{2z}{K'} \tag{2.17}$$

The tip height z is defined as the sum of the radius of the tip apex curvature R and the tip-sample distance a. For tungsten tips under low bias, K' is typically close to 1 $Å^{-1}$. As a result, the lateral resolution, Δx, can be approximated as [88]:

$$\Delta x \approx 1.4\sqrt{R} \tag{2.18}$$

For a sharp tip with a radius of $R = 100$ Å, the expected resolution is around Δx=14 Å. However, atomic resolution is often achieved through atomic-sized protrusions at the tip apex, which effectively reduce the radius of curvature, thereby enhancing the resolution. Lateral resolutions on the order of $\Delta x \approx 4.4$ Å are achievable under optimal conditions, with a tip-sample distance $d \approx 5$ Å and a radius of the apex protrusion $R \approx 5$ Å [89–91].

Sacks presented more realistic calculations by considering the tip-sample couplings and including the symmetries of p and d orbitals, in addition to the s orbital. This work contributed to the understanding of the high experimental resolutions achieved by STM [92].

The tunneling current, therefore, serves as an effective feedback mechanism for distance regulation. By mounting both the tip and the sample on a piezoelectric stage capable of precise movements in the X, Y, and Z spatial directions, STM can produce highly detailed topographical images at atomic scales.

2.2 Scanning Tunneling Spectroscopy

Scanning Tunneling Spectroscopy (STS) has emerged as an essential extension of STM, enabling the investigation of local electronic properties of materials with high precision. While STM offers detailed topographical information, STS focuses on examining atomic-level electronic structures by measuring variations in the local density of states (LDOS).

2.2.1 Current vs bias technique: I(V)

One of the fundamental techniques in STS is the current versus bias technique, often abbreviated as I(V). This method was pioneered by researchers such as Feenstra, Thompson, and Fein [93], who made significant contributions to determine the band gap for the 2×1 surface states on the Si (111) 2×1 surface. The I(V) technique requires a constant tip-sample distance by disengaging the feedback loop responsible for automatic control of this distance. The current variations are then measured as the voltage, V, is swept.

In STS measurements, elastic tunneling processes predominantly contribute to the measurements. This suggests that the electrons near the center of the Brillouin zone (with wavevector approximately equal to zero) play a significant role in the tunneling current. Though this may seem restrictive, it is important to recognize that the bandgap for most semiconductors is located at the Γ point of the Brillouin zone.

Extending the tunneling current equation (equation 2.9), and assuming the density of states for the tip to be constant, we can simplify its expression. This assumption allows to factorize the density of states for the tip out of the integral, resulting in a more explicit relationship:

$$I \propto \rho_{tip} \int_0^{eV} T(E, eV)\rho_{sample}(E)dE \tag{2.19}$$

The derivative of the current with respect to voltage can be expressed as:

$$\frac{dI}{dV} \propto e\rho_{tip}\rho_{sample}(eV)T(eV, eV) + e\rho_{tip} \int_0^{eV} \frac{d}{deV}[T(E, eV)]\rho_{sample}(E)dE \tag{2.20}$$

While the above equation may seem comprehensive, it does not simply portray a proportionality with the density of states in the sample. Notably, the transmission coefficient, $T(E, eV)$, increases exponentially with the applied bias. This results in a larger contribution from states at higher energies as compared to states near the Fermi level. Although this effect is negligible for metals, it becomes significant for semiconductors, particularly when higher biases are employed.

This distortion can result in an incorrect representation of the relative amplitudes of states and an inaccurate estimation of the band gap width. To address this issue, Feenstra et al. [94] introduced a normalization procedure where the differential conductance is normalized by the I/V ratio. This normalization effectively cancels out the exponential dependence on $T(E, eV)$, providing a more accurate representation:

$$\frac{\frac{\partial I}{\partial V}}{\frac{I}{V}} \propto \frac{\rho_{sample}(eV) + \frac{1}{eV}\int_0^{eV} \frac{\partial[T(E,eV)]}{\partial eV}\frac{\rho_{sample}(E)}{T(eV,eV)}dE}{\frac{1}{eV}\int_0^{eV} \frac{T(E,eV)}{T(E,eV)}\rho_{sample}(E)dE} \tag{2.21}$$

In this equation, the numerator includes a second term that can be considered as a slowly varying background. Due to its slow variation, it has a minimal impact on the fluctuations of $\frac{dI}{dV}$ as a function of V. Thus, variations in this ratio are primarily governed by the behavior of $\rho_{sample}(eV)$, which leads to a more simplified relationship:

$$\frac{\frac{\partial I}{\partial V}}{\frac{I}{V}} \propto \rho_{sample}(eV) \tag{2.22}$$

This development is instrumental in extracting the LDOS from measured I(V) curves, making the analysis independent of the tip-sample separation. However, there are certain challenges when applying this technique to materials with a wide band gap. Specifically:

- The I/V ratio tends to zero more quickly than the differential conductance as V approaches zero, resulting in a divergence at the edges of the gap. One remedy is to apply an exponential convolution to the I/V ratio, which leads to broadening:

$$\frac{\bar{I}}{V} = \int_{-\infty}^{+\infty} \frac{I(V')}{V'} exp\left(-\frac{|V'-V|}{\Delta V}\right) dE \tag{2.23}$$

  In this equation, ΔV is chosen to be approximately the size of the sample band gap to prevent significant amplification of the noise level within the band gap. This procedure does not shift the peak positions and removes the divergence in the band gap region, enabling a qualitative assessment of the LDOS.

- In the case of I/V normalized differential conductance, when the current decreases in the band-gap region, there may be rapidly oscillating and incoherent results indicative of a low signal-to-noise ratio. To mitigate this, the tip position can be adjusted during the scan to maintain a constant exponential argument:

$$I \propto exp\left(-2a\sqrt{\frac{2m}{\hbar^2}}\sqrt{\phi - \frac{|eV|}{2}}\right) \tag{2.24}$$

To eliminate the distance dependence, it is necessary to find a variation of the tip-sample distance that maintains a constant current throughout the spectrum measurement. This can be achieved by enforcing:

$$a(V)\sqrt{1 - \frac{|eV|}{2\Phi}} = a_0 \tag{2.25}$$

where a_0 is a constant representing the tip-sample distance when V is zero. For small values of V (smaller than ϕ), a Taylor expansion provides:

$$a(V) = a_0\left(1 + \frac{|eV|}{4\Phi}\right) \tag{2.26}$$

As a result, to enhance sensitivity in the band gap region of semiconductors, the tip can be moved closer to the sample following a linear ramp against V. The ramp should be adjusted to have a minimum at V equals zero if the I(V) contains both positive and negative voltages. For example, if a_0 equals 10 Å and ϕ equals 4.5 eV, the slope to counterbalance is 0.56 Å/V. This methodology enables more precise measurements in the band gap region of semiconductors by effectively counterbalancing the varying parameters in the exponential argument during the scan.

In conclusion, STS serves as a powerful tool for investigating the local electronic properties of materials, with techniques such as I(V) spectroscopy providing invaluable insights into the LDOS and band structures. The normalization of the differential conductance, as demonstrated by Feenstra et al., is crucial for extracting the LDOS from measured I(V) curves in a manner that is independent of tip-sample separation. However, when working with wide band gap materials, challenges such as the divergence of the I(V) ratio and the reduction in the signal-to-noise ratio need to be addressed. Employing an exponential convolution to the I(V) ratio and adjusting the tip position during the scan to maintain a constant current are effective strategies for improving the reliability and accuracy of measurements within the band gap region.

2.2.2 Temperature broadening

In the previous section, we discussed the methodologies and challenges of using STS for probing local electronic properties. Another crucial aspect that must be considered for accurate STS measurements is the effect of temperature on the tunneling current. When the system temperature is not at absolute zero, thermal energy can cause electrons to populate states higher than the Fermi level, leading to a broadening of the resonances. This phenomenon is governed by the Fermi-Dirac distribution law.

With this in mind, let's consider the total current flowing through the junction, which is the difference between the current from the tip to the sample and vice versa. Upon summing these, one can derive the following expression:

$$I \propto \int_{-\infty}^{+\infty} [f_{sample}(E) - f_{tip}(E - eV)]T(E, eV)\rho_{tip}(E - eV)\rho_{sample}(E)dE \tag{2.27}$$

The Fermi-Dirac distribution, $f_n(E)$, dictates the electron distribution:

$$f_n(E) = \frac{1}{1 + exp\left(\frac{E - E_{Fn}}{k_B T}\right)} \tag{2.28}$$

The transmission probability T(E, eV) contributes a background to the spectra, but its influence becomes negligible for smaller energies when compared to the barrier height. With the assumption of a constant density of states in the tip (which is consistent with small energies relative to the barrier height), we can write the derivative of the current against the bias voltage as:

$$\frac{\partial I}{\partial V} \propto \rho_{tip} \int_{-\infty}^{+\infty} \frac{\partial f_{tip}}{\partial V}(E - eV)\rho_{sample}(E)dE \tag{2.29}$$

This expression essentially implies that the measured differential conductance spectra correspond to a convolution between the derivative of the Fermi-Dirac function of the tip at this temperature and the LDOS of the sample. The expression of the derivative of the Fermi-Dirac function with respect to voltage is:

$$\frac{\partial f_{tip}}{\partial V}(E - eV) = -\frac{1}{k_B T} \frac{\exp\left(\frac{E - eV - E_F}{k_B T}\right)}{\left[1 + \exp\left(\frac{E - eV - E_F}{k_B T}\right)\right]^{-2}} \tag{2.30}$$

An example of the temperature broadening effect on computed differential conductance spectra is shown in Fig 2.4. The very sharp peaks that would be obtained at absolute zero are gradually smoothened by the expression above, which has a full-width at half-maximum (FWHM) of approximately 3.2 $k_B T$.

2.2.3 Lock-in amplifier

Having discussed the theoretical foundations of STS measurements and the implications of temperature broadening, it is imperative to address the practical aspects of processing and analyzing the signals obtained from these measurements. Signal processing is crucial for reducing the challenges posed by factors such as noise and temperature fluctuations, which can obscure the fine details of electronic properties. The lock-in amplifier serves as an essential tool in this regard, designed to extract a signal with a known carrier wave from an extremely noisy environment, thereby significantly improving the signal-to-noise ratio and enhancing the reliability and precision of the data.

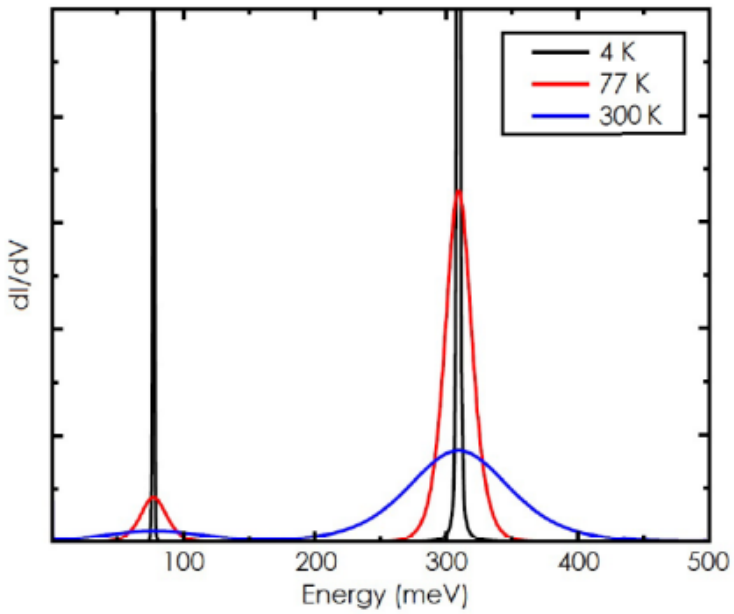

Figure 2.4: Temperature broadening illustrated by the current derivative at 4 K, 77 K and 300 K. [87]

As discussed earlier, obtaining the derivative of the current with respect to voltage is central to probing the LDOS through STS. One might consider numerically differentiating the current, however, this approach, despite its simplicity, is prone to noise amplification. Mechanical instabilities and electronic noise inherently introduce a wide-band noise (up to some kHz) into the measurements, which is exacerbated during numerical differentiation. A major component of this noise originates from low-frequency 1/f noise, which is impervious to removal through numerical methods.

The lock-in amplifier addresses this challenge through phase-sensitive detection, akin to radio broadcasting where a carrier signal of a known frequency is modulated by the signal of interest. This technique measures the amplitude of small AC signals and isolates the noise by shifting the desired signal component to a reference frequency.

When the polarization eV is modulated by a sinusoidal carrier with a small amplitude, expressed as $eV_{mod}\sin(\omega_{mod}t + \phi)$, the tunneling current can be expanded into a Taylor series. With bias modulation, the first and second derivatives of the current manifest in the first and second harmonics of the signal, respectively. It is important to note that the modulation frequency f_{mod} is generally selected to be high relative to the cut-off frequency of the current feedback loop (typically in the range of 500 Hz to 10 kHz), ensuring that the oscillations do not adversely affect the STM image or spectrum.

The different elements of the lock-in amplifier are shown in Figure 2.5 and can be described through the following steps:

- A bias voltage is applied to the sample with the superimposition of a small sinusoidal oscillation at a predetermined frequency. This modulation induces oscillations in the tunneling current, resulting in an input signal comprising both the desired information and background noise.
- The input signal is then fed to the lock-in amplifier, alongside a reference signal derived from the modulation frequency of the bias voltage.
- Employing phase-sensitive detection, the lock-in amplifier multiplies the input signal with

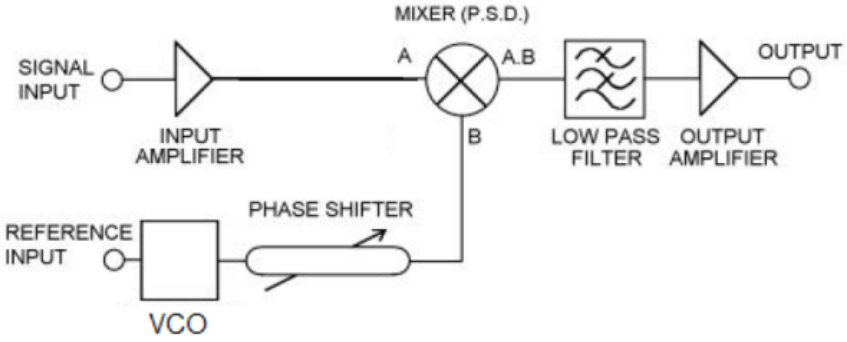

Figure 2.5: A schematic representation of the process of signal processing with a lock-in amplifier in scanning tunneling spectroscopy. [95]

the reference signal. This multiplication generates a composite signal that includes components at both the sum and difference of the frequencies of the two initial signals.

- Subsequently, the lock-in amplifier employs a low-pass filter to eliminate the high-frequency sum component, retaining the desired signal at the difference frequency.
- The amplitude of this isolated signal represents the derivative of the current (dI/dV), which is roughly proportional to the LDOS. The lock-in amplifier measures this amplitude.
- Post demodulation, the lock-in amplifier yields an output signal proportional to dI/dV. With meticulous calibration, this output can serve as an estimator for the LDOS.
- It is imperative to recognize that the lock-in amplifier is not free from intricacies. The tip-sample system, along with the interconnecting wires to the preamplifier, can manifest as a capacitance. This causes a parasitic sinusoidal current akin in frequency to the modulation. However, this parasitic current can be mitigated by superimposing the inverse signal, derived from the reference.
- Additionally, judicious attention must be accorded to the modulation amplitude. The temporal integration of the modulation signal culminates in a half-round curve versus energy, known as the "instrumental resolution function". If eV_{mod} is inferior to the desired energy resolution, the spectrum remains negligibly broadened. Nonetheless, in certain scenarios, an enhancement of the Signal-to-Noise ratio mandates an increment in the modulation amplitude to efficaciously extract the signal.

By iteratively executing this protocol, it is feasible to perform a spatially resolved map of the LDOS. This map delineates the LDOS as a function of position and bias voltage, thereby revealing the electronic properties of the sample with remarkable spatial resolution and sensitivity.

2.3 Omicron Low-Temperature Scanning Tunneling Microscope

The Omicron Low Temperature Scanning Tunneling Microscope (LT-STM) represents a sophisticated ultra-high vacuum (UHV) instrument that enables both morphological and electronic characterizations of samples across a range of temperatures, representative upon the selection

of cryogenics (either Liquid Nitrogen at 77 K or Liquid Helium at 4.2 K). The instrument comprises three principal components: the load lock, the preparation chamber, and the analysis chamber. In this section, we delve into the functionalities and features of the LT-STM system, and how it is utilized in low-temperature STM experiments.

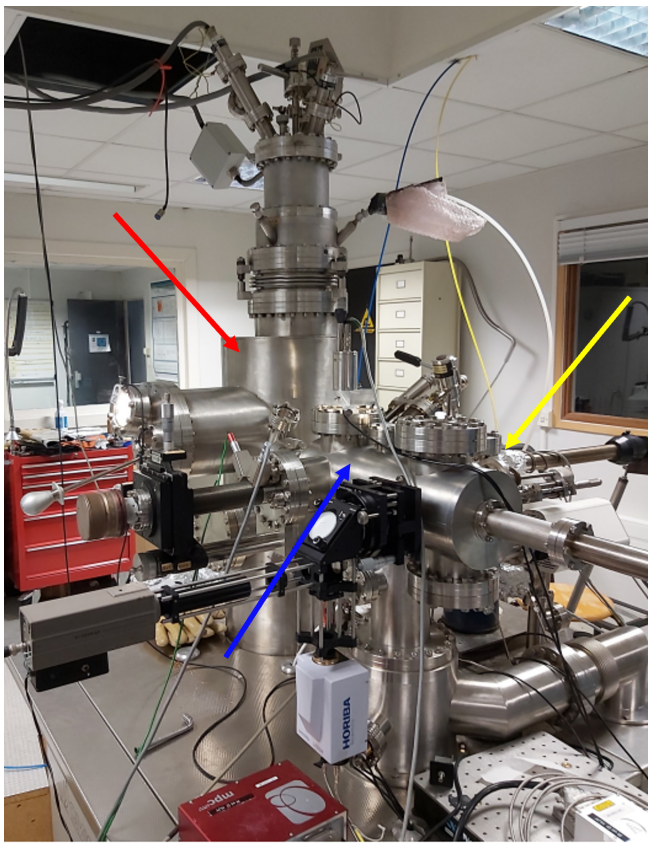

Figure 2.6: The Omicron Low Temperature Scanning Tunneling Microscope (LT-STM). The system is divided into three main parts: the load lock, the preparation chamber, and the analysis chamber, shown respectively with yellow, blue and red arrows.

2.3.1 Load-lock chamber

The load-lock chamber, depicted in Figure 2.6, serves as an intermediary between the UHV chambers and the ambient environment. This chamber is equiped with a sliding transfer rod, capable of accommodating up to three samples simultaneously. It is noteworthy that both the tips and samples designated for analysis are initially loaded into the load-lock chamber prior to being conveyed to the preparation chamber.

Access to the load-lock chamber is provided via a viewport that can be opened. This viewport is sealed with a viton gasket. A key advantage of employing viton gaskets over copper counterparts is that they do not necessitate replacement after each opening of the viewport, despite a limitation of the maximum bake-out temperature to 120°C and the attainable vacuum level.

Upon the introduction of new materials into the load-lock, it is first pumped to achieve high vacuum conditions using a turbomolecular pump. Subsequently, a bake-out at 120°C is performed for approximately 8 hours to eliminate typical air contaminants such as water vapor.

The load-lock chamber is crucial in the STM system as it acts as a vital interface between the UHV conditions and the external atmosphere. By safeguarding the maintenance of ultra-high vacuum conditions, which are imperative for accurate measurements and manipulations,

the load-lock chamber reinforces the reliability and precision of the data acquired.

2.3.2 Preparation chamber

The preparation chamber is specially designed to accommodate an array of preparatory processes essential for the conditioning of both samples and tips prior to analysis. The chamber encloses a primary manipulation stage that enables the preparation of semiconductor surfaces through either indirect resistive heating or the direct application of voltage. The temperature during these processes can be ascertained using a thermocouple fixed to the primary manipulation stage, or via an external pyrometer for temperatures exceeding 250°C.

For the preparation of metallic surfaces, the chamber employs an Ion Gun that utilizes neon (Ne) or argon (Ar) ions. Additionally, the chamber is furnished with an auxiliary electrical contact, which permits degassing tips up to 1200°C, a critical procedure for eliminating the tungsten oxide layer formed during the electrochemical etching process.

Moreover, the chamber is equipped with a Titanium Sublimation Pump (TSP), which is instrumental in sustaining an ultra-high vacuum ambiance with a base pressure of 5×10^{-11} Torr. Within the chamber, a sample storage stage with five slots is integrated alongside a manipulator capable of three-dimensional movement and axial rotation.

The manipulator is also equiped with a resistive heater, a thermocouple, and multiple electrical connections, facilitating the polarization of the sample or the establishment of a current through it. This attribute is particularly advantageous for heating resistive samples to sublimate native oxide layers, clean them, and facilitate surface reconstruction devoid of defects.

For non-resistive metallic samples, their surface preparation is performed through iterative cycles of ion sputtering and heating. Ion sputtering, typically executed with argon ions, is employed for the removal of contaminants, while subsequent heating via the manipulator resistive heater is utilized for surface reconstruction. This preparation may necessitate repetition to ensure comprehensive elimination of contaminants from the sample.

Lastly, the preparation chamber incorporates a specialized setup for a chemical modification of the sample surface, such as hydrogenation or nitridation, which involves a gas inlet and a tungsten filament. In this setup, the gas undergoes cracking via the filament heated to elevated temperatures, and the resultant ions are extracted by an electric field generated through the polarization of the sample.

2.3.3 Analysis chamber

The analysis chamber, as depicted in Figure 2.6, constitutes the central component of the system where the scanning tunneling microscopy takes place. This chamber is carefully maintained under UHV conditions, with a base pressure of 7×10^{-11} Torr at room temperature post-bake-out. Within this environment, the chamber accommodates the STM apparatus and is designed to hold up to six samples in a rotary carousel.

The STM unit housed within this chamber is interfaced with a dual-cryostat system for cooling. The exterior cryostat, charged with nitrogen, acts as a thermal shield. The interior cryostat, which can be charged with either nitrogen or helium, offers flexibility in selecting the operating temperature, depending on the cryogen employed. The conventional operating temperatures are 4 K (with liquid helium) and 77 K (with liquid nitrogen). The refilling intervals for the cryostats are contingent on the choice of the cryogen and experimental conditions.

A wobblestick is utilized for transferring samples between the carousel and the STM. Moreover, the analysis chamber is furnished with a piezoelectric scanner that facilitates the meticulous positioning of the STM tip.

The positioning of the STM tip with such high precision is vital for obtaining reliable data and insights into the surface properties of the samples under examination. The UHV conditions within the analysis chamber are crucial in minimizing contamination, thereby ensuring the integrity and accuracy of the measurements conducted with the STM.

2.4 Multi-probe STM

Following the discussion on the operation and components of a single-probe STM, this section will delve into an advanced and more versatile configuration, known as the Multi-Probe STM. The term "Four-Probe STM" refers to a specific variant of Multi-Probe STM that employs four probes. This instrument builds upon the fundamental scanning tunneling principles of conventional STM, augmenting it with the capability to perform multiple simultaneous measurements.

While the conventional single-probe STM is an indispensable tool in nanoscience and nanotechnology, allowing for the imaging of topographical features and local electronic structures of conductive samples, its scope of functionalities remains constrained. In contrast, the Four-Probe STM broadens the array of possibilities by employing multiple scanning tips simultaneously. This configuration can be metaphorically described as a "nano-multimeter" because it permits the measurement of transport properties at the nanoscale.

There have been several studies that have explored the capabilities and challenges associated with Multi-Probe STMs, exemplifying the potential advantages and intricacies that arise from employing a multi-probe setup [96,97]. The incorporation of multiple probes not only amplifies the instrument adaptability but also facilitates advanced experiments, such as simultaneous topographic and electronic measurements, or localized transport measurements which were not possible with a single probe.

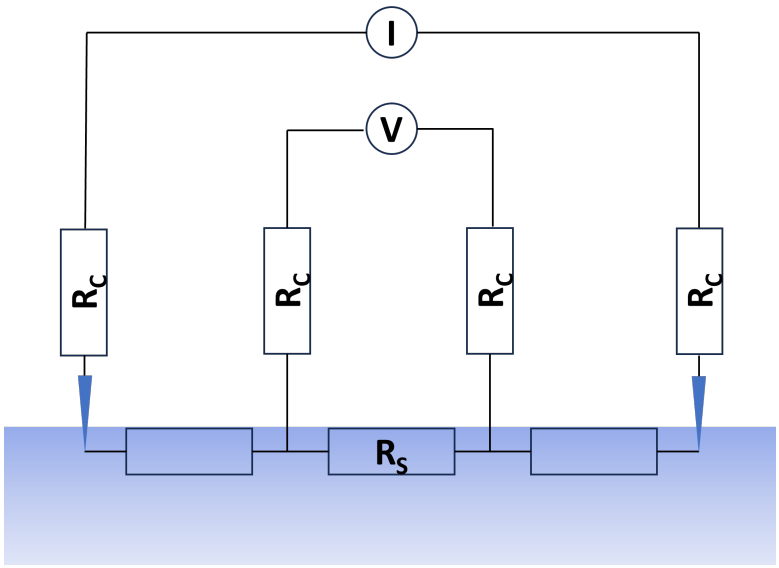

Figure 2.7: Schematic diagram of a 4-probe resistance measurement setup. R_S represents the sample resistance to be measured, R_C is the contact resistance, V denotes the measured voltage between the two inner probes, and I represents the injected current between the two outer probes. The sample is coloured in blue.

In a Four-Probe STM setup, as depicted in Figure 2.7, a voltage V is measured between the two inner contacts while a current I is injected through the two outer contacts. This configuration, known as the 4-point measurement technique, allows for simultaneous investigation of surface topography and local lateral electrical conductivity at different locations on a sample

surface. By using four individually controlled STM tips, the 4-point measurement technique can be employed to effectively avoid the challenge posed by contact resistance (R_C). In this setup, R_C in the injecting electrodes can be ignored as they can be of the order of MΩ due to the small contact area. This separation of current injection and voltage measurement ensures that the current flowing into the sample remains the same regardless of the contact resistances. The high resistance values of R_C in the voltmeter circuit minimize the current flowing through the voltmeter, and consequently, there is a negligible voltage drop. This method not only provides an accurate measurement of the sample resistance but also yields valuable insights into aspects such as carrier mobility and carrier concentration in the sample, when the sample is electrostatically controlled with a back gate.

Before delving into the intricacies of the Four-Probe STM technique at the microscopic scale, it is insightful to draw a comparison with the conventional macroscopic four-probe method. Understanding the distinction between these two scales and the nuances in the measurement techniques is essential for appreciating the capabilities and challenges of employing a Four-Probe STM in nanoscale studies.

2.4.1 Four-probe STM and its macroscopic analogue

A useful starting point for understanding the details of the four-Probe STM is to contrast it with its macroscopic counterpart, the macroscopic four-probe method. The latter is a well-established procedure for determining the resistivity of semi-conductive materials, a feature shared with the four-Probe STM. In the macroscopic method, the injected current travels through the outer contacts, and the voltage is measured across the two inner contacts, effectively canceling the influence of contact resistances.

In macroscopic four-probe measurements, the conductive path of an electrical current through a semiconductor material consists of several pathways:

- Through the surface states, which are tied to the material surface reconstruction.
- Through a space charge layer, located immediately beneath the surface.
- Through the material inherent bulk states, attributes that are unaffected by the surface conditions.

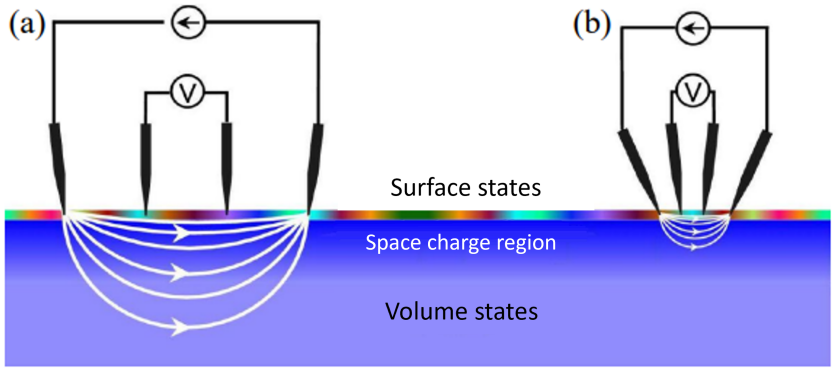

Figure 2.8: (a) Macro- and (b) micro-four-point probe techniques employed for electrical conductance measurement. [98]

Figure 2.8 illustrates the transition from macroscopic to microscopic techniques. This transition introduces a variety of unique attributes and complexities in a four-Probe STM setup.

2.4.2 Probe spacing and configurations in four-probe STM

As mentioned in the previous section, one of the key considerations in four-Probe STM is the configuration and spacing of the probes. These factors are critical to the accuracy of the four-Probe STM in extracting precise electrical properties, as they directly influence the path through which the current flows and, consequently, the measured resistance.

2.4.2.1 Arbitrary configuration

The Van der Pauw theorem, which is fundamental to four-point probe measurements, provides a mathematical framework for calculating the resistivity of an arbitrary, flat, and homogeneous sample of finite size. As depicted in Figure 2.9a, the theorem applies to a flat sample of arbitrary shape with negligible thickness, having four small contacts located at the perimeter.

The general equations for arbitrary configurations of the probes in the 3D and 2D cases are given by:

$$R_{4p}^{3D}(\vec{s_1},\vec{s_2},\vec{s_3},\vec{s_4}) = -\frac{\rho_{3D}}{2\pi}\left(\frac{1}{|\vec{s_3}-\vec{s_1}|}-\frac{1}{|\vec{s_3}-\vec{s_4}|}-\frac{1}{|\vec{s_2}-\vec{s_1}|}+\frac{1}{|\vec{s_2}-\vec{s_4}|}\right) \tag{2.31}$$

$$R_{4p}^{2D}(\vec{s_1},\vec{s_2},\vec{s_3},\vec{s_4}) = -\frac{\rho_{2D}}{2\pi}\ln\left(\frac{|\vec{s_3}-\vec{s_4}|\cdot|\vec{s_2}-\vec{s_1}|}{|\vec{s_3}-\vec{s_1}|\cdot|\vec{s_2}-\vec{s_4}|}\right) \tag{2.32}$$

where the vectors $\vec{s_i}$ (i=1,2,3,4) start from a common reference point $\vec{r_0}$.

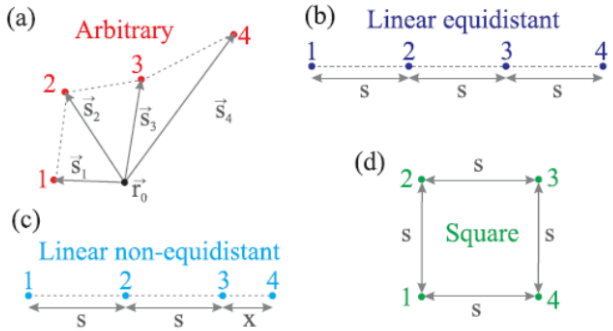

Figure 2.9: Schematic diagrams of the four probe configurations used in four-Probe STM: (a) Arbitrary configuration, allowing for flexible probe placements, (b) linear equidistant configuration, where probes are aligned in a straight line with equal spacing, (c) linear non-equidistant configuration, where probes are aligned in a straight line but with variable spacing, and (d) square configuration, useful for probing conductivity anisotropy in two perpendicular directions. [99]

2.4.2.2 Equidistant linear configuration

The equidistant linear configuration, depicted in Figure 2.9b, is a specific case of probe arrangement that benefits from the Van der Pauw theorem. In this configuration, the probes are arranged in a straight line, with equal spacing between them. The equations provided in this section are a simplification of the general equations from the Van der Pauw theorem, adjusted for the equidistant linear configuration. This configuration is particularly useful for studying homogeneous materials, as the equal spacing and linear alignment simplify the modeling and interpretation of the data. Also, the consistency in measurement conditions achieved by maintaining equal distances minimizes variability in results due to probe positioning.

For such materials that are both homogeneous and isotropic, and can be approximated as semi-infinite three-dimensional resistive mediums, the resistance R measured by a four-point probe in this configuration as a function of the distance d between the probes is given by the equation [99]:

$$R = \frac{\rho_{3D}}{2\pi d} \tag{2.33}$$

where ρ_{3D} is the bulk resistivity of the material.

However, this equation holds only for certain ranges of probe spacing. For larger distances, the current may penetrate to the bottom of the sample. This causes the field lines to compress due to the geometry, and an alternative equation becomes more relevant:

$$R = \frac{\rho_{3D} L}{S} \tag{2.34}$$

where L is the length of the measured area, and S is the cross-section of the sample.

When measuring the resistance of an infinite two-dimensional sheet using this configuration, the resistance is defined by:

$$R = \frac{\ln 2}{2\pi} \cdot \rho_{2D} \tag{2.35}$$

where ρ_{2D} is the sheet resistance, equivalent to the three-dimensional resistivity divided by the thickness of the sheet, $\rho_{2D} = \frac{\rho_{3D}}{t}$.

This configuration, while simple and effective for homogeneous materials, is limited in its versatility when it comes to studying materials with non-uniform properties. For anisotropic or inhomogeneous materials, the equidistant linear configuration may not provide comprehensive insights.

2.4.2.3 Non-equidistant linear configuration

In contrast to the equidistant linear configuration, the non-equidistant linear configuration involves a linear arrangement of the probes, but with varying distances between them. This setup is primarily advantageous due to its straightforward measurement process, which simplifies the examination of samples, even when they present heterogeneity or variable electrical properties across their surface. A visual representation of this configuration is shown in Figure 2.9c.

Mathematically, the non-equidistant configuration can still be analyzed in terms of resistance measurements like in the equidistant configuration, but the spatial variation in distances adds complexity to the interpretation. The resistance in the 3D and 2D cases as a function of distance x from the nearest tip and the distance s between the other three tips is given by [99]:

$$R_{4p}^{3D}(s,x) = \frac{\rho_{3D}}{2\pi}\left(\frac{1}{x} + \frac{1}{2s} - \frac{1}{s+x}\right) \tag{2.36}$$

$$R_{4p}^{2D}(s,x) = \frac{\rho_{2D}}{2\pi}\left(\ln\left(\frac{2s}{x}\right) - \ln\left(\frac{s}{x+s}\right)\right) \tag{2.37}$$

These equations are specialized forms of the general equations derived from the Van der Pauw theorem for non-equidistant configurations.

2.4.2.4 Square configuration

The square configuration is especially useful for analyzing anisotropic materials, which have directional dependence in their electrical properties. In this configuration, four probes are placed in a square pattern as shown in Figure 2.9d. This setup allows for examining the conductivity in two perpendicular directions without recontacting the tips.

The resistance R_{square} can be calculated using the equation [99]:

$$R_{square} = \frac{1}{2\pi\sqrt{\sigma_x \sigma_y}} \times \ln\left(1 + \frac{\sigma_y}{\sigma_x}\right) \tag{2.38}$$

where σ_x and σ_y are the conductivities in the two perpendicular directions.

Additionally, to ascertain the primary directions of conductivity, the square configuration can be rotated and the resistance can be measured with respect to the rotation angle θ. The resistance R as a function of the angle θ can be represented as:

$$R(\theta) = C \cdot \ln\left(\left(\frac{\sigma_x}{\sigma_y} + 1\right)^2 - 4\cos^2\theta \sin^2\theta \left(\frac{\sigma_x}{\sigma_y} - 1\right)^2 \left(\sin^2\theta + \frac{\sigma_x}{\sigma_y}\cos^2\theta\right)^2\right) \tag{2.39}$$

where $C = \frac{1}{2\pi\sqrt{\sigma_x \sigma_y}}$.

This rotational analysis is essential to pinpoint the major conductivity axes and provides valuable insights into the directional dependencies of the material electrical properties.

2.4.3 Omicron 4-Probe instrumentation

After discussing the general concepts of probe spacing and configurations in four-Probe STM, it is instructive to examine IEMN instrument that embodies these principles. The Omicron 4-Probe is a sophisticated instrument designed for multi-probe STM measurements, particularly in UHV conditions. It comprises a preparation chamber, an analysis chamber, and is equipped with multiple Nanoprobe tips.

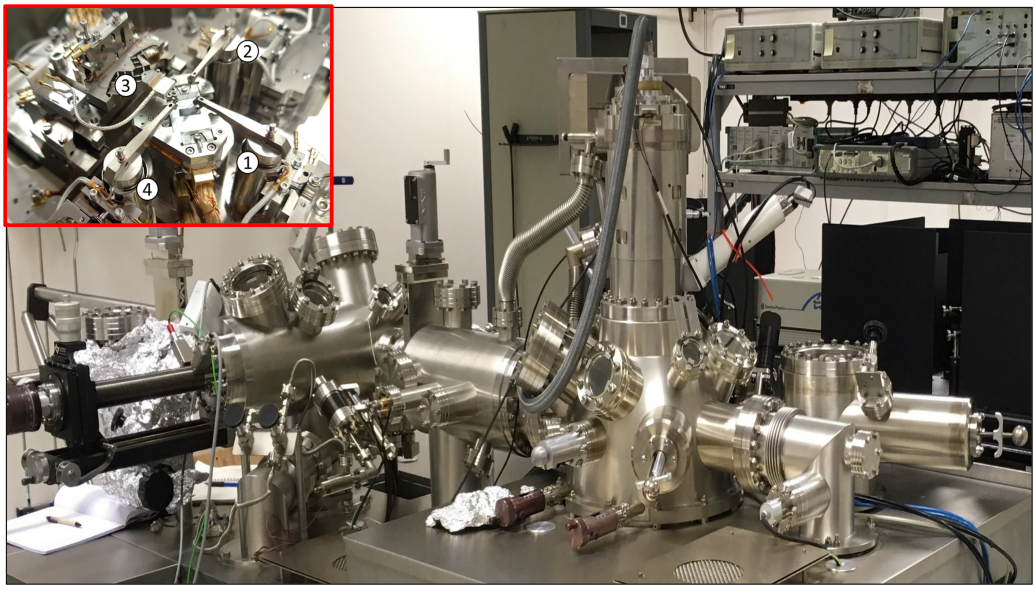

Figure 2.10: The Omicron 4-probe instrument and the 4 STM tip stage in the inset.

One of the distinguishing features of this instrument is the integration of a Scanning Electron Microscope (SEM), which provides complementary imaging techniques to STM. The SEM offers microscale imaging with an excellent depth of field, while the STM provides atomic-scale resolution. This combination enables precise tip positioning and complementary imaging techniques, enhancing the quality and range of information that can be obtained from the material surfaces at the atomic or nanometer scale. A load lock chamber with storage for six holders is present for the insertion of both tips and samples. Figure 2.10 shows the Omicron 4-Probe instrument present at IEMN.

Preparation Chamber: The preparation chamber is essential for in-situ preparation of both samples and tips under ultra-high vacuum conditions. It features storage for samples and tips and includes a manipulation stage that can be used for degassing tungsten tips with a tantalum electrical contact or preparing samples through direct current injection or resistive heating. The chamber is equipped with rotary and turbomolecular pumps as well as an ion pump to maintain ultra-high vacuum in the $10^{-9} - 10^{-10}$ mbar range.

Analysis Chamber: The analysis chamber is where the actual measurements are performed. It houses four scanners for the nanoprobe tips, of which one is equipped with a high-resolution scanner for atomically-resolved STM imaging, while the others consist of scanners with atomic-step height resolution. The tips can be precisely positioned in the X, Y, and Z directions, whereas the sample holder at the center of the chamber can be moved in the X and Y directions. The fine positioning of the tips is facilitated by a SEM (Gemini column) placed directly above the analysis chamber.

Nanoprobe Tips: The nanoprobe tips are made from tungsten wires, which are etched electrochemically. These tips are cleaned and degassed under ultra-high vacuum conditions in the preparation chamber to avoid contamination during measurements.

2.4.4 Electrical measurements

In the course of this research, three distinct electrical circuits have been employed to serve different experimental needs. These include the STM mode circuit utilizing Nanonis controllers, the circuit for transport properties and static I(V) measurements, which is equipped with Keithley meters, and a specialized circuit designed for pulse measurements that we will discuss more in details.

2.4.4.1 Specialized circuit for pulse measurements

The specialized circuit for pulse measurements, which includes a pulse generator, voltage amplifier, and an oscilloscope, is crucial for exploring the dynamic aspects of electronic transitions through time-resolved measurements. It also minimizes heating effects compared to static I(V) measurements. This setup is defined by a characteristic time of approximately 5μs, a result of its capacitance, imposing a limit for the shortest detectable electronic transition dynamics. The development of this circuit involved several stages, initially incorporating a preamplifier for current measurement, later replaced by a resistance R_{load} due to switching issues and the current limitations of the Nanoprobe. In order to control the setup, a LabVIEW program was developed by Yevheniia CHERNUKHA, a postdoc in our group, to balance high temporal resolution with manageable data file sizes, a task complicated by the use of a sophisticated oscilloscope.

2.5 Molecular Beam Epitaxy

2.5.1 Introduction and historical background

From the time scientists understood that the properties of materials depend on their microstructure, one can think about questions once asked by the physicist Richard Feynman: "What could we do with layered structures with just the right layers? What would the properties of materials be if we could really arrange the atoms the way we want them?". Therefore, scientists were motivated to design structures that produce specific and desired behavior.

Vapor and liquid epitaxy techniques have been employed for the growth of various semiconductor materials; the former offers rapid growth rates, while the latter is known for producing

high-purity films [100]. However, these methods require growth at high temperature with a lack of uniformity in film thickness, which can be a hindrance in device processing applications. There was a need for a new technique that could grow materials at lower temperatures while maintaining higher purity and fewer defects.

In the late 60s, a revolution in surface analysis occurred, and a new growth technique, Molecular Beam Epitaxy (MBE), was implemented. Initially, the MBE process was developed to study surface–vapor interactions with a compact mass spectrometer [101] and quantum phenomena predicted by Esaki and Tsu [101]. Later in 1969, Arthur, LePore and Cho successfully grew epitaxial GaAs films for the first time by MBE, using temperatures lower than 800°C compared to common growth techniques that can exceed 1000°C [102]. This marked the beginning of a new era in the production of high-quality materials, extending beyond the III-V semiconductor family. Indeed, the MBE process succeeded in growing other kinds of semiconductors, metals, and insulators. As a consequence, the electronic industry, including diodes, transistors, and integrated circuits, improved in terms of technological value thanks to such high-quality materials.

One of the key features of the MBE process is the ability to perform real-time analysis of the surface structure. During the experiment, this is typically performed using Reflection High-Energy Electron Diffraction (RHEED) [103] [104].

2.5.2 Components and growth process

To achieve the purity and precision for which MBE is renowned, the apparatus is configured with a set of essential components. Notably, it operates in UHV conditions (pressures below around 10^{-9} Torr) to ensure an environment free of contaminants. UHV is crucial in MBE to prevent the incorporation of impurities into the growing film, thereby allowing for high-quality epitaxial growth.

Operating under such UHV conditions, effusion cells, also known as Knudsen cells, play a pivotal role in the MBE process. These cells contain the source material, which is heated to a temperature at which it begins to sublimate or evaporate. The evaporated atoms or molecules are directed out through a small opening, generating a directed beam with a low density of particles, known as a molecular beam. This beam travels toward the substrate without interacting with other gases, due to the UHV conditions.

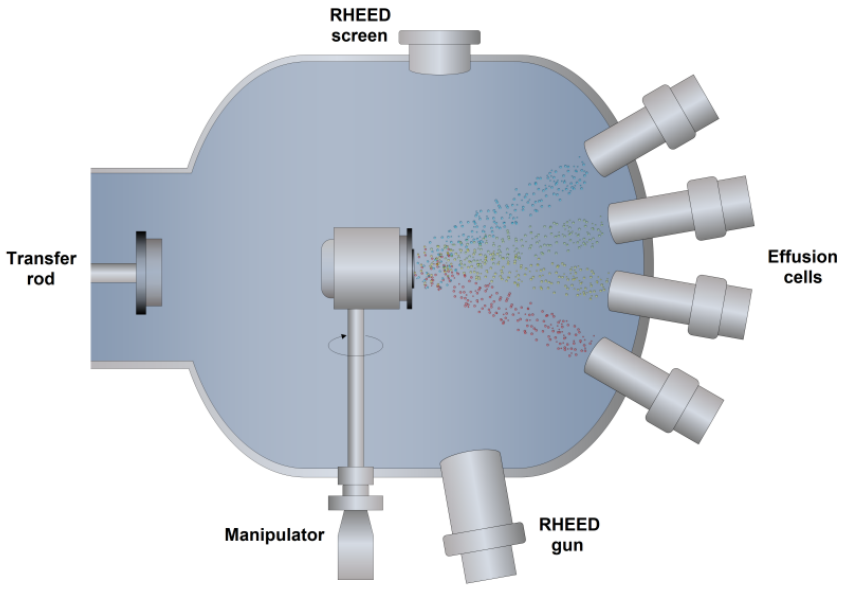

Figure 2.11: Sketch of a MBE growth chamber. [86]

In MBE, growth rates are typically about one monolayer per second. Beam controllers, consisting of fast-action shutters with operational times shorter than one second, allow for the control of the thickness of grown layers with an accuracy of less than a monolayer. This precise control enables layers with different chemical compositions to be grown on top of each other, with atomically abrupt interfaces.

The substrate holder is another critical component. It not only holds the substrate but can also often be rotated and heated. This ensures that the substrate is at the optimum temperature for the atoms or molecules to attach, migrate, and anneal into their preferred lattice positions.

Furthermore, real-time monitoring is essential in MBE to precisely control the growth of atomic layers. Among the monitoring systems, RHEED stands out and is widely used in MBE setups. RHEED operates by directing a beam of high-energy electrons at the surface of the substrate at a shallow angle. This grazing incidence minimizes disturbance to the molecular beams, making RHEED ideal for in-situ monitoring. The diffraction pattern generated by the scattered electrons provides vital information about the surface structure of the growing material. By analyzing changes in the pattern, one can infer the growth rate and even the crystallographic orientation of the layers. These data are crucial for making real-time adjustments, ensuring high precision and quality in the epitaxial growth process.

As depicted in Figure 2.11, the growth chamber is where the molecular beams are directed onto the substrate to form epitaxial layers. For this work, the attached chambers play crucial roles in the preparation and analysis of the materials. Beams of elemental tantalum (Ta) and selenium (Se) are directed onto the substrate to form epitaxial layers of 1T-$TaSe_2$.

2.6 COMSOL Multiphysics

COMSOL Multiphysics is a versatile simulation software package that employs finite element analysis to model and solve complex physical phenomena across a wide range of domains. It offers various specialized modules such as the AC/DC Module for electromagnetics, the Heat Transfer Module for thermal studies, the Structural Mechanics Module for mechanical systems, among many others.

In this thesis, the AC/DC Module was specifically utilized to simulate the electric field distribution in $GaMo_4S_8$ bulk material through the modeling of the 4-probe measurement method. The 4-probe measurement is an experimental technique widely used for measuring the electrical properties of materials. Simulating this method provides insights into the electric field behavior and characteristics of $GaMo_4S_8$, which are crucial for understanding the material properties under different conditions, considering various parameters such as the applied voltage, size of the sample, and size of the electrodes.

Simulation plays a critical role in understanding and interpreting physical phenomena, especially when it is not feasible to obtain explicit solutions or perform exhaustive experimental analysis. The ability to simulate the behavior of systems based on theoretical models and inputs can provide valuable insights and corroborate experimental data. Real-world physical systems are often too complex to model accurately using analytical methods. The finite element analysis employed by COMSOL is invaluable in this regard, allowing for the approximation of solutions to boundary value problems and partial differential equations, which are fundamental to physical systems.

Since it is commercialization in 1998, COMSOL has evolved into a versatile and robust tool for multiphysics simulations. Its development has been driven by the increasing demand for accurate, reliable, and efficient tools to model and solve multifaceted physical systems. For instance, COMSOL has expanded its range of modules to cater to a broader spectrum of applications, from acoustics to chemical engineering. It has also made strides in improving the accuracy and efficiency of its simulations through more advanced solvers and algorithms.

Additionally, the user experience has been enhanced with more intuitive interfaces, as well as integration capabilities with software such as MATLAB and various CAD tools.

This section will provide an introduction to COMSOL Multiphysics, with a particular focus on the AC/DC Module, which was specifically used in this thesis for relevant simulations. The subsequent subsections will explore its practical application and how the simulation results can be interpreted and utilized in conjunction with experimental data.

2.6.1 AC/DC module: An overview

The AC/DC Module is one of the specialized modules offered within COMSOL Multiphysics. It provides a unique environment for simulating AC/DC electromagnetics in both 2D and 3D, making it particularly powerful for detailed analysis of coils, capacitors, and electrical machinery. This module is used for simulating static and low-frequency electromagnetic fields and is grounded in solving the Maxwell's equations, which are the fundamental equations for electromagnetism.

These equations describe how electric and magnetic fields interact with each other and with charges and currents. Specifically, in the context of the AC/DC Module, the focus is on solving the time-dependent or frequency-dependent forms of Maxwell's equations to analyze how electric and magnetic fields behave in different materials and under various conditions. This involves dealing with the four Maxwell's equations, namely, Gauss's law, Gauss's law for magnetism, Faraday's law, and Ampère's law with Maxwell's addition. The Maxwell's equations are stated as:

- Gauss's Law: $\nabla \cdot \mathbf{E} = \frac{\rho}{\varepsilon_0}$
- Gauss's Law for Magnetism: $\nabla \cdot \mathbf{B} = 0$
- Faraday's Law: $\nabla \times \mathbf{E} = -\frac{\partial \mathbf{B}}{\partial t}$
- Ampère's Law with Maxwell's Addition: $\nabla \times \mathbf{B} = \mu_0 \mathbf{J} + \mu_0 \varepsilon_0 \frac{\partial \mathbf{E}}{\partial t}$

Understanding these equations and the assumptions or approximations made in solving them is crucial for interpreting the results of simulations conducted using the AC/DC Module.

The AC/DC Module enables several types of electromagnetic field simulations, including electrostatics, electric currents in conductive media, magnetostatics, and low-frequency electromagnetics. It accommodates diverse material properties such as inhomogeneous, fully anisotropic materials, media with gains or losses, and complex-valued material properties. Moreover, the module supports infinite elements for the modeling of unbounded domains.

In this thesis, the AC/DC Module is employed to simulate the time-independent electric field distribution in samples. Understanding the distribution of electric fields is vital for the analysis of numerous physical phenomena and applications such as electrostatic interactions, capacitive sensing, and electric field-driven material transport in microfluidic devices. Through the simulations, we will examine how different parameters, such as applied voltage, size of the sample, and size of the electrodes, influence the electric field distribution.

The AC/DC Module also offers capabilities for the direct computation of lumped parameters like capacitances and inductances and the calculation of electromagnetic forces. Furthermore, it is fully multiphysics enabled, which allows users to couple it with any other interface in COMSOL Multiphysics for more comprehensive analyses. For instance, one can simulate the current in the coils using the AC/DC Module and couple it with the heat equation in COMSOL Multiphysics or the Heat Transfer Module to analyze heat distribution in a motor.

Features of the AC/DC Module:

- **Defining Material Properties**: The AC/DC Module provides comprehensive tools for characterizing materials by enabling the definition of complex properties such as anisotropy, inhomogeneity, and complex permittivity. The meticulous characterization of materials, including orientation-dependent properties, is essential for accurately simulating real-world materials and capturing their electromagnetic behavior.

- **Setting Boundary Conditions**: With extensive control over boundary conditions, the AC/DC Module is instrumental in modeling physical constraints and interactions at interfaces accurately. It includes options for setting electrical or magnetic insulation conditions, continuity conditions ensuring smooth transitions across material boundaries, and more, thereby enabling a realistic representation of physical systems.

- **Enabling Multiphysics Coupling**: The AC/DC Module integration within the COMSOL environment allows for seamless multiphysics coupling, essential for simulating the complex interplay between electromagnetic fields and other physical phenomena such as thermal effects, structural mechanics, or fluid flow. This feature is indispensable in studying real-world applications involving multiple physical interactions.

- **Using Advanced Solvers**: Equipped with sophisticated numerical solvers, the AC/DC Module excels in handling both static and time-dependent analyses. These solvers are grounded in robust mathematical frameworks and are optimized for solving the Maxwell's equations governing electromagnetic phenomena with high accuracy and efficiency. The choice and configuration of solvers are pivotal for ensuring the reliability of simulations.

2.6.2 Setting up simulations in COMSOL

Setting up simulations in COMSOL Multiphysics involves a series of steps that are generally common across its various modules. Understanding these steps and how to effectively implement them is crucial for obtaining accurate and reliable results. This subsection provides an overview of these steps, which include geometry creation, defining material properties, applying boundary conditions, meshing, solving, and post-processing for analysis. Specifically, we will focus on how these steps are applied to simulate the electric field distribution within the context of this research.

2.6.2.1 Geometry creation

Creating the geometry of the model is the first step in setting up a simulation in COMSOL. It is essential to define shapes and structures that closely resemble the physical system under investigation. For simulations involving the AC/DC Module, it's important to consider aspects such as the size and shape of elements relevant to electric fields. Additionally, the scale is an essential aspect to consider since the behavior of the electric field can be scale-dependent.

In the simulations conducted for this research, the geometry consisted of a 3D block to represent $GaMo_4S_8$ crystals as shown in Figure 2.12. On the top plane we add circles that represent the tips in contact with the sample. This geometry was chosen to closely represent the configuration needed to analyze the distribution of the electric field under specific conditions.

2.6.2.2 Defining material properties

Defining material properties is a critical step following the creation of the geometry. In simulations focusing on electric field distribution, properties such as electrical permittivity and conductivity are of paramount importance. These properties govern how the material responds

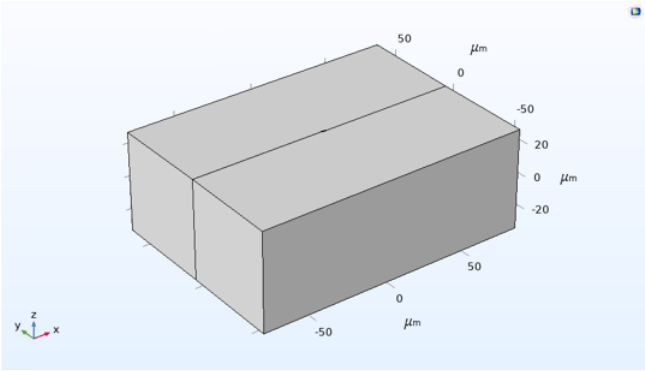

Figure 2.12: Geometry used for the electric field distribution simulations.

to electric fields and consequently affect the distribution and strength of the fields within the material.

Initially, for the simulations conducted in this research, tungsten was used to represent the 4-probe tips. Tungsten is part of COMSOL standard material library, and therefore, its material properties were directly sourced from the library without the need for manual input.

Moreover, materials can exhibit various complexities in their constitutive relationships with electric and magnetic fields. These complexities need to be considered when defining material properties:

- **Inhomogeneous Materials**: Constitutive parameters in inhomogeneous materials vary with spatial coordinates. This means different field properties prevail at different parts of the material structure.
- **Anisotropic Materials**: For anisotropic materials, the field relationships at any point differ for different directions of propagation. A 3-by-3 tensor is necessary to properly define the constitutive relationships for anisotropic materials. If the tensor is symmetric, the material is often referred to as reciprocal. Special cases include uniaxially anisotropic materials where two of the diagonal entries of the tensor are equal, and biaxially anisotropic materials where none of the elements have the same value [105].
- **Nonlinear Materials**: Nonlinearity arises from variations in permittivity or permeability with the intensity of the electromagnetic field. It also includes hysteresis effects, where the history of the field distribution influences the physical properties of the material.
- **Dispersive Materials**: Dispersion describes changes in a wave velocity with wavelength. In the frequency domain, dispersion manifests as a frequency dependence of the constitutive laws.

In the context of this research, the primary material of interest is $GaMo_4S_8$ bulk material. Since it is not part of COMSOL standard material library, it was necessary to define its properties manually. The relative permittivity ε_r and electrical conductivity σ of this material were set to 9 and 2.6 S/m, respectively [39].

2.6.2.3 Applying boundary conditions

Boundary conditions are essential in simulations as they dictate how the model interacts with its surroundings and are crucial for ensuring that the physical reality is accurately represented. In the context of electromagnetic simulations using the AC/DC Module, several boundary conditions are particularly relevant:

- **Electric Insulation**: This condition models boundaries where there is no flow of electric charge by setting the normal component of the electric field to zero.
- **Continuity**: Used at interfaces between different materials, continuity conditions ensure that there are no discontinuity in the electric field by enforcing the condition that the tangential component of the electric field is continuous across the boundary.
- **Symmetry**: In cases where the geometry under study has symmetrical properties, symmetry boundary conditions can be applied to reduce the computational domain and simulation time while maintaining accuracy.
- **Perfect Electric Conductor (PEC)**: This condition is used to simulate surfaces that are perfect conductors of electricity by setting the tangential component of the electric field to zero.

In our case, particular emphasis was placed on current conservation and electric isolation. The equations ensuring current conservation and electric isolation are:

$$\begin{aligned} \nabla.\vec{J} &= Q \\ \vec{J} &= \sigma\vec{E} + \vec{J}_e \\ \vec{E} &= -\nabla V \\ \vec{n}.\vec{J} &= 0 \end{aligned} \tag{2.40}$$

where $\vec{J}$ represents the total current density, Q is the charge density, σ is the electrical conductivity, $\vec{E}$ is the electric field, $\vec{J}_e$ the external current density, V is the electric potential, and $\vec{n}$ is a unit vector normal to the surface.

These equations are critical in accurately modeling the electric field distribution within $GaMo_4S_8$ bulk material by ensuring that the electric current is conserved and that there is no current flow through insulated surfaces.

Furthermore, it is important to highlight that simplifying the geometry is a practical approach to reduce computational demand, especially in large or complex systems. One effective method is 'Truncating Infinite Domains'. In this approach, the geometry is shortened in cases where the model stretches towards infinity or where the solution changes very little. By doing this and applying an appropriate boundary condition, such as setting the electric field to zero at the open boundary, the model becomes more manageable without significant loss of accuracy. This is particularly useful in static and quasi-static models, where it is essential that the truncation does not affect the core behavior of the system.

2.6.2.4 Meshing

Meshing is the essential process of subdividing the geometry of the model into discrete elements for numerical solutions of governing equations in simulations. The choice of mesh density and quality significantly affects the accuracy of the simulation results and must meet a balance between accuracy and computational efficiency.

The mesh density in electric simulations depends on various factors, including the geometry complexity, material properties, and electric field gradients. A finer mesh is generally required in regions with geometric complexity or rapid changes in the electric field. There are two primary types of mesh used in simulations: structured and unstructured. The structured mesh consists of regular grid patterns and is well-suited for simple geometries. In contrast, unstructured mesh is adaptable to complex geometries with irregular patterns.

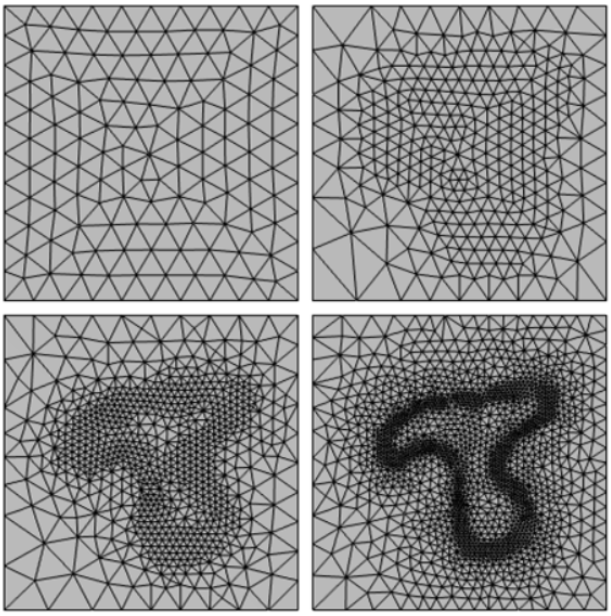

Figure 2.13: Mesh adaptivity employed for precision in 2D simulation. [106]

Mesh refinement, particularly Adaptive Mesh Refinement (AMR), is instrumental in enhancing the mesh density in regions demanding higher accuracy, such as areas with rapid changes in the electric field or near boundaries and interfaces. AMR can be employed to dynamically adjust the mesh during the simulation, focusing on regions where the electric field is changing rapidly or where higher accuracy is needed, and refining the mesh in those areas as seen in Figure 2.13. This adaptive approach is highly efficient as it ensures that computational resources are focused on the critical regions of the model without unnecessarily increasing the mesh density everywhere.

In summary, smart mesh design and refinement strategies are imperative to ensure the reliability and accuracy of electric field simulations. The mesh must be fine enough to capture critical features of the electric field, while transitions between different mesh densities should be smooth to minimize numerical errors.

2.6.2.5 Solving and post-processing

During the solving phase in COMSOL, the mathematical equations characterizing the physical phenomena under investigation are numerically solved. COMSOL affords users the ability to select appropriate solvers and fine-tune their configurations to optimize accuracy and computational efficiency. This selection process is critical, especially in electric field simulations, as various solvers have diverse efficacies in addressing the intricate interactions within electric fields [107] [108].

Subsequent to the solving phase, the post-processing stage is crucial for the extraction, analysis, and interpretation of the data yielded by the simulation. COMSOL encompasses an array of post-processing tools [109], encompassing visual aids such as plots and graphs as well as tabulated data. These tools facilitate a deeper understanding of the underlying physical properties, such as the distribution of electric fields and current densities.

Throughout this section, we have delved into the integral steps and considerations in utilizing COMSOL Multiphysics for electric field simulations. We navigated the path from geometry creation and defining material properties, to refining meshes for accurate results, and finally post-processing the data. The effective execution of these steps is indispensable for ensuring the reliability and accuracy of simulation outcomes.

Chapter 3

Electric field induced transitions in Mott insulator $GaMo_4S_8$

3.1 Introduction

The Mott insulator family encompasses a wide range of materials, including both large gap (>1 eV) variants such as cuprates, manganites, irridates, and nickelates, as well as narrow gap (0.1 - 0.5 eV) members like vanadium sesquioxide (V_2O_3). Especially significant within the narrow gap category are the transition metal chalcogenides in the AM_4X_8 family. Among these, $GaMo_4S_8$, a prominent member with a gap of 356 meV, has received a specific interest.

Distinctively, $GaMo_4S_8$ differentiates itself from other Mott insulators with its well documented electric phase transition at room temperature [35, 110]. While materials like NiS_2 and $GaTa_4Se_8$ also exhibit phase transitions, they typically require low temperature conditions [24]. Previous works using Mott materials further underscore this potential by demonstrating a Leaky Integrate-and-Fire (LIF) function. $GaMo_4S_8$ room temperature transition shows potential for ultra compact artificial neurons at ambient temperature.

Moreover, Cr-doped V_2O_3 and $GaTa_4Se_8$ necessitate low-temperature conditions for phase transitions that could introduce complexities. For instance, transport experiments performed at these temperatures could lead to a temperature gradient in the Nanoprobe setup, described in the Chapter 2, as only the sample would be cold. This temperature differential might affect the material local behavior, possibly causing artifacts or inducing non-uniform transitions. Additionally, the threshold voltage for the transition shows an exponential relationship with temperature.

In this chapter, we use the capabilities of the Nanoprobe at IEMN, which allows to meticulously characterize the electric field-induced transitions in $GaMo_4S_8$ both spatially and temporally. Through this tool, we shed light on the dynamics of the transition and complement our experimental findings with simulations to understand the electric field distribution. As our exploration advances, we uncover a multi-dimensional transition within the material, from the volatile electric Mott transitions to topographical transformations and profound chemical alterations. These accumulated discoveries provide a deeper understanding of the complex behavior inherent to this fascinating material.

3.2 Transport properties at low electric field

3.2.1 Indexing $GaMo_4S_8$ samples based on their preparation

Single crystals of $GaMo_4S_8$ were prepared at the Institut des Sciences Chimiques in Rennes through a non-congruent melting method involving molybdenum (Mo), molybdenum sulfide

(MoS_2), and gallium sulfide (Ga_2S_3). Controlled heating and cooling stages yielded large octahedral crystals typically exceeding 500 μm. For complete synthesis details, readers are referred to [35].

Figure 3.1 illustrates the geometries of the $GaMo_4S_8$ samples used in this study, divided into two main series based on the environment, in which they were cleaved, either outside or inside the Ultra High Vacuum (UHV) chamber of the Nanoprobe:

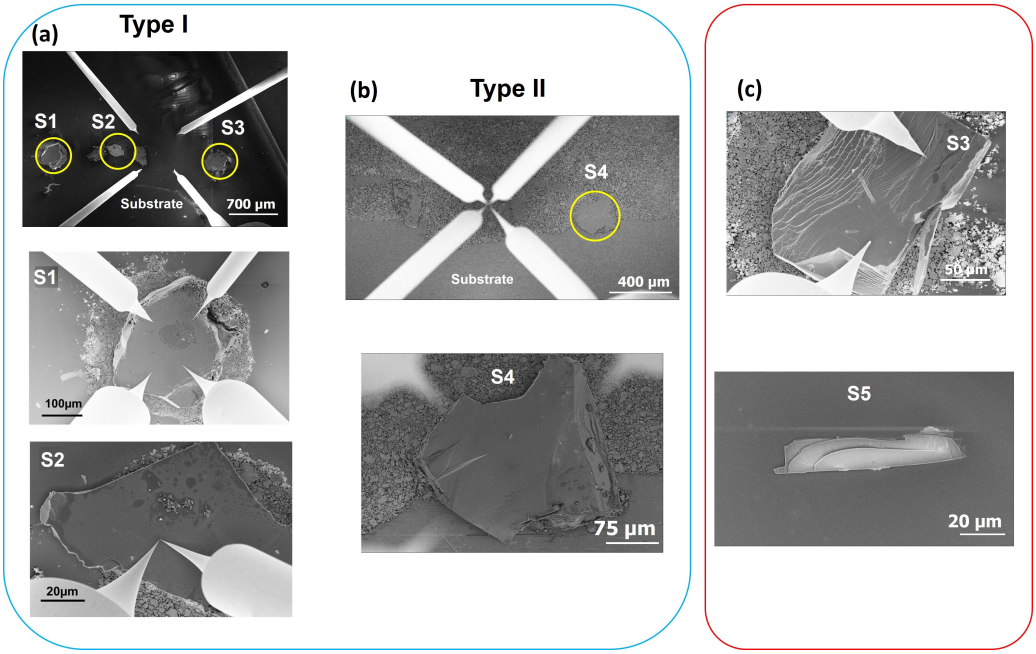

Figure 3.1: Samples utilized in this study, with varying preparation and treatment methods. Series A in blue shows (a) samples S1, S2 and S3 heated inside the nanoprobe. (b) Sample S4 was heated externally. Series B in red shows at the top of (c) the largest part of sample S3 after the cleavage and, at the bottom, the smallest piece labelled as sample S5.

Series A: this series consists of samples cleaved outside UHV. Within this series, there are two types of samples:

- **Type I** (Figure 3.1a) includes samples S1, S2, and S3, which were affixed to a gold p-doped silicon substrate using conductive glue suitable for UHV environments and annealed at 150°C for 1 hour in UHV conditions in the preparation chamber.
- **Type II** (Figure 3.1b) consists of samples glued to a molybdenum substrate and externally heated in an oven. Sample S4 is at the heart of our study.

Series B: this series includes one unique sample cleaved inside UHV from sample S3. The cleavage was performed in the nanoprobe by exerting a vertical pressure on the S3 sample with one of the tips, resulting in sample S5. This UHV clived sample corresponds to a piece of the detached sample part in Figure 3.1c, that has been tilted sideways with one tip to expose the UHV-clived face on top, has shown in the same figure.

Once the samples loaded in the microscope, it was crucial to accurately determine their thickness. For samples in Series A (S1, S2, S3, and S4), the thicknesses were measured by comparing the height of the sample and the substrate, a process facilitated by the precise vertical control of the piezoelectric elements within the nanoprobe. Conversely, the thickness of sample S5 in Series B was estimated by measuring the width of the cleaved part from the SEM image before it flipped and faced the substrate. This measurement determined the thickness of S5, following a vertical cleavage from sample S3.

Table 3.1 summarizes the thicknesses of the studied samples.

Sample	Thickness (µm)
S1	74
S2	42
S3	61
S4	35
S5	5

Table 3.1: Thickness measurements for the samples used in this study.

3.2.2 4-probe resistivity of $GaMo_4S_8$ samples

Resistance measurements were performed on samples S1, S2, and S3 with the 4 STM tips of the Nanoprobe. The current was injected through the outer tungsten tips and the potential drop measured across the inner pair. Figures 3.2a, b, and c show SEM images of the positioning of the 4 tips on top of each sample. The measurements of the resistance was repeated for different equidistant separations d between the tips. The variation of the resistance as a function of d was then plotted in Figures 3.2d, e, and f. As seen in the chapter Experimental techniques, the relationship between the resistance and resistivity is not trivial in the general case where electrodes placed on the sample surface. Moreover, here the interelectrode distance is of the same order as the sample thickness, thus one cannot use the simple analytic relationships in the 1D, 2D or 3D limit.

To determine accurately the resistivity from the 4P resistance measurements, finite element simujlations using Comsol have been performed. To simulate the resistance measurements, we modeled the samples (S1, S2, S3) in COMSOL as blocks, reflecting the dimensions and geometries of the experimental samples. The mesh used in the simulations was specifically adapted to cover the size of the tips and their contact area (which was determined using the SEM of the nanoprobe), ensuring a highly detailed representation of the contact points. Figures 3.2g, h display the modeled samples using regular slab of thickness, length and width corresponding to the measured sample sizes with the corresponding mesh used in the simulations. The resistivity of the $GaMo_4S_8$ sample was then adjusted until the simulated $R(d)$ plots matched the experimental data, as illustrated in Figures 3.2d, e, and f.

In this fit, the resistivity is the only free parameter. The simulated $R(d)$ plots provide insight into the relationship between resistance and probe distance. The variation in resistance as a function of the probe distance can be appreciated by considering the streamlines of the current flow as demonstrated in the two sketches of Figure 3.2d. For larger distances, the current flows through the entire volume of the material, mirroring the macroscopic resistance measurement depicted by $\rho d/S$, where ρ denotes the resistivity, d the inter-electrode distance, and S the cross-sectional area. For shorter distances, however, the current lines do not reach the bottom of the sample. The resistance is then proportional to the resistivity divided by d. The measured 4P resistance series thus covers the electrode configuration range between the 1D and 3D limits.

This fitting process enabled us to accurately determine the resistivity values for samples S1, S2, and S3, indicated on Table 3.2. The obtained resistivity values were compared to the literature-reported resistivity for $GaMo_4S_8$ crystals, measured at room temperature, which is $32\,\Omega\,\mathrm{cm} \pm 24\,\Omega\,\mathrm{cm}$ [35].

Within the reported literature range, the calculated resistivity affirms the robustness of the simulation and experimental methods, and verify the quality of the $GaMo_4S_8$ samples used in this study. The difference of resistivity between the 3 samples may be attributed to the

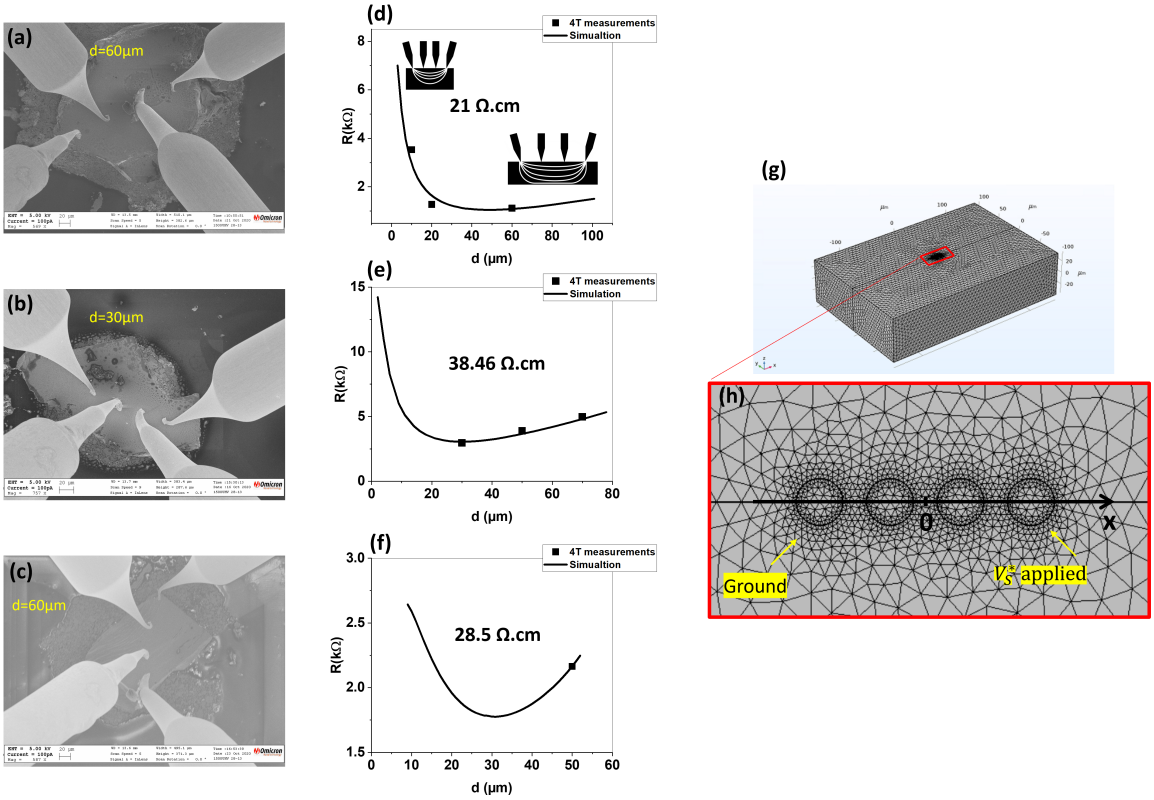

Figure 3.2: (a), (b) and (c) SEM images of samples S1, S2 and S3 respectively, and the 4 tips used to measure the 4-probe resistance. (d), (e) and (f) Plots of 4-probe resistance measured as a function of the inter-electrode distance (Symbols) of sample S1, S2 and S3 respectively, and the simulated R(d) (Line). (g) The block used in COMSOL to simulate the sample. (h) Zoom on the top surface of the block showing 4 cirles which correspond to the surface contact between the probes and the sample.

Sample	Resistivity ($\Omega\,$cm)
S1	21
S2	38.46
S3	28.5

Table 3.2: Resistivity values for samples S1, S2, and S3.

errors due to the simplified sample geometry and estimated lengths, or to some variation in the sample composition, in the bulk or only at the surface. The insights gained through this study enable us to confidently proceed with the investigation of the electric field distribution within the samples.

3.2.3 Mott insulator-metal interface

At the junction between a metallic electrode and a semiconductor, the discontinuity between the density of states gives rise to interfacial effects such as Schottky barriers and contact resistance. Whereas such effects are well documented for conventional semiconductors, only a few studies have been done on correlated materials such as $GaMo_4S_8$. The Nanoprobe is a powerful tool to study these complex interfacial phenomena, and because the experiments can be performed with 2-probe or 4-probe configurations.

3.2.3.1 Contact resistivity

One common and significant contribution to the measured resistance in two-probe setups is the contact resistance, an unavoidable phenomenon at the interface between the probe and the sample. In the two-probe setup, the resistance measurement includes not only the sample intrinsic resistance but also the contact resistance at each probe. This relationship is described by the equation:

$$R_{2P} = R_{4P} + 2 \cdot R_C \tag{3.1}$$

where R_{2P} is the total resistance measured in the 2-probe configuration, R_{4P} is the intrinsic resistance of the material measured in the 4-probe configuration, and R_C is the contact resistance at each probe. Here the resistance of the wires (few ohms) are neglected compared to the sample and contact resistances.

Figure 3.4a shows the 2-probe I(V) characteristic taken at a 10μm distance between the probes. It was acquired from 0 to 1V, and from 0 to -1V. The 2-probe resistance R_{2P} was determined to be approximately 500 kΩ. It is worth mentionning that R_{2P} was measured for different samples (S1, S2, S3 and S5) and probe distances. The results are shown in Figure 3.4d. It is found that R_{2P} is almost constant as a function of the probe distance. The 4-probe resistance R_{4P}, measured at the same inter-electrode distance 10μm for sample S2 (Figure 3.2e), was found to be 5 kΩ. Using these measurements, the contact resistance R_C was calculated as:

$$R_C = \frac{R_{2P} - R_{4P}}{2} = 247.5k\Omega \tag{3.2}$$

Remarkably, this contact resistance is two orders of magnitude higher than the intrinsic resistance of the $GaMo_4S_8$ sample. This result emphasizes the significant impact of the contact resistance in our measurements and underscores the importance of accounting for it in the analysis. We further explored the characteristics of this contact resistance by calculating the contact resistivity, a property crucial for understanding the interfacial behavior. Using the equation [111]:

$$\rho_c = R_C \cdot A_c \tag{3.3}$$

where ρ_c is the contact resistivity, and A_c is the contact surface area. The radius of the contact surface area was determined to be 1μm from the SEM images of the tip diameters. Combining this with the previously calculated contact resistance R_C, the contact resistivity ρ_c was determined to be approximately $7.78 \times 10^{-3}\,\Omega \cdot cm^2$.

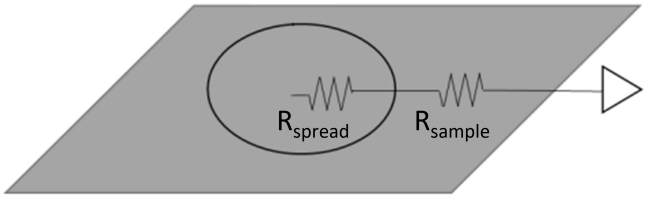

Figure 3.3: Schematic of the spreading resistance showing the contact point (black circle) between the probe and the sample. Adapted from [112].

One explanation of this high contact resistance could be the spreading resistance [113]. It refers to the resistance that current faces as it moves outward from a point of contact into the broader material (Figure 3.3). This form of resistance is particularly significant in settings with small contact areas, as is common in our experimental setup. It arises because the electrical

current, initially confined to a small area, must spread through a larger volume of the material, thereby encountering more resistance. Consequently, spreading resistance forms a crucial part of the overall contact resistance, affecting the accuracy and interpretation of our electrical measurements.

For a circular contact of radius r and a homogeneous sample of resistivity ρ, the spreading resistance is given by the expression:

$$R_{SP} = \frac{\rho}{4r} \tag{3.4}$$

In our case, the curvature radius is ≈1µm, a spreading resistance of 80 kΩ is obtained, smaller than R_c but of the same order of magnitude.

On the other hand, the obtained contact resistivity for our $GaMo_4S_8$ sample is consistent with surface resistivity measurements reported in the literature for other materials. For instance, in an investigation focused on the interfacial contact resistivity at the junction of p-doped Si and Al probe electrodes, values were found to range between 10^{-7} and $10^{-2}\,\Omega\,cm^2$, depending on the doping concentration [111].

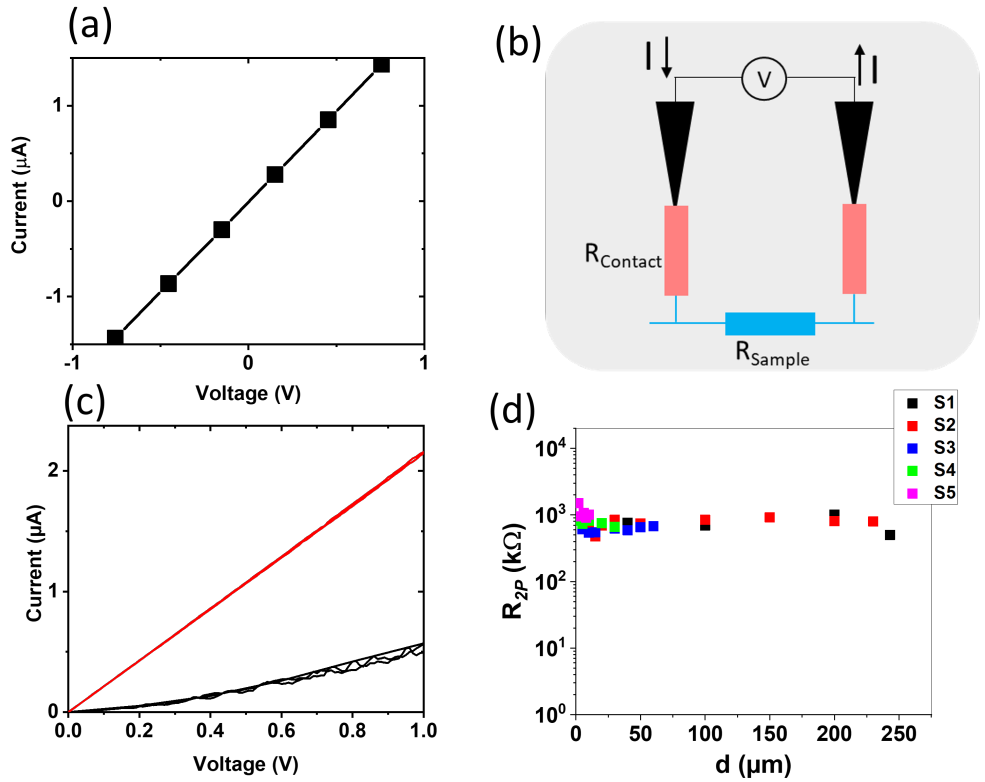

Figure 3.4: (a) I(V) characteristic measured with 2 probes separated by 10 μm. (b) Sketch of the two probe measurement showing the existence of contact resistance at each probe. (c) I(V) characteristic before (black curves) and after (red curves) voltage ramping. (d) two probe resistance measured on samples S1, S2, S3 and S5.

3.2.3.2 Non-ohmic behavior

In many cases, particularly when the probes were sharp, a non-ohmic behavior of the contact was initially observed. This was cured by a voltage ramp applied between the probe and the ground. This type of non-ohmic behavior has not been observed on the surface of UHV-cleaved samples, but only in samples cleaved before being loaded into UHV, pointing to a probable oxidation effect at the interface. This effect could be a basic heating effect improving

the surface contact or the breakdown of the thin oxide layer. However, $GaMo_4S_8$ is a Mott materials and it may also relate to a specific metal/Mott insulator interfacial change reported in the literature.

To investigate the non-ohmic behavior, we initially performed two-probe measurements. In this case, the I(V) curve in black exhibited a non-Ohmic response, as illustrated in Figure 3.4c. Intriguingly, as the applied voltage was ramped up to 15 V, we observed a change in the behavior from non-Ohmic to Ohmic, a transport regime that persisted throughout subsequent measurements (red curve). While the underlying mechanism of this change is not entirely clear, it suggests a complex interaction at the interface between the tungsten tip and our $GaMo_4S_8$ sample, possibly influenced by factors such as the work function difference and potential oxidation effects. When a low voltage is applied, it is conceivable that the energy provided to the charge carriers (electrons or holes) may not be sufficient to overcome this potential barrier at the interface. It could lead to a current that is exponentially dependent on the applied voltage, thus resulting in the observed non-Ohmic behavior. Conversely, as the voltage is increased, the additional energy provided might enable the charge carriers to overcome the barrier more readily, turning the response to a more linear Ohmic behavior. However, this interpretation is speculative, and further studies are required to definitively characterize the underlying mechanisms at play.

The observed transition from Non-Ohmic to Ohmic behavior upon increasing the applied voltage present some similarities with the characteristics reported for strongly correlated electron systems (SCES) when interfaced with a metal electrode, as detailed in the literature [114]. In these SCES-metal interfaces, a voltage-driven transition from an insulating (OFF) state to a metallic (ON) state can occur. The insulating state corresponds to a non-Ohmic I(V) behavior, associated with a high potential barrier at the interface that hinders the flow of charge carriers. However, when a threshold voltage is applied, the system transits to the metallic state, which is characterized by an Ohmic I(V) behavior indicating a lowered potential barrier facilitating the charge carriers movement across the interface. In the context of $GaMo_4S_8$, prior research indicates the existence of mid-gap states within the bandgap of the material [35]. These mid-gap states could potentially alter the energy barrier at the interface between the tungsten tip and $GaMo_4S_8$, which in turn could lower the effective barrier height. This reduction in barrier height would enable charge carriers to more readily overcome the barrier at higher applied voltages, leading to the observed change from a Non-Ohmic to an Ohmic behavior.

This distinct transition from a non-Ohmic to an Ohmic behavior, triggered by the applied voltage, prompts further investigation into the nature of the interface between the tungsten tip and $GaMo_4S_8$. Comparison with reference [114] reveals differences in the magnitude of the applied electric field, and unlike the reported results, we did not observe the reverse switch. This discrepancy suggests that what we are observing might be distinct from the reported findings. We strategically harness this voltage-induced transition to obtain reproducible Ohmic contacts by applying a high voltage (above 15 V) and overcome the initial non-linear I(V) characteristic, achieving stable resistance at the interface.

3.3 Static study of the volatile transition

Starting from a linear I(V) characteristic measured between two STM tips in the range -1V to +1 V as shown in Figure 3.4, we now study the I(V) characteristics over a larger voltage range. Thanks to the Nanoprobe capabilities, the study has been done for different electrode distances down to the micrometer scale. In the range of distance from 3 microns to 200 microns, we observed a clear volatile transition at a threshold voltage varying between 11 V and 13 V.

A typical I(V) is shown in Figure 3.5. The I(V) characteristic displays an abrupt surge in current beyond a certain threshold voltage, denoted as V^*. This sharp rise in current consis-

tently occurs at the same voltage value across repeated measurements, thereby signifying it is caused by an intrinsic property of the material. Significantly, this non-linear I(V) behavior aligns with previously reported observations in other Mott insulators of the same family, such as $GaVa_4S_8$ and $GaTa_4Se_8$ single crystals [39]. The threshold voltage, was identified as a signature of a volatile phase transition in these materials. Given the consistent behavior in $GaMo_4S_8$ and the good superimposition of the forward and backward characteristics despite a small hysterisis, these observations strongly indicate that we are likely witnessing a similar volatile phase transition.

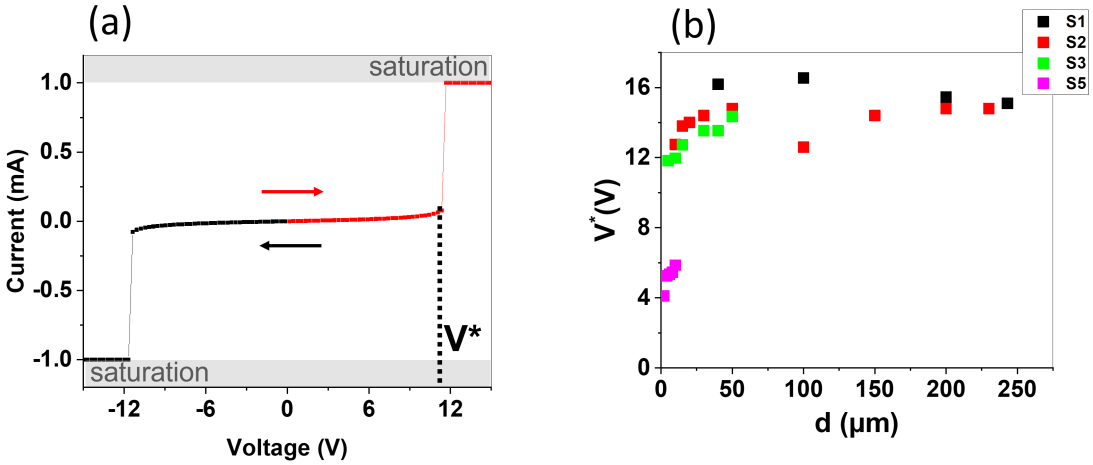

Figure 3.5: (a) I(V) characteristic taken from 0 to 15 V (red curve), and from 0 to -15 V (black curve). V^* being the threshold voltage of the transition. (b) V^* as a function of the probe distance measured on samples S1, S2, S3 and S5.

The observed threshold voltage V^*, with a mean value around 14V for samples S1 and S2, is notably higher compared to typical values found in the literature [110].

The observed phenomenon can be attributed to the contact resistances, which are significantly larger than the sample resistance. This results in a predominant potential drop at the contacts. Being aware of the importance of the contact resistance prompted us to analyze the actual voltage experienced by the sample. In order to do that, we applied the voltage divider rule. The voltage across the sample V_S^* is given by Figure 3.6:

$$V_S^* = V^* \times \frac{R_S}{R_T} \tag{3.5}$$

where R_S is the resistance of the sample and R_T is the total resistance (including the contact resistances). When $V^* = 14$ V is applied on sample S1 for example, with tips seperated by 10 μm, the resistance of the sample R_S is 3.5 kΩ (according to Figure 3.2d) much smaller than the total resistance R_T (See Figure 3.4d). As a result, only around 1% of this total voltage is experienced by the sample, which corresponds to an approximate voltage of 0.05 V. We denote this value as V_S^*, which serves as the threshold voltage for the sample.

Conventionally, the threshold voltage is understood to be related to the threshold electric field E^* and the interelectrode distance d through the equation $V_S^* = E^* \times d$. This relationship implies that V_S^* should vary with d, a behavior commonly reported in prior studies [28]. Contrary to this expectation, our experiments with $GaMo_4S_8$ reveal a surprising stability in V_S^* across a broad range of interelectrode distances, from 3 to 200 μm as shown in Figure 3.5b.

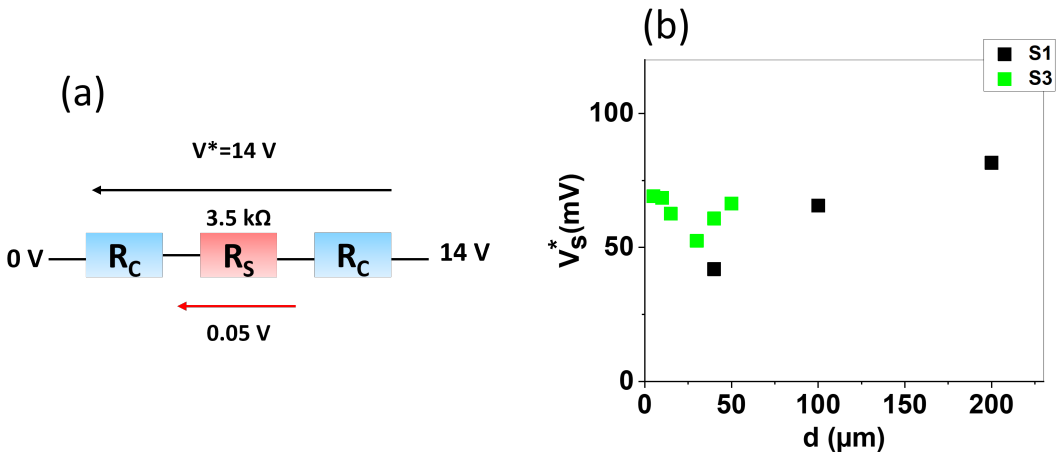

Figure 3.6: (a) Voltage divider showing 0.05 V applied on the sample whithout the contribution of the contact resistances. (b) The threshold voltage applied on the sample without the contribution of contact resistance as a function of the probe distance, for samples S1 and S3.

3.3.1 Determination of the threshold electric field for the generation of a volatile transition

In our investigation of the observed volatile phase transition within $GaMo_4S_8$, a striking feature emerged: the threshold voltage, V_S^*, appeared to be largely invariant with respect to the inter-electrode distance.

This observation was both intriguing and puzzling, defying a simple linear relationship where the electric field within the sample would be a straightforward function of V/d (voltage over distance between electrodes). To further explore and explain this unexpected behavior, a deeper understanding of the actual electric field distribution at the surface of our material was necessary. The assumption of a linear field distribution could not capture the complexity of the situation. Therefore, we utilized Finite Element Method (FEM) simulations in COMSOL Multiphysics, aiming to map out the electric field considering the unique geometry and conditions of our experimental setup. This section details the process, findings, and implications of these simulations.

As depicted in Figure 3.7a, the $GaMo_4S_8$ sample is represented as a block with a resistivity of $\rho = 38\ \Omega cm$ corresponding to the one measured in sample S2. The Ohmic contacts simulated by two circular contact points on the top surface of this block, emulate the interface between the material and the electrodes (Figure 3.7b). These simulated circular contacts were separated by a distance d.

Upon applying V_S^* to one electrode (with the other considered as ground), the electric field distribution along the x-axis was plotted (Figure 3.7c). We observe three characteristic electric field values: E_E, E_M, and E_D, corresponding to the electric fields beneath the electrodes, between the electrodes, and at the divergence point at the triple junction, respectively. Notably, E_E was found to be between 0.1 and 1 kV/cm depending on the tip separation, strengths in line with the threshold electric fields for phase transitions in several Mott insulators [35]. This similarity suggests that the transition begins beneath the electrode. In light of previous research, it is understood that the phase transition from insulator to metal begins when a particular region in the sample attains the threshold electric field. Subsequently, the transition spreads from this point, extending to more remote areas until a conductive pathway is established between the electrodes. In this context, E_E denotes the highest local electric field that the sample experiences when a voltage is applied.

E_D represents a divergence in the electric field at the so-called 'triple point,' which is the in-

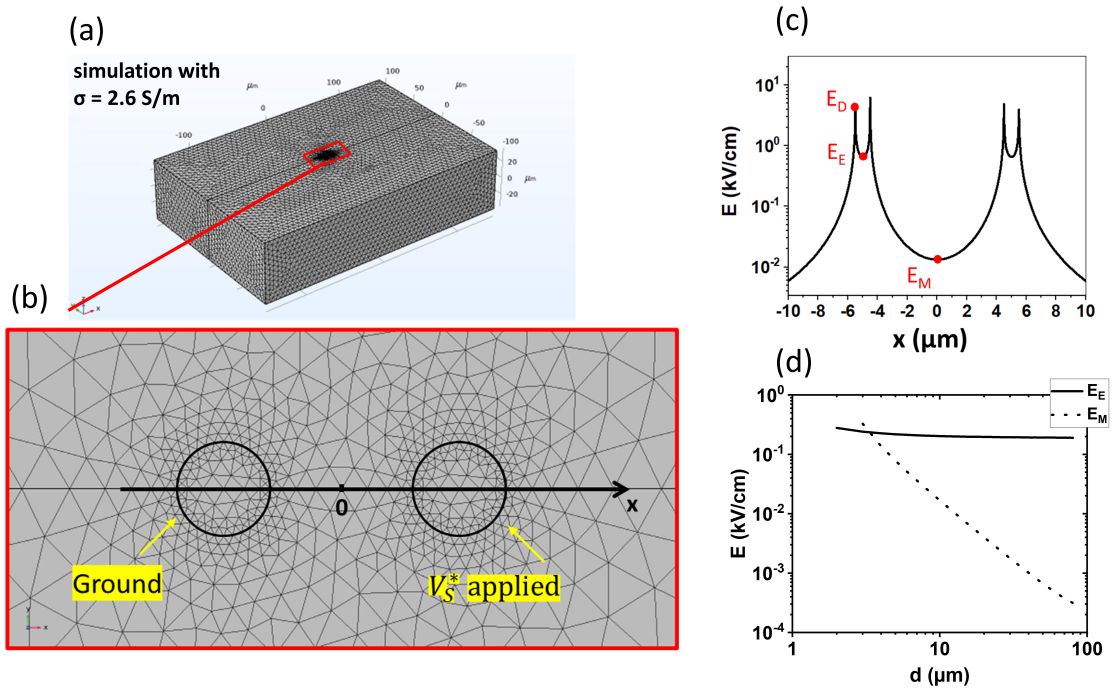

Figure 3.7: a) Representation of the material as a block with resistivity $\rho = 38\Omega cm$. (b) Zoom of two simulated circular contact points on the top surface of the block, separated by a distance $d = 10, \mu$m, reflecting the interface between the material and the electrodes. (c) Plot of the electric field distribution along the x-axis upon applying voltage V_S^* to one electrode, with the other considered as ground. (d) Plot of the electric field distribution E_E and E_M as a function of the inter-electrode distance d [115]

tersection of the sample, electrode, and vacuum. One might consider attributing the threshold value E^* to the electric field identified at this divergence point, E_D. Nevertheless, we argue that E_D may not be the pertinent electric field for this analysis and could be a mathematical artefact in the simulations. This conclusion is mainly drawn from our experimental observations that showcase a reproducible voltage threshold, irrespective of the probe-sample contact. In contrast, E_D would presumably be highly sensitive to changes in the contact geometry, specifically showing minimal values for obtuse angle contacts [116]. We therefore ascribe the threshold electric field to E_E, which is the maximum electric field point when divergences are excluded.

An intriguing observation emerges when considering E_E and E_M as functions of the inter-electrode distance. As depicted in Figure 3.7d, E_E appears constant as a function of the probe distance and consistently registers higher values compared to E_M in the regime $d > 3\mu m$. However, as the distance between the electrodes diminishes, a crossover occurs wherein E_M surpasses E_E. This crossover is observed when the inter-electrode distance aligns with the size of the electrodes themselves, suggesting the influence of electrode geometry and spacing on the electric field distribution within our sample. E_M shows a decrease as the probe distance increases, echoing the dependence observed in a parallel capacitor where the electric field is inversely proportional to the distance between the electrodes [117]. When the tip size is reduced, E_E shows an increase as a function of $\frac{1}{(2r)^2}$. This trend mirrors the electric field created by a point charge.

After our qualitative analysis of the electric field distribution, we turn our attention to the threshold electric field determined by our measurements. When an external voltage of 14 V is applied, the effective voltage experienced by the material is reduced to 50 mV due to contact resistances. In our COMSOL simulations, we incorporate the aforementioned effective voltage of 50 mV as the applied voltage on the material, resulting in $E_E = 0.2$ kV/cm. This E_M

remains consistent across varying electrode distances, underscoring that the threshold field for the observed transition is independent of both electrode geometry and distance. Remarkably, this threshold field aligns closely with values found in the literature for the same material. This correspondence further suggests that our observed threshold is an intrinsic property of the material. Such an intrinsic threshold electric field has been detailed in a temperature-dependent study, denoted as $E_{th}(T)$ in prior work [35], for temperatures ranging from 70 to 200 K. Extrapolating from this study to a temperature of 300 K, we found the threshold electric field to consistently lie between 0.1 and 1 kV/cm. This range aligns notably with our findings.

3.4 Temporal characteristics of pulse-induced phase transition

While our exploration into the threshold voltage and electric field has provided substantial insights into the phase transition characteristics of $GaMo_4S_8$, it is essential to further enrich this understanding with the temporal aspects of this transition. Specifically, we are interested in the phase transition response and progression under the influence of electric pulses. To implement this, our experimental setup underwent a notable modification. Instead of the regular Keithley device used for I-V measurements, a pulse generator and a voltage amplifier were incorporated into the nanoprobe setup, as seen in Figure 3.8a. The connection established between the pulse generator and the nanoprobe tips allows to precisely modulate the pulse attributes such as its duration, amplitude, and shape, which are likely to influence the phase transition dynamics.

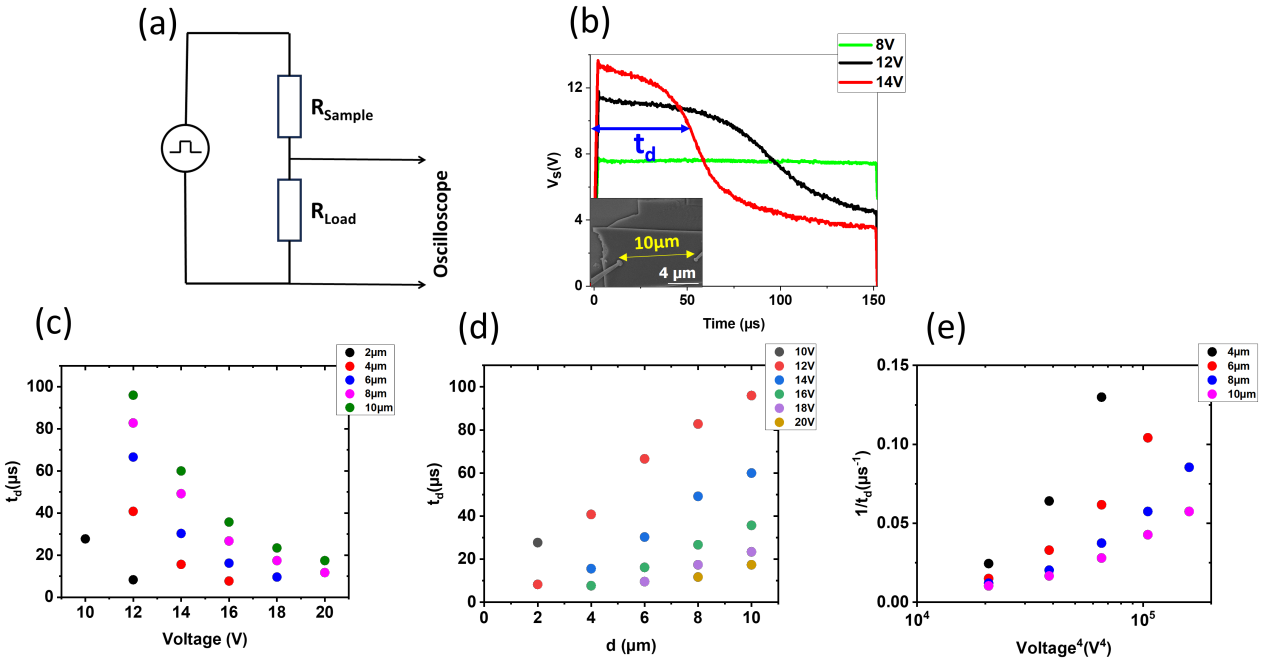

Figure 3.8: (a) Schematic of the setup incorporating a pulse generator and voltage amplifier, connected via a load resistor (R_L). (b) Temporal responses of the system for 3 distinct pulse amplitudes, 8 V (green curve), 12 V (black curve) and 14 V (red curve), the two probes were separated by 10µm (See SEM image in inset). (c) Graph showcasing the decreasing delay time (t_d) with the higher amplitude of the pulse voltage. (d) Plot of the relationship between t_d and the inter-tip distance d for different applied voltages for different tip separations. (d) A plot of the inverse relationship between the delay time, t_d, and V^4, across varying probe distances ranging from 4µm to 10µm.

To prevent potential damage to the nanoprobe electronics from any sudden drop in the

sample resistance, we introduced a load resistor (R_L) in series with the sample. This ensured that the current would flow through R_L in the event of an abrupt resistance switch in the sample. We continuously monitored the voltage drop across our sample to capture its real-time response to the applied electric pulses.

All instruments involved in the experimental setup were controlled via a LabView interface, developed by Yevheniia Chernukha, a postdoc in our group. This program not only streamlined the operation of the equipment but also facilitated real-time data recording and analysis.

Upon positioning the nanoprobe tips on the $GaMo_4S_8$ sample at a distance of 10 μm, we initiated the application of electric pulses with a square shape and a duration of 100 μs. As depicted in Figure 3.8b, the temporal responses for three distinct pulse amplitudes are presented. When a low voltage of 8 V is applied, the system demonstrates stability, as indicated by the green trace that remains relatively unchanged throughout the pulse duration. However, a different scenario emerges as we amplify the pulse to 12 V. In this case, we observe an intriguing phenomenon: the voltage first rises and then after a particular duration, the voltage begins to markedly drop. As introduced in the first chapter, this observation signals an interesting event within the system - the onset of a phase transition. This moment carries significant importance and is denoted as the delay time, or t_d. It is defined as the point at which a distinct change in the slope of the voltage-time curve is observed. This inflection point, identified through the derivative of the voltage with respect to time. It essentially encapsulates the temporal characteristics of the phase transition under the influence of an electric pulse. It is crucial to note that the system returns to the initial resistance state at the end of the pulse, emphasizing the volatile nature of this transition. With this primary observation, we now focus on investigating the influence of voltage variations on the delay time, t_d.

As the phase transition dynamics is further probed by increasing the applied voltage, a noteworthy pattern was encountered. By increasing the pulse amplitude from 12 V to 14 V in Figure 3.8b, we observe a noticeable decrease in the delay time t_d. This decrease, in relation to the increase in voltage amplitude, is clearly illustrated in the Figure 3.8c, whatever the electrode separation was. Importantly, these measurements were carried out on two different samples, with thicknesses of 40µm and 5µm, and we observed the same trend in both cases.

The decrease of t_d with the voltage increase has been already reported, as discussed in chapter 1. Previous studies on $GaMo_4S_8$ where two electrodes are glued onto the sample, have observed a similar dependence of t_d on the electric field. It was shown for a fixed distance that $E_{th}^4 \propto 1/t_d$, suggesting that the resistive transition appears when the electronic system reaches the critical plasma density [35]. In our case, as shown in Figure 3.8e, $1/t_d$ seems to have an approximately linear relationship with V^4 across inter-electrode distances ranging from 2 to 10 μm. This characteristic behavior extends beyond $GaMo_4S_8$, as it has also been reported in other AM_4X_8 compounds like $GaTa_4Se_8$ and $GaVa_4S_8$ [28].These consistent findings across different materials, configurations, and sample thicknesses confirm a common mechanism underlying these phase transitions.

3.4.1 Impact of the interle-electrode distance on the dynamics of the transition

Thanks to the precision of the nanoprobe setup to adjust the inter-electrode distance, the impact of the distance on the resistive switching time was explored, a topic still under debate. For instance, Stoliar and Tesler studies have shown that the volatile transition is well described by an avalanche phenomenon where t_d is dictated by the time needed to achieve a certain critical metallic site density [118]. This duration largely exceeds the subsequent delay necessary for the formation of the metallic filament. However, the dependence of t_d with the sample size is not explicit in these models and the nature of t_d as an intensive or extensive parameter is

yet to be ascertained. The nature of t_d as an intensive or extensive parameter is yet to be ascertained. However, its importance is undeniable, especially in the context of ReRAM and neuromorphic components [43]. The delay time directly impacts the energy consumption of a switch operation, emphasizing the need for understanding its behavior for future nanometric devices.

To understand the dynamics of resistive switching, we conducted a series of measurements, modulating the inter-electrode distances while systematically adjusting the voltage amplitudes at each position. In the general case, t_d depends also on the voltage through V/V^*: t_d becomes infinite for voltage close to the threshold. In this study, we take advantage of the specific Nanoprobe electrodes configuration that allow for a nearly constant threshold voltage with electrode distance. The relationship between t_d and the inter-electrode distance d for sample S5 is depicted in Figure 3.8d. Intriguingly, our data delineates a distinct pattern: for a specific voltage, t_d increases as the inter-electrode distance expands. This indicates a faster transition as the distance diminishes. The observed t_d spans between a value below few μs and 100 μs over a distance range from 2 to 10 μm. This relationship appears linear, and extrapolation suggests that for distances being below 2 μm, the transition time could fall below the 8 μs minimum measured in our experiments. However, given the inherent time contribution of our electronics, approximately 5 μs, we may not detect t_d values below this threshold.

This observation underscores a pivotal connection between the spatial characteristics and the delay time in the phase transition triggered by electric pulses in $GaMo_4S_8$. Notably, the behavior of t_d strongly hints at its extensive nature. This extensivity could have profound implications for understanding the spatial scaling behavior in such systems, potentially guiding the optimization of device structures and operational parameters in future Mott insulator-based applications.

3.4.2 Characteristic energy of the transition

Building upon these observations, we further delve into the phase transition mechanism, echoing the interpretation discussed in [35]. The electronic temperature rises when an electric field is applied and its effect is balanced by a dissipation through the lattice up to a certain threshold electric field (See Figure 3.9a). Upon reaching this threshold, the equilibrium between heating and cooling powers is disrupted, propelling the system into a non-equilibrium state, thereby triggering the transition after a delay time, t_d.

To quantify the energy associated with the phase transition across varying inter-electrode distances, we adopted a methodological approach rooted in integrating the product of current, I, and voltage V seen by the sample, over a specific duration. This integral spans from the initial application of the voltage to a distinct transition delay time, t_d:

$$W_{transition} = \int_0^{t_d} I(t) \cdot V(t)\, dt$$

The determination of t_d was crucial. It was identified at the juncture where the derivative of the voltage with respect to time was most negative, signifying a sharp decrease in voltage. The data underwent preliminary processing, where any potential noise was minimized, ensuring the accuracy of the t_d determination.

With this definition in place, our results highlighted a significant relationship between the energy and the inter-electrode distance, revealing an increase in energy as d increased (Figure 3.9b), provides an intriguing parallel to our previous observation of an increase in t_d with the inter-tip distance. This simultaneous increase in both energy and t_d as a function of distance may suggest a shared dependence on the spatial characteristics of the system. Specifically, the

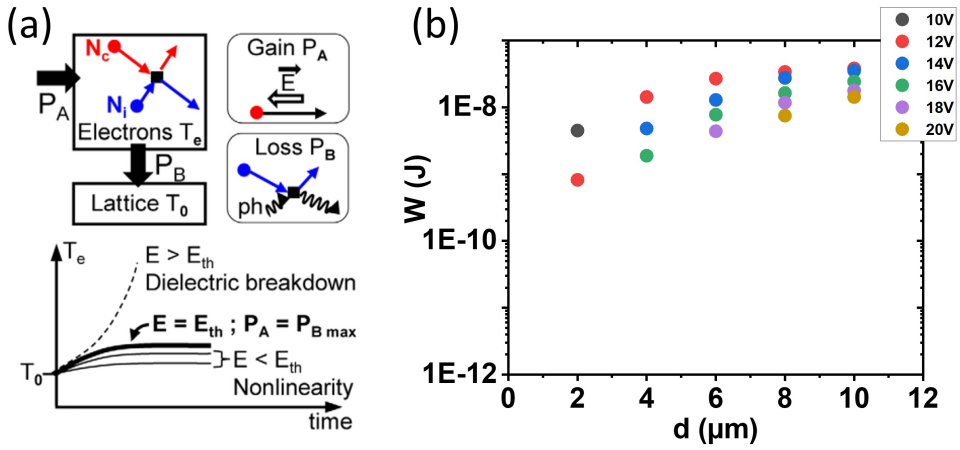

Figure 3.9: (a) Illustration of the thermal dynamics within the electronic system of a Mott insulator. The electron temperature T_e is shown to be distinct from the lattice temperature T_0, with P_A and P_B representing the respective heating and cooling powers. The plot displays the progression of the electronic temperature across various electric field values. [35] (b) The dependency between the energy W needed for phase transition and the inter-electrode distance d for applied voltages ranging from 10 to 20V.

increase in energy required for the transition might be correlated with the observed increase in delay time, t_d, as the distance between the electrodes is expanded.

This correlation between t_d and energy as a function of d emphasizes the complexity of the phase transition dynamics and points to an intricate interplay between spatial parameters, time delays, and energy requirements. The observation that both energy and t_d exhibit a dependence on distance adds an additional layer of insight into the underlying mechanisms of these phase transitions in $GaMo_4S_8$. It may point towards the evidence of a latent heat necessary for the transition, that depends on the sample active volume.

Furthermore, the observed decrease in both t_d and $W_{transition}$ with d is particularly promising for applications, suggesting enhanced device performance at reduced electrode distances. This trend indicates a potential avenue for achieving faster switching times while minimizing energy consumption, a crucial consideration for future device optimizations and efficient phase transitions in practical scenarios.

3.4.3 LIF function in cleaved $GaMo_4S_8$

Our investigations with the UHV cleaved sample, S5, unveiled the presence of a Leaky Integrate-and-Fire (LIF) function at an inter-electrode distance of 5 µm, as illustrated in Figure 3.10a which depicts a SEM image of the electrode separated by a distance of 5 µm. Notably, upon applying a series of 10 V pulses, the transition is observed to occur at the third pulse, as shown in Figure 3.10b. Historically, LIF properties in Mott insulators, including $GaMo_4S_8$, have been reported at temperatures as low as 74 K [36]. Other Mott insulators have shown this property at temperatures below 164 K. This makes our observation of the LIF function at room temperature in $GaMo_4S_8$ particularly significant, suggesting an advantage for real-world applications. In recent years, there has been a notable study proposing a single-component neuron operating at room temperature [118]. The discovery of the LIF function in our UHV cleaved sample, especially under these conditions, offers a promising avenue for the development of Mott insulator-based neuromorphic devices.

These are preliminary finding, which requires more detailed study, underscores the possi-

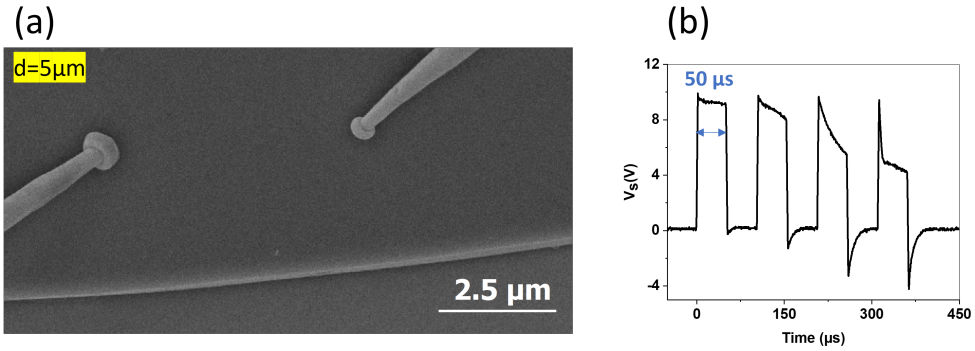

Figure 3.10: (a) SEM image showing two probes with an inter-electrode distance of 5 µm. (b) Series of applied pulses of 10 V, where the volatile transition appears at the third one.

bility of realizing the LIF function at room temperature in $GaMo_4S_8$.

3.5 Investigating the irreversible resistive switching at reduced inter-electrode distances

The subsequent section will shift the focus to transitions at reduced inter-electrode distances. The motivation to explore reduced inter-electrode distances arose from a desire to investigate the possible presence of the Leaky Integrate-and-Fire (LIF) function at the nanoscale. This neural function, known to exist at macroscopic scales, was reported in $GaMo_4S_8$ along with other Mott insulator compounds such as the oxide $(V_{0.89}Cr_{0.11})_2O_3$ and [Au(R-thiazdt)$_2$] [118].

To achieve this, the probes were carefully moved to an inter-electrode distance of 2µm, as shown in the SEM image of Figure 3.11a. Electric pulses were systematically applied, with voltage amplitudes gradually increased, as depicted in Figure 3.11b. The transition began to manifest at 10V after a certain delay time t_d. After the pulse, the resistance returned to its value measured before the pulse, suggesting that it is a volatile transition.

Upon increasing the amplitude to 12 V, a reduction in the delay time t_d was observed, consistent with previous findings. Unlike the 10V pulse, after this 12 V pulse, the resistance of the sample did not return to its initial value but rather remained in a low resistance state, suggesting that it is not a volatile transition as observed before. Additionally, the SEM image in Figure 3.11c, taken after the 12 V pulse, reveals the formation of a filament between the two probes. This alteration, contrasting sharply with the lack of any visible modification of $GaMo_4S_8$ at larger inter-electrode distances, signified a notable departure from the previous experiments.

The emergence of a filament between the two probes naturally evokes comparisons with the non-volatile transition previously reported in Mott insulators such as $GaTa_4Se_8$ [29, 119, 120] and GaV_4S_8 [121]. The resemblance to this well-documented phenomenon prompted us to consider whether the observed behavior might be a manifestation of a non-volatile transition in $GaMo_4S_8$. However, key distinctions arose in our case. The first and more important one is the magnitude of the electric field at which the change is observed: whereas the non-volatile Mott transition typically arises at strong electric field, corresponding typically to more than 5 times the threshold voltage, here the change appears very close to the threshold voltage.

A noteworthy observation is the distinct morphology of these filaments. Their regularity contrasts sharply with the amorphous structures that might arise from heat-induced amorphization. Further emphasizing this distinction, four-point resistance measurements shows a significant drop in resistance by a factor of 50. Such a pronounced decrease suggests a mech-

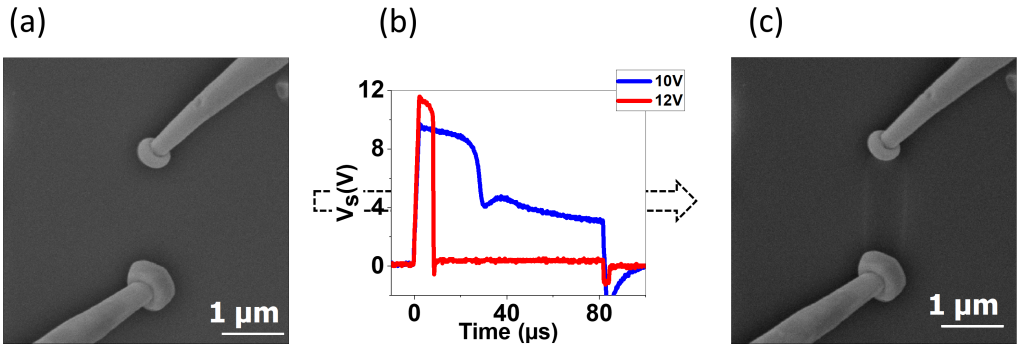

Figure 3.11: (a) SEM image, showing two probes with an inter-electrode distance of 2 μm before the application of electric pulses. (b) Response of the sample to electric pulses with amplitudes of 10 and 12 V. (c) SEM image acquired after the applying of 12 V pulse showing the creation of a distinct path between the two probes.

anism not simply attributable to amorphization by Joule heating. An alternative hypothesis, worth exploring, could be the formation of a molybdenum filament through ionic migration.

While for non-volatile transitions, the initial resistance state can be recovered through electric pulses, as mentioned in previous studies [38], our findings diverged from this. Extended electric pulse application, reaching up to 8V and durations up to few milliseconds, was tested. Also, with the reversed non-volatile Mott transition often attributed to Joule heating, we attempted controlled heating of the entire sample, raising its temperature to 300°C overnight (for approximately 16 hours). Yet, the filament persisted, hinting at an underlying mechanism different from the Mott non-volatile transition.

Importantly, this observation is not isolated. The phenomenon reproducibility was underscored by the successful inscription of "IEMN" on the sample surface as shown in Figure 3.12a.

To further investigate the nature of the observed filament and its distinctive persistence, we set out an in-depth examination using various characterization techniques:

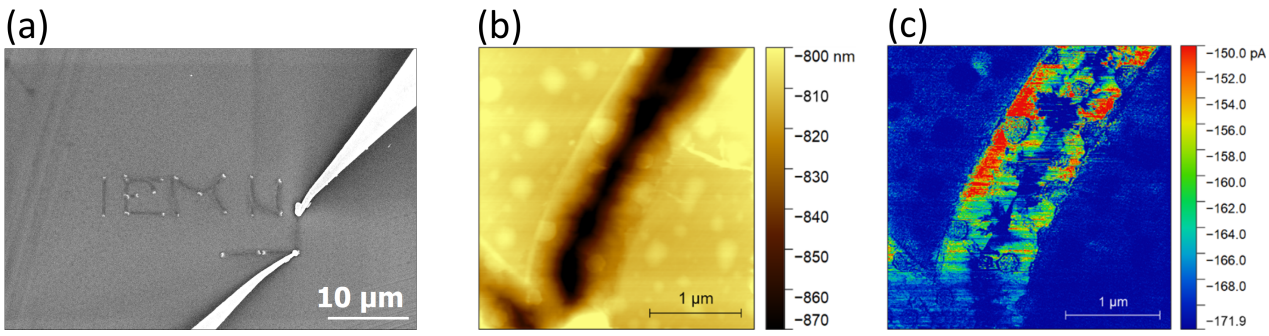

Figure 3.12: (a) A SEM image showcasing the 'IEMN' pattern written on the sample. (b) A detailed AFM image focused on a singular filament. (c) Conductance mapping of the filament in (b).

- **Conductive Atomic Force Microscopy (C-AFM)**: C-AFM was employed to delve into the topographical and conductive properties of the filament once the sample was withdrawn from the UHV environment. Figure 3.12b offers a detailed examination of a singular filament. The filament is hollowed out to a depth of about 40nm. This characteristic is in contrast to Mott insulators such as $GaTa_4Se_8$, where filaments protrude about 20nm above the surface [30]. In $GaTa_4Se_8$, such a protrusion is characteristic of

the non-volatile transition. The absence of this feature in our observations might indicate a deviation from the typical non-volatile transition.

Further, the filament conductivity mapping, as demonstrated in Figure 3.12c, unveils pronounced conductivity, notably surpassing that of the surrounding pristine regions. The edges of the filament, in particular, exhibit heightened conductivity. This phenomenon of heightened conductivity at the filament edges could be attributed to a variety of factors. One possibility is the inherent contact dynamics between the filament unique topography and the C-AFM tip, which might result in a larger contact surface area and, consequently, a greater current. Alternatively, the edges of the filament themselves could inherently possess higher conductivity.

The C-AFM experiments detailed in this section were performed by our intern, Tushar CHAKRABARTY.

- **Energy-Dispersive X-ray Spectroscopy (EDX):**

  One of the key aspects of understanding the nature of the conductive filament in $GaMo_4S_8$ revolves around its chemical composition. To this end, EDX spectroscopy was employed, providing a thorough elemental analysis of the filament compared to the pristine regions of the sample. The experiments where performed by David Troadec at IEMN. Figure 3.13 showcases the spectra for both regions.

  Figure 3.13a is a SEM image showing the conductive filament. We distinguish two main areas: position 18 is located in the prestine area of $GaMo_4S_8$, and position 20 is in the middle of the filament. EDX spectra are performed at these two positions, and shown respectively in Figures 3.13b and c. Both spectra showcase the presence of Ga, Mo, S and C elements. When the filament is created, the Mo content exhibits a slight increase, meanwhile, Ga registers a significant decline, its weight ratio goes from 8.85% in the prestine area, to 3.84% in the transited are.

  The observed increase in Mo concentration within the filament region warrants further investigation. One plausible factor driving this change is the influence of the applied electric field during filament formation. This field may promote a localized migration or rearrangement of Mo atoms, potentially leading to their denser aggregation within the filament area. This notion aligns with our C-AFM observations in Figure 3.12c, which identified specific regions within the filament showcasing heightened conductivity, potentially indicating areas with a denser concentration of Mo.

  Additionally, the experimental conditions might have facilitated certain chemical transformations, resulting in a decomposition or restructuring of the $GaMo_4S_8$ compound. Such changes could introduce disparities in the relative abundances of Ga and Mo within the filament.

- **RAMAN spectroscopy:**

  To comprehend the structural changes accompanying the filament formation, Raman spectroscopy was employed. The experiments where performed by Dominique Vignaud at IEMN. Figure 3.14a displays the Raman spectrum of the pristine $GaMo_4S_8$ sample, where a myriad of peaks are discernible, ranging from 100 to 500 cm^{-1}. The peak with the most pronounced intensity is observed at 450 cm^{-1}. Although the precise origins of these peaks in $GaMo_4S_8$ remain elusive due to the lack of reference spectra, the peaks can be associated with various vibrational modes inherent to the material.

  Switching to the filament Raman spectra in Figure 3.14b, a stark contrast in the spectral landscape becomes apparent. While the peak at 450 cm^{-1} persists, its intensity is

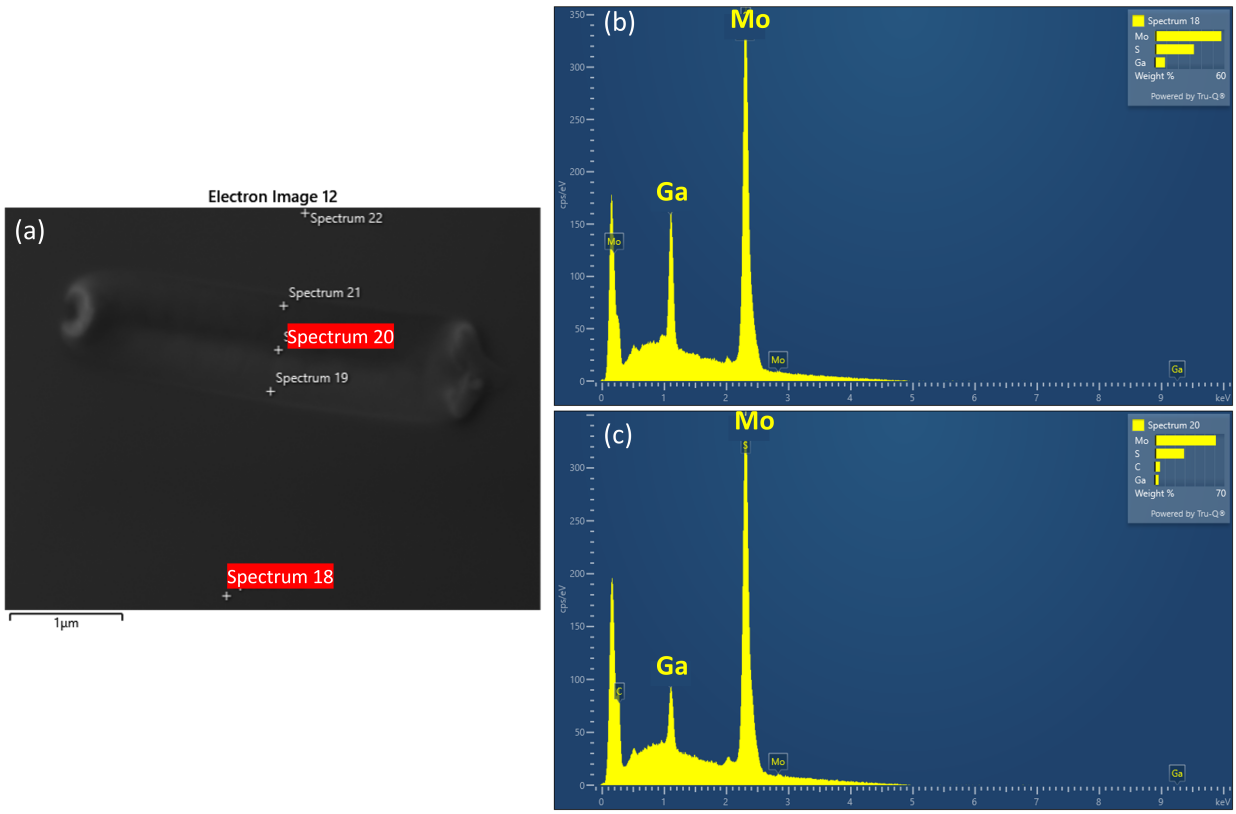

Figure 3.13: (a) SEM image showing the conductive filament. Spectrum 18 and 20 refer to the prestine area and the created filament respectively. (b) and (c) EDX spectra taken at position 18 and 20 respectively.

diminished compared to that in the pristine sample. Furthermore, two new pronounced peaks emerge around 381 cm^{-1} and 407 cm^{-1}. These peaks, distinct from the pristine sample, align with well-documented vibrational modes. In particular, they closely match the characteristic vibrational modes of MoS_2: the in-plane E_{2g} mode and the out-of-plane A_{1g} mode. Literature data on MoS_2 highlights that bulk MoS_2 typically exhibits these prominent peaks, and as MoS_2 reduces to a single layer, the E_{2g} mode upshifts while the A_{1g} mode downshifts. The observed difference of approximately 26 cm^{-1} between our observed modes suggests a potentially multi-layered MoS_2 structure within the filament [122, 123].

The gathered findings from this comprehensive study gravitate towards a compelling conclusion: at inter-electrode distances below 3 microns, the electric pulse appears to instigate a pronounced chemical transformation. This transformation seemingly morphs $GaMo_4S_8$ into a crystalline MoS_2 filament. Morphologically, the filament showcases a unique structure and topography. Its conductivity, rather than being uniformly dispersed, is spatially varied with certain regions displaying heightened conductivity. The increase in Mo concentration within the filament further indicates potential atomic rearrangements or chemical shifts. Beyond this, the signatures consistent with MoS_2 provide evidence for underlying structural changes within the filament.

Furthering our insights into the practical implications of the MoS_2 filament formation, an intriguing observation emerged regarding its electrical properties. It was noted that the contact resistance experienced a substantial reduction on the MoS_2 filament. This was made evident when contrasting 2-point and 4-point resistance measurements performed on the filament. In a more direct testament to the filament utility, current-voltage ($I(V)$) measurements conducted

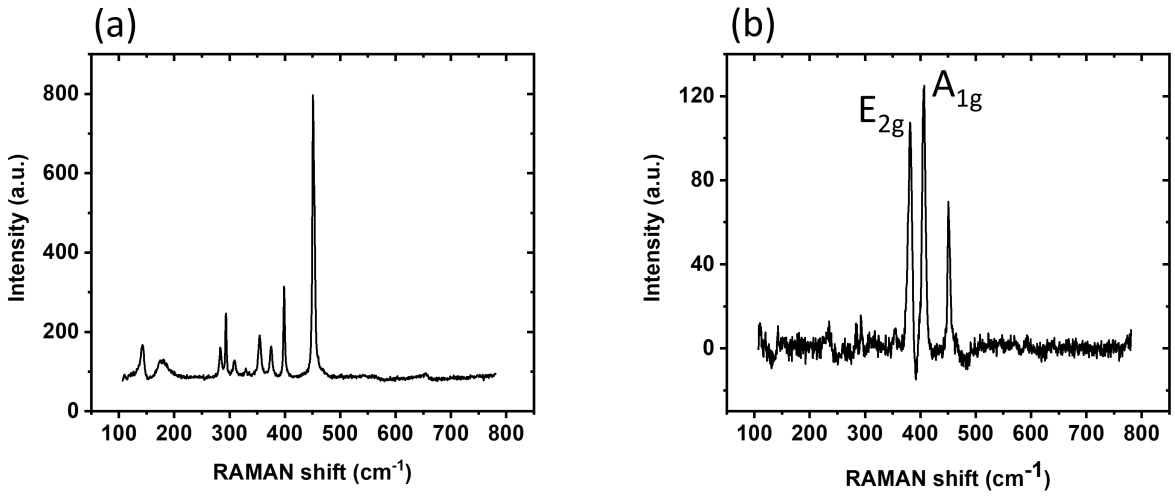

Figure 3.14: Raman spectrum of the $GaMo_4S_8$ sample on (a) the prestine area and (b) the created filament.

with one of the electrodes positioned on the MoS_2 filament revealed a marked drop in the threshold voltage, settling at a mere 7 V instead of 14 V. This reduction is due to the strong decrease of the contact resistance in the filament, of the order of few tens of kΩ, to be compared to 0.5 MΩ in the pristine material. Such a reduction holds significant promise for device development, especially in endeavors aimed at curtailing power consumption. Drawing parallels with contemporary semiconductor technology, this effect mirrors the strategic doping in transistors, a move made to establish ohmic contacts. In a similar vein, optimizing the interface in our context might pave the way for achieving reductions in threshold voltages, ushering in a new paradigm of energy-efficient devices.

3.6 Conclusion

In this chapter, we focused on the electric field-induced transitions in $GaMo_4S_8$. The use of STM tip electrodes was a pivotal aspect of our study, introducing a higher contact resistance compared to the macroscopic electrodes. This difference significantly influenced our measurements of the threshold electric field. After accounting for the increased contact resistance, we found that the electric field required for transitions aligns with those observed in studies using larger, flatter electrodes, validating our experimental approach and the bulk intrinsic character of the threshold electric field above which the electric Mott transition appears.

Moreover, our findings showed an intriguing relationship between the electrode distance and the transition dynamics in $GaMo_4S_8$. While the threshold electric field for initiating the phase transition remained constant across different electrode distances, the delay time of the transition increased as the distance between electrodes grew. This suggests a distinct spatial component in the transition process, where the delay time of the phase change through the material becomes a key factor with increasing distance. This observation adds a crucial dimension to our understanding of the material behavior under external stimuli and has important implications for practical applications.

Additionally, our experiments revealed novel behaviors under higher electric fields, such as the transition from $GaMo_4S_8$ to MoS_2.

In summary, this chapter has provided significant insights into the behavior of $GaMo_4S_8$ under electric fields. We have demonstrated the critical role of experimental methodology, particularly the impact of electrode geometry and inter-electrode distance on observed phenomena.

Our findings contribute to a more nuanced comprehension of phase transitions in Mott insulators and underscore the complex interplay between experimental configurations and material behaviors in condensed matter physics.

Chapter 4

Structural and electronic properties of single layer $TaSe_2$ on GaP(111)B

4.1 Introduction

Two-dimensional (2D) Mott insulators are strongly correlated systems that have been in focus of extensive research in recent years. Mott insulator states arise when the Coulomb interaction (U) exceeds the bandwidth (W) in half-filled band systems. This results in the splitting of the density of states around the Fermi level into two bands: the upper Hubbard band (UHB) and the lower Hubbard band (LHB). Consequently, a Mott insulator gap is formed. Intriguingly, these materials possess high correlation energy, making them excellent candidates for investigating exotic quantum phenomena such as high-temperature superconductivity [124] and quantum spin liquid [125].

Tantalum diselenide ($TaSe_2$), a transition metal dichalcogenide (TMD), exhibits fascinating electronic and optical properties. This material exists in three distinct phases shown in Figure 4.1: 1T, 2H, and 3R, each differing in crystal structure and electronic properties. The 1T phase displays trigonal coordination, the 2H phase has a hexagonal layered structure, and the 3R phase presents a rhombohedral structure. The distinctions between these phases lie in the stacking arrangement of the layers of transition metal and chalcogenide atoms as seen in Figure 4.1a. The stacking order significantly impacts the material electronic properties, with each phase exhibiting distinct behaviors due to their unique structural arrangements.

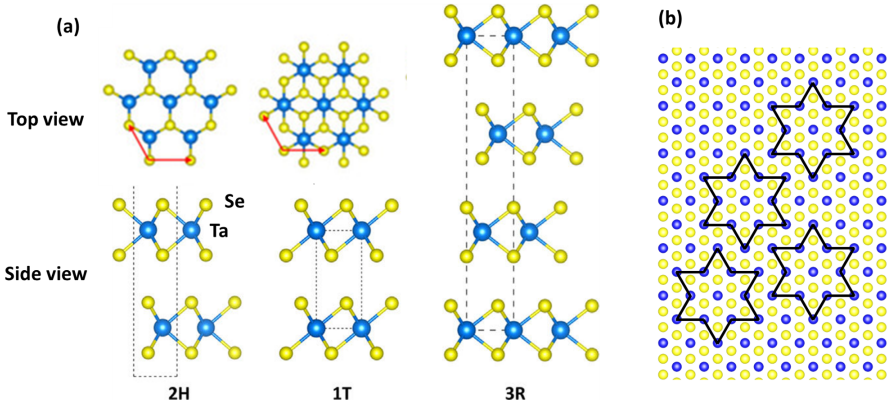

Figure 4.1: (a) Top and side view of the structural representation of 1T, 2H and 3R transition metal dichalcogenide polytypes. The numbers indicate the number of layers in the unit cell and the letters stand for trigonal, hexagonal and rhombohedral, respectively. The unit cells are indicated by red arrows. (b) Top view sketch of single-layer 1T-$TaSe_2$. A clusters of 13 Ta atoms are outlined in star-of-David (SOD) CDW. Adapted from [126]

The 1T-$TaSe_2$ polytype, a Mott insulator, displays a notable charge density wave (CDW) property. This material undergoes a first-order phase transition below 473 K [127], forming a commensurate charge density wave (CCDW). Each layer reconstructs into a $\sqrt{13}\times\sqrt{13}$ superlattice, shaped like a Star of David (SOD). Each SOD consists of 13 Ta atoms bonded into a cluster as seen in Figure 4.1b, with the central atom retaining a single unpaired 5d electron. It leads to a half-filled band. But, due to band folding associated with the formation of a superlattice caused by the CDW, the width of the half-filled band shrinks to the scale of U, making the layer insulating. However, because of the interaction between the stacked layers in the 1T-polytype, 1T-$TaSe_2$, in its bulk form, displays a metallic behavior [72] [73]. When its dimensionality is reduced, a transition from metallic to Mott insulator is observed at a critical thickness of a few layers, the minimum number of layers being still debated, three in [74], seven in [75], for example.

The rich physics of the Mott insulator state continues to intrigue researchers, stimulating ongoing efforts to synthesize, grow, or exfoliate high-purity samples (ones with the least amount of impurities or structural defects) and characterize them using the most sophisticated methods available. Among these methods, chemical vapor deposition (CVD) and molecular beam epitaxy (MBE) on substrates like graphene or highly oriented pyrolytic graphite (HOPG) stand out for their ability to produce thin films of materials in a controlled manner, minimizing the incorporation of impurities and structural irregularities.

In this chapter we focus on 1T-$TaSe_2$ single layer grown on graphene and GaP(111)B substrates using MBE. By performing thorough characterization of the epilayers, mostly with STM and STS, we aim to elucidate the structural and electronic properties of this single layer.

4.2 Synthesis of a 1T-$TaSe_2$ epilayer

$TaSe_2$ monolayer was grown using MBE on two different substrates: epitaxial graphene and n-type gallium phosphide (GaP) doped with sulfur (S) atoms, with a doping concentration of 2×10^{18} cm^{-3}. The (111)B orientation of GaP was specifically chosen for its symmetry which matches with the one of $TaSe_2$. The epitaxial graphene was initially grown on copper and subsequently transferred onto a silicon substrate that was coated with a 180 nm thick layer of SiO_2. The growth process took place inside a MBE chamber under a pressure of 10^{-10} Torr. Prior to the deposition of Se and Ta elements, both substrates were subjected to a heating phase: the graphene was heated up to 600°C, and GaP was heated up to 525°C. In the case of GaP, a passivation process was performed to replace phosphorus adatoms with selenium, creating a Se passivation layer on top of the GaP substrate. The passivation of the dangling bonds at the GaP(111)B surface favors the crystallization of an adlayer without the formation of chemical bonds with the substrate. On top of this Se passivation layer, we grew a $TaSe_2$ monolayer, which consists of a transition metal atomic plane sandwiched between two chalcogen layers. This specific stacking was confirmed by Transmission Electron Microscopy (TEM) measurements on a similar TMD material, $WeSe_2$ [81]. The growth process was monitored in real time using Reflection High-Energy Electron Diffraction (RHEED), as depicted in Figure 4.2.

Figure 4.2a shows the RHEED pattern of the clean GaP substrate. After the selenium passivation of the GaP substrate, a noticeable change in the RHEED pattern was observed, as depicted in Figure 4.2b. The deposition of $TaSe_2$ on the passivated substrate resulted in a further change in the RHEED pattern.

Following the deposition, an annealing process was carried out, after which the RHEED pattern was recorded again, as shown in Figure 4.2d. This step served to further confirm the growth and crystalline structure of the new layer on the GaP substrate. The different temperatures used in the process are presented in Table 4.1.

The consistent transformation in the RHEED patterns at each step of the process provides

	Graphene	GaP
Growth	600°C	600°C
Annealing	640°C	700°C
Decapping	260°C	270°C

Table 4.1: Temperatures used for each step of the sample preparation, the growth, the annealing and the decapping to remove the protective Se layer.

strong evidence of the successful deposition of a new layer on the GaP substrate. While RHEED allows us to infer the successful deposition of a new layer and gain some understanding of its structure, it does not provide direct information about the chemical composition of the deposited layer. Therefore, further characterizations were performed.

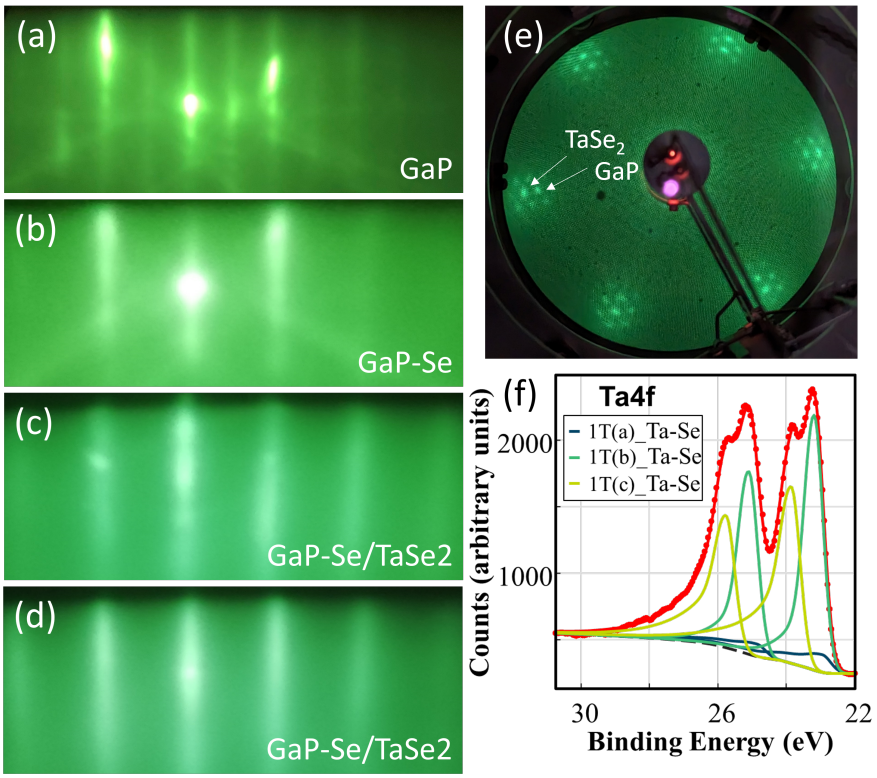

Figure 4.2: RHEED patterns along the [111] azimuth for (a) the clean GaP(111)B surface, (b) the GaP(111)B passivated with Se, (c) the $TaSe_2$/GaP heterostructure and (d) after annealing. (e) LEED pattern of the $TaSe_2$/GaP heterostructure with two highlighted diffraction spots related to the GaP and $TaSe_2$ lattices respectively. (f) XPS diffraction peaks of the Ta 4f electrons measured with a photon energy of 1486.7 eV.

Low energy electron diffraction (LEED) measurements were performed at room temperature, using an electron energy of 50 eV, to further confirm the structure and orientation of the grown $TaSe_2$. The LEED pattern, depicted in Figure 4.2e, corroborates the conclusions drawn from the RHEED analysis. We observe well-aligned diffraction spots from both the GaP(111)B substrate and $TaSe_2$, signifying the growth of a thin epilayer in accordance with our expectations. Notably, a Moiré pattern is observed in the diffraction pattern. Each primary diffraction peak of the main hexagonal structure is flanked by two closely related hexagonal patterns centered around the peaks, a characteristic manifestation of the Moiré effect [128]. A detailed analysis of this pattern suggests a (11x11) $TaSe_2$/(10x10) GaP superstructure. Taking

a lattice constant of 5.45 Å for bulk GaP, corresponding to a lattice constant of 3.85 Å in the (111) plane, it yields a $TaSe_2$ lattice parameter of 3.5±0.1 Å. This value is consistent with the in-plane lattice parameter of bulk 1T-$TaSe_2$, which is 3.48 Å [129]. The consistency of the deduced $TaSe_2$ lattice parameter with that of the bulk 1T-$TaSe_2$ phase further validates that the epilayer is indeed the 1T phase of $TaSe_2$.

X-ray Photoelectron Spectroscopy (XPS) measurements were conducted at room temperature. The results revealed a spin-orbit doublet in the Ta 4f core level, which can be further split into three distinct components, as shown in Figure 4.2f. This triplet structure supports the presence of three nonequivalent tantalum sites, which align with the unique SOD structure of the commensurate charge density wave (CCDW) phase in 1T-$TaSe_2$. Furthermore, the asymmetric nature of these peaks, which stands in contrast to the asymmetry observed in the 2H-$TaSe_2$ phase [130] [131], along with their energy and separation, are in agreement with previous XPS analyses of bulk 1T-$TaSe_2$ [132] [133]. This provides compelling evidence that $TaSe_2$ has indeed been epitaxially grown in the 1T phase. The doubling of the two peaks is a direct consequence of the CDW modulation inherent to the 1T phase. This feature is exclusive to the 1T polytype at ambient temperature, further confirming the formation of the 1T phase of $TaSe_2$.

Following the in-situ characterization, a protective 20 nm-thick selenium layer was deposited on our samples. This step is crucial in safeguarding the material from air exposure, particularly during its transfer to the scanning tunneling microscopy (STM) measurements.

4.3 Structural properties of a 1T-$TaSe_2$ monolayer on GaP(111)B

Both samples, the one grown on graphene and the other on GaP, were introduced into the STM load-lock. Here, each sample experienced a bakeout process at a temperature of 120°C for 8 hours to remove any potential contaminants, in particular water. Following this, the samples were transferred to the preparation chamber, where the protective Se layer was removed by heating the samples, using temperatures of 260°C and 270°C respectively, during 30min. These temperatures ensured an effective removal of the selenium layer. The final step involved transferring the samples into the STM analysis chamber for their surface observation. All STM measurements were performed at a temperature of 77 K.

4.3.1 Evidence for the growth of a 1T-$TaSe_2$ monolayer

Figure 4.3a presents a large-scale STM image of $TaSe_2$ grown on graphene, where we observe prominent triangular islands. These islands exhibit an approximate thickness of 0.6 nm. Additionally, scattered across the surface, we notice distinct bright bumps. A higher resolution STM image in Figure 4.3b provides a more detailed view, revealing a periodic triangular pattern of bright protrusions in the islands. The measured distance between these bright spots defines a superlattice parameter of 1.27 nm. This is consistent with a $\sqrt{13}\times\sqrt{13}$ superstructure expected in 1T-$TaSe_2$ [134] [74] [135]. Given this periodicity and the triangular arrangement, we can say that each bright spot corresponds to a SOD cluster of 13 Ta atoms.

Comparing our results to the literature, our observations align well with previous works employing both epitaxy and chemical synthesis on graphene [74] [136]. Importantly, the characteristic bright spots and their $\sqrt{13} \times \sqrt{13}$ periodicity, observed in our STM images, indicate the presence of a CDW. This CDW and the corresponding SOD arrangement are unique features of the 1T phase of TMDs. Conversely, the 1H phase typically exhibits a 3×3 superlattice reconstruction, which is distinct from our observations [137]. Additionally, in the large-scale

STM image shown in 4.3a, we observe bright spots of around 3nm in height scattered across the surface. We suspect these features to be due to folds in the underlying graphene layer, a phenomenon previously documented that can influence the properties of the graphene layer [138]. This additional feature complicates our STM measurements, as the tip tends to interact with these areas, hence, the subsequent studies will focus on $TaSe_2$ grown on GaP.

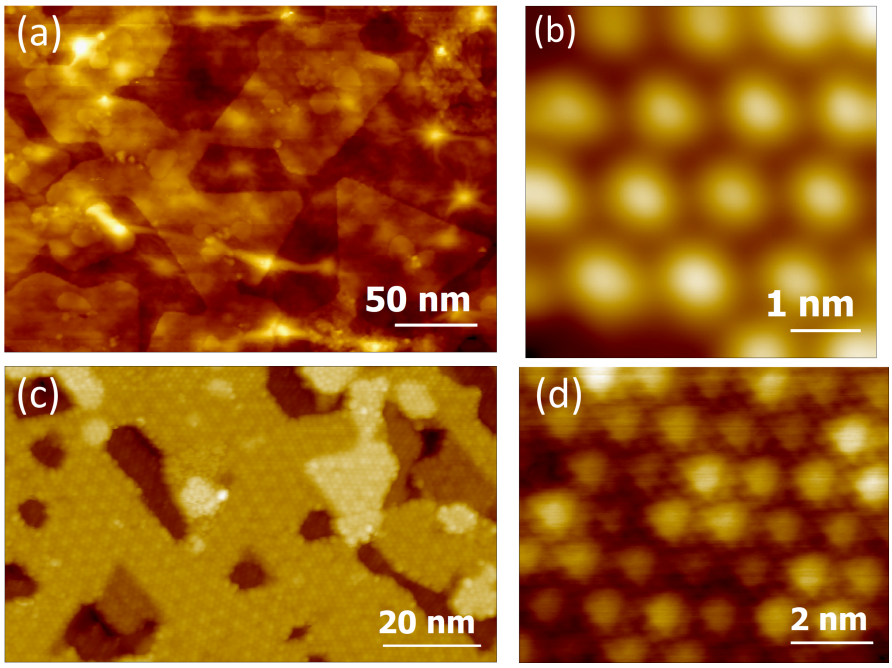

Figure 4.3: Large scale STM topography of $TaSe_2$ grown on graphene (a) and GaP (c) substrates. STM image at the resolution of the charge density wave of $TaSe_2$ grown on graphene (b) and GaP (d) substrates. Scan parameters: (a) V_{sample}=2.0 V and I=20 pA, (b) V_{sample}=5.0 V and I=40 pA, (c) V_{sample}=1.5 V and I=20 pA, (d) V_{sample}=-0.5 V and I=60 pA.

Figure 4.3c and 4.3d present STM image of $TaSe_2$ grown on GaP, revealing its structural features at two different scales. Image 4.3c is a large-scale STM image that clearly displays numerous terraces on the sample surface. The presence of these terraces indicates the formation of well-defined layers during the growth process. Additionally, a periodic lattice can be observed, which is attributed to the Moiré pattern formed between the $TaSe_2$ monolayer and the GaP substrate. A detailed discussion of the Moiré pattern will be presented in the subsequent section.

Transitioning to a more refined scale, Figure 4.3d offers a closer view of the atomic arrangement on the surface. At this scale, an entirely different periodic pattern emerges, characterized by triangular features. The observed superstructure exhibits a superlattice parameter of 1.3 nm, which is close to the value expected for the CDW $\sqrt{13}\times\sqrt{13}$ structure. Each triangle then corresponds to 13 Ta atoms clustered as a SOD.

In addition, a higher-resolution STM image, Figure 4.4b, is provided to reveal the atomic-scale details of the surface. In this image, we can observe the same triangular features similar to those in Figure 4.3d, along with bright protrusions appearing between the triangles. A schematic representation of the structure, focusing on the top layer of Se atoms, is also provided in Figure 4.4a. Each SOD contains 6 top Se atoms that form a triangle within the star. These triangles correspond to the triangular features observed in the STM image. Based on this arrangement, each bright protrusion corresponds to a Se atom. The periodicity of these small protrusions is 0.34 nm, which aligns with the in-plane 1T-$TaSe_2$ lattice parameter. [129]

In STM imaging, the tip primarily interacts with the outermost atomic layer, making it more likely to detect the Se atoms which are closer to the tip. Our schematic representation, which

focuses on the top layer of Se atoms, leads to the conclusion that Se atoms are responsible for the observed small protrusions, consistent with previous works on 1-TaS2 and 1T-NbSe2 [135] [139], unlike other studies which attribute the observed features to Ta atoms, due to their higher orbitals [74].

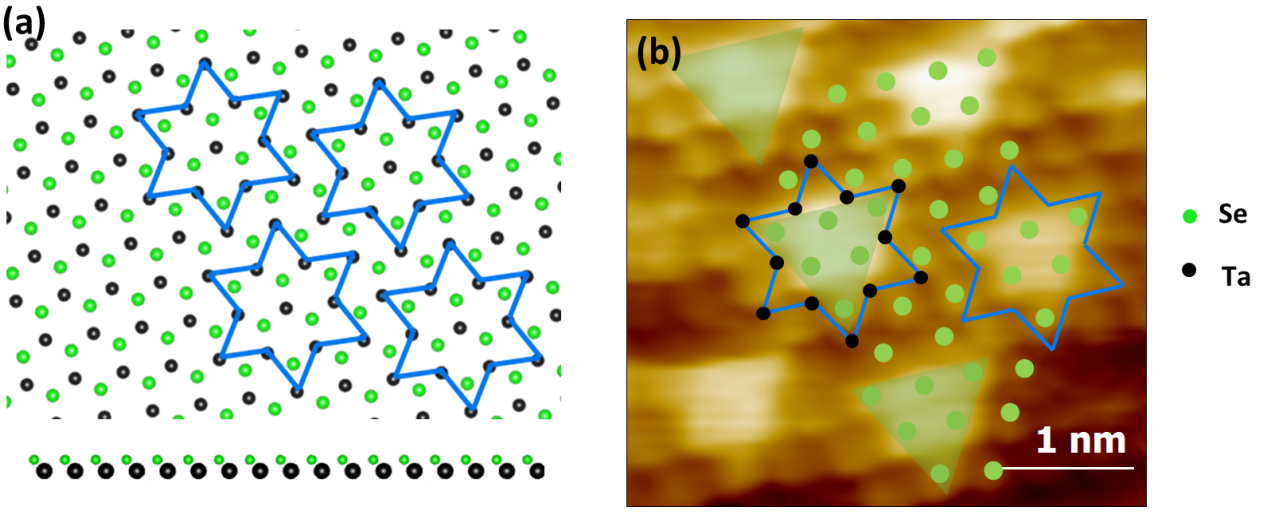

Figure 4.4: (a) Sketch of $TaSe_2$ single layer with only the top Se atoms. (b) High resolution STM image. Scan parameters V_{sample}=-0.5 V and I=70 pA.

Figure 4.5 shows a large scale STM image and the corresponding height profile. In Figure 4.5a we observe terraces of $TaSe_2$ on the GaP substrate. In Figure 4.5b, a corresponding height profile obtained from the STM image reveals a step height of 0.3 nm. Considering that the thickness of 1T-$TaSe_2$ is typically 0.63 nm [140], it is also important to note that the measured height profile of 0.3 nm matches the atomic-step height of the GaP substrate.

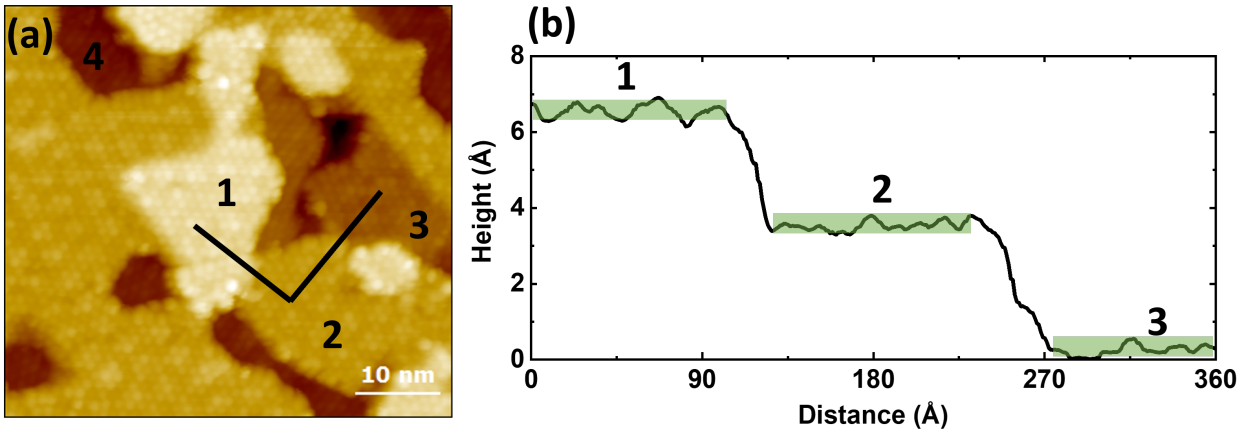

Figure 4.5: (a) STM topography of $TaSe_2$ terraces on GaP(111)B, V_{sample}=-1.5 V, I=20 pA, T=77 K. (b) Height profile measured along the black line.

4.3.2 From the lattice interaction between 1T-$TaSe_2$ and GaP

Figure 4.6a shows a STM image of the 1T-$TaSe_2$ monolayer, revealing protrusions of the expected SOD superstructure and a superlattice that takes on a flower shape. Further analysis using Fast Fourier transform (FFT), as shown in Figure 4.6d, revealed two distinct periodicities

outlined by a short green wave vector and a long red wavevector. The angle between the two periodicities is 14°.

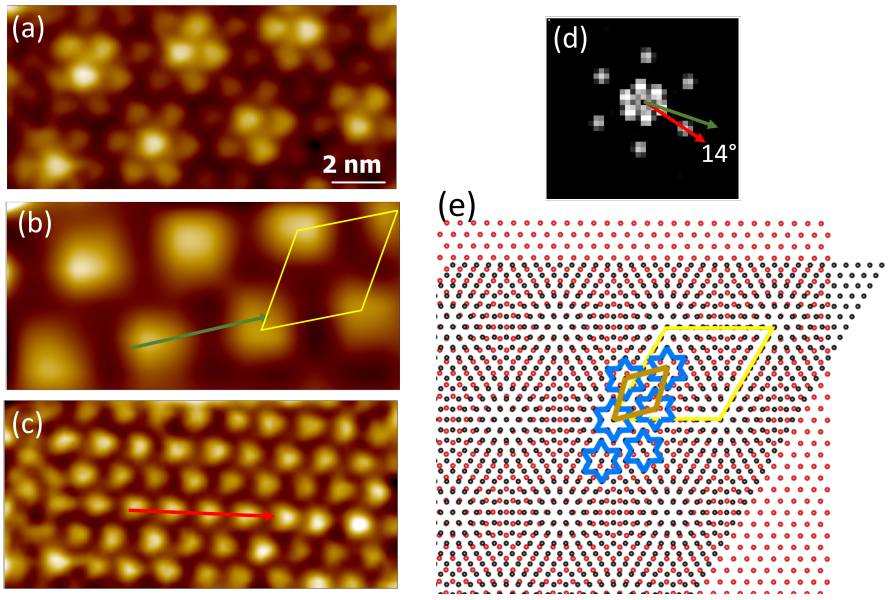

Figure 4.6: (a) STM image measured at V_{sample}=3.0 V and I=20 pA. (b) and (c) The inverse FFT of the filtered features pointed by the green and red arrows showing respectively Moiré pattern, and SOD superstructure. (d) FFT pattern of (a). The vectors represent directionality and not specific distances. (e) Schematic of the Moiré: blue stars indicate SOD, the brown and yellow diamonds indicate CDW and Moiré unit lattice. [141]

In the FFT image, two series of spots are clearly resolved. They correspond to periodicities in real space of 3.8 nm and 1.3 nm and are labelled as green and red in Figure 4.6d. An inverse FFT of the green 3.8 nm periodicity yields Figure 4.6b. Similarly, an inverse FFT of the red 1.3 nm periodicity results in Figure 4.6c, representing the SOD superstructure. As already seen in Figure 4.2e, the LEED pattern exhibits a characteristic Moiré effect with a $(11x11)_{TaSe_2}/(10x10)_{GaP}$ structure. The Moiré periodicity in the FFT, corresponding to 3.8 nm, is 10 times the GaP lattice constant, in agreement with the LEED pattern. It is worth noting that this Moiré pattern has not been observed in 1T-$TaSe_2$ samples grown on graphene and HOPG, highlighting the unique interaction between the $TaSe_2$ monolayer and the GaP substrate.

To further support the Moiré effect, Figure 4.6e illustrates a schematic representation of the 1T-$TaSe_2$ monolayer positioned on top of the Se passivation layer of GaP. Various rotations of the monolayer were tested to explore different alignment combinations. The Moiré pattern emerges when the wave vectors of the 1T-$TaSe_2$ unit cell align with the wave vectors of the GaP(111)B unit cell, resulting in the Moiré superstructure. The superlattice parameter, measured at 3.8 nm, is consistent with the STM images and supports the presence of a Moiré pattern, providing evidence for the successful growth of a 1T-$TaSe_2$ monolayer on the Se passivated GaP(111)B substrate.

However, in addition to the regular and periodic Moiré pattern, we observed a rotation of the Moiré pattern in certain areas of the STM images. These regions show deviations from the expected periodic behavior, suggesting that there may be more complex interactions or factors at play in these specific areas. Similar distortions in Moiré patterns have been reported in other materials. For example, in 1T-$TiTe_2$/1T-$TiSe_2$, atomic reconstruction at small twist angles near 0° caused local strain variations, enhancing the CDW state [142]. Heterostrain-induced deformation in twisted heterobilayer $WSe_2/MoSe_2$ led to spatial variations in the Moiré

wavelength [143]. Additionally, dislocations, point defects, and domain boundaries affecting stacking order and interlayer coupling have been shown to cause Moiré pattern distortion in twisted bilayer graphene [144].

While the Moiré pattern was observed in monolayer, it is also important to investigate the bilayer structure of 1T-$TaSe_2$.

As shown in Figure 4.7a, the STM image reveals a distinct, bright island that is elevated compared to the surrounding monolayer. Figure 4.7b presents the height profile extracted along the black line in Figure 4.7a, showing a prominence of 0.6 nm. This prominence is consistent with the thickness of a monolayer structure [140] but could also correspond to two terraces of GaP.

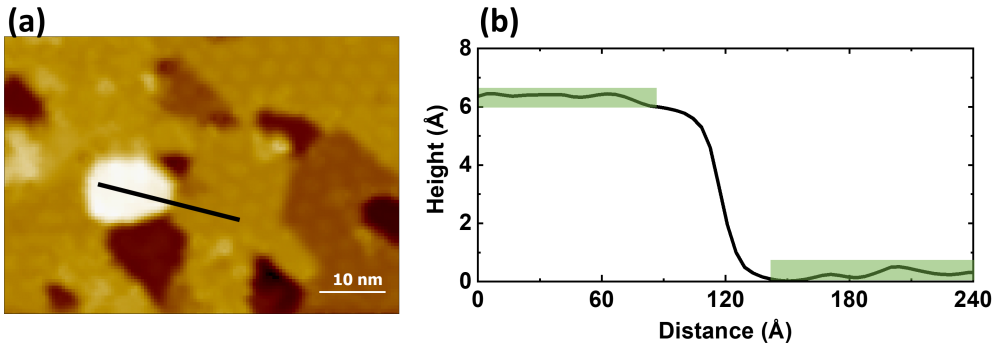

Figure 4.7: **(a)** STM image showing monolayer and bilayer 1T-$TaSe_2$. **(b)** Height profile measured along the black line.

Figure 4.8a displays a high resolution STM image of the bright island in which we observe a superstructure of bright spots with a periodicity of 1.3 nm, suggesting the presence of the CDW characteristic of the 1T-$TaSe_2$. Further, in Figure 4.8b, an atomic-resolution STM image, acquired in the same area, reveals triangular patterns associated with the CDW and composed of six protrusions. These patterns are consistent with the resolution of the Se atoms, with a contrast variation which depends on their position with respect to the centre of the SOD.

It is noteworthy that the observed structure in Figure 4.8a does not show the Moiré pattern, which is present in the monolayer. This absence is an important distinction, suggesting a difference in the interaction between layers in the bilayer compared to the monolayer and substrate. However, despite this distinction, there are several similarities between the monolayer and bilayer 1T-$TaSe_2$ that are worth highlighting.

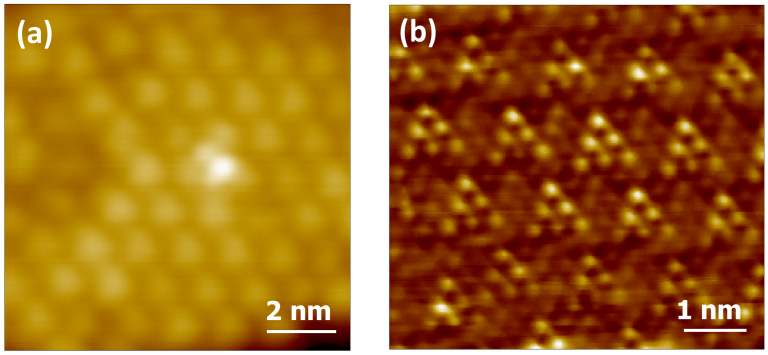

Figure 4.8: High-resolution STM images of bilayer 1T-$TaSe_2$ showing (a) the CDW superlattice and (b) the atomic resolution. Scan parameters V_{sample}=-1.0V; I=20pA and V_{sample}=-2.0V; I=20pA respectively.

Both the monolayer and bilayer 1T-$TaSe_2$ exhibit a CDW superstructure with a similar

periodicity of 1.3 nm, suggesting a common underlying ordering mechanism. Moreover, the atomic resolution images show triangular patterns associated with the CDW, and the identification of Se atoms in the bilayer closely resembles those found in the monolayer 1T-$TaSe_2$. These observations emphasize the shared features between the 1T-$TaSe_2$ monolayer and bilayer structures, and indicate that despite the absence of Moiré patterns in the bilayer, the intrinsic properties related to CDW formation are preserved.

Given the complexity of these observations, further studies are needed to fully explore and understand the origins and implications of the rotated Moiré patterns in 1T-$TaSe_2$ monolayer. Such investigations could involve more detailed STM measurements, computational modeling, or experimental studies under different conditions. These efforts would not only clarify the nature of these intriguing phenomena but also provide valuable insights into the interplay between 1T-$TaSe_2$ monolayer and GaP substrate.

4.3.3 Charge density wave chirality

In addition to the previously discussed features, the monolayer material has revealed a novel characteristic: the presence of charge density wave chirality. In scientific language, chirality refers to a distinctive property of an object or a state that prevents it from being superimposed perfectly onto its mirror image [139]. Translating this concept to charge density waves, chirality introduces an equivalent asymmetry, leading to wave patterns that display a directional preference or 'handedness'. This 'handedness' can be referred to as right-handed or left-handed chiral domains. These domains, while seemingly similar, cannot be superimposed on one another due to their distinct orientations.

Figure 4.9a shows a STM image that showcases the presence of the CDW and Moiré pattern. The inset displays the corresponding FFT, which exhibits many wavevectors on the outer skirt, separated by an angle of 28°, alongside a smaller hexagon. This arrangement is notably distinct from prior FFT observations, by doubling the number of the longuest wave vectors.

Figure 4.9c displays the inverse FFT of the reciprocal lattice defined by the smaller wave vectors. The Moiré superlattice is visible in this image, with a green rhombus superimposed to represent its unit cell. The superlattice parameter of this unit cell is measured to be 3.8 nm, in line with the previous findings.

Figures 4.9b and 4.9d together unravel the intriguing chirality feature of the CDW in our monolayer material. Figure 4.9d, displaying the inverse FFT of the larger hexagons from Figure 4.9a, vividly portrays two chiral domains of the CDW. These domains, distinguished by their orientations, are illustrated with two arrows (red and yellow) sketched in each domain to indicate the direction of the CDW. These arrows are rotated by ± 14° from a black arrow marking a high symmetry direction of the in-plane 1T-TaSe2 structure, serving as a reference. This description of multiple chiral domains is a unique characteristic of the 1T-$TaSe_2$ monolayer material, thus enriching the structural complexity of our system. Figure 4.9b further clarifies this phenomenon with a schematic diagram, including the black arrow denoting the Ta direction and two arrows rotated by ± 14°, mirroring the CDW directions in the chiral domains from Figure 4.9d. This illustration offers a concrete representation of the concept of 'handedness' or chirality within the CDW domains.

Although CDW chiral domains have not been previously reported in 1T-$TaSe_2$ material, revious research on related TMDs, notably 1T-TaS_2 thin flakes [145] and 1T-$NbSe_2$ monolayer [139], has revealed CDW chirality, a phenomenon now observed in 1T-$TaSe_2$ for the first time. In these studies, manipulation of CDW chirality was achieved through temperature variation or external electric fields. A notable observation was the 'chirality-locking effect' in 1T-TaS_2, indicative of strong interlayer binding energy for same-chirality layers. While our study focuses on monolayer systems, these findings provide a compelling direction for future investigation

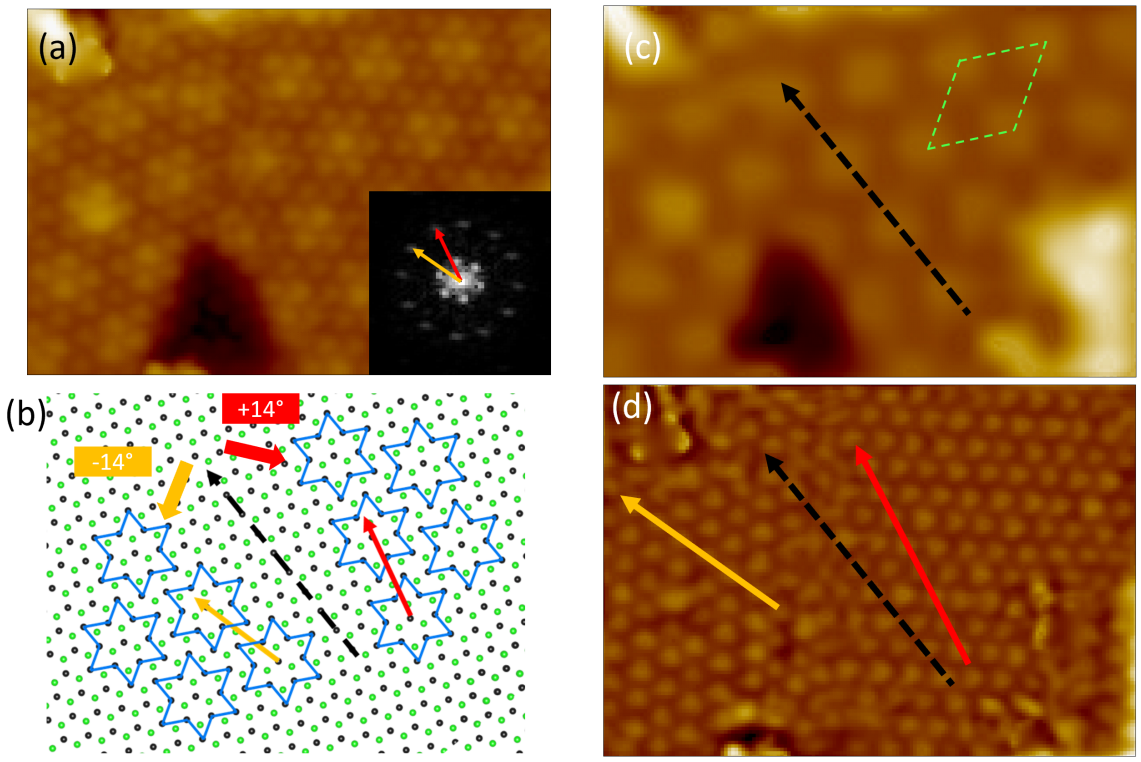

Figure 4.9: **(a)** STM image measured at V_{sample}=3.0V and I=20pA, and its FFT in inset. **(b)** Schematic of two orientations of the CDW. **(c)** and **(d)** The inverse FFT of the image in (a) to highlight the CDW patterns only. The superlattice in (c) corresponds to Moiré lattice and its unit cell is defined by the green rhombus. Arrow colors and directions are respected in figures (b), (c) and (d)

into potential interlayer effects.

The appearance of CDW chirality in our monolayer TMD material grown on GaP substrate raises intriguing questions about the influence of the substrate on the crystal structure of two-dimensional materials. Notably, similar observations have not been reported for the same material grown on other substrates such as graphene or HOPG. This suggests that the GaP substrate may play a role in the emergence of CDW chirality, although the exact mechanism remains unclear.

4.4 Electronic properties of 1T-$TaSe_2$ monolayer on GaP(111)B

In this section, we focus on the electronic properties of 1T-$TaSe_2$ monolayer grown on GaP(111)B. By employing spectroscopic analysis and macroscopic 4-probe resistance measurements, we aim to gain deeper insights into the behavior and characteristics of this material from an electronic perspective. The spectroscopic analysis facilitates a detailed examination of the electronic band structure, which is essential in understanding the fundamental electronic behavior of the monolayer. Complementing this, the 4-probe resistance measurements, performed as a function of temperature, provide invaluable macroscopic perspective into the resistance behavior of the material.

4.4.1 Electronic signature of a Mott insulator

In the spectroscopic analysis of the electronic structure of the 1T-$TaSe_2$ monolayer, the initial focus was a broad spectral bias window ranging from -2.0V to +2.0V. Utilizing this wide bias window allows us to observe a comprehensive range of electronic states in the material. Figure 4.10a presents the dI/dV spectra obtained in this range. We note the presence of the Fermi energy (E_f) at V=0, which appears slightly shifted from the center of the zero-conductance region.

For V>0, the conduction band (empty states) is probed, while for V<0, the valence band (filled states) is probed. From the spectra, the valence band edge is positioned at approximately -1.0V and the conduction band edge at about 1.3V. This results in a region of lower signal, potentially indicative of a band gap, overtaking approximately 2.3 eV within this bias window.

To ascertain the origin of these observations, we first compare the spectra with available ARPES measurements of 1T-$TaSe_2$. Interestingly, the ARPES data for 1T-$TaSe_2$ does not indicate a significant density of states around -1.2 eV [76]. However, it reveals a state centered around 0.26 eV [146], which is not in alignment with the features observed in our dI/dV spectra around -1.2 eV. This suggests that the features observed in our dI/dV spectra at this energy range are likely not due to 1T-$TaSe_2$.

Taking into account the close agreement between the observed energy range, and the known band gap of GaP at 78 K which is 2.3 eV, we conclude that the observed states are attributed to the GaP substrate. This implies that, at high bias, the 1T-$TaSe_2$ monolayer is quasi-transparent to tunneling electrons, and tunneling spectroscopy probes the electronic properties of the GaP substrate.

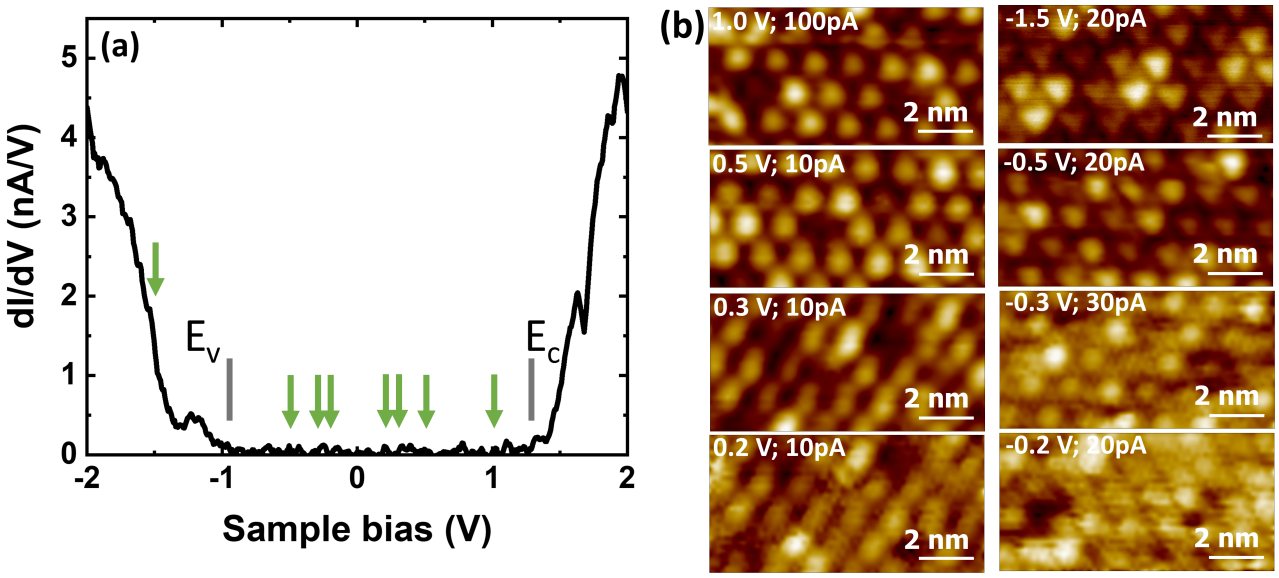

Figure 4.10: (a) dI/dV spectra measured on the 1T-TaSe2 monolayer grown on GaP(111)B. The grey vertical segments indicate the band edges of the GaP substrate. Feedback parameters: V_{sample} = -2.0 V, I = 200 pA (b) STM images acquired at different bias voltages within the band gap of GaP. The bias voltages for each image are indicated by green arrows in Figure 4.10a

Continuing with our spectroscopic analysis, Figure 4.10b showcases STM images captured at lower bias voltages ranging from 1.0 V down to -1.5 V, within the energy gap of GaP. Despite the large band gap in GaP, these images reveal intriguing features, including discernible structures that change with the bias voltage. Notably, the superstructure displayed is not consistent with

the GaP lattice, but instead characteristic of the CDW of 1T-$TaSe_2$. This implies that the tunneling current is predominantly interacting with and probing states within the 1T-$TaSe_2$ monolayer rather than the GaP substrate.

In contrast to the earlier measurements, in Figure 4.11, the feedback voltage was reduced, allowing for a smaller bias window ranging from -1 V to +1 V. Remarkably, the tunneling junction remained stable at this small bias, despite the energy being too small for electron transfer to or from the GaP substrate. It is important to note that Figure 4.11 includes multiple spectra taken at different positions across the sample, as shown in the STM image in inset, attesting to the reproducibility and consistency of the observed features. Within this smaller bias window, two distinct bands are observed.

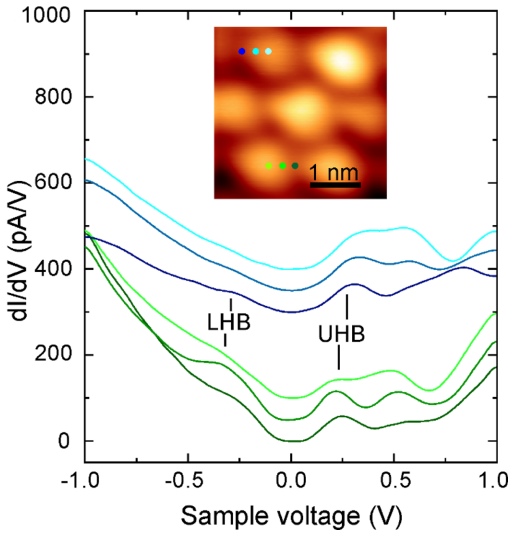

Figure 4.11: Spatially-resolved dI/dV spectra measured at the locations marked in the STM topography of the inset. Feedback parameters: V_{sample} = -1.0 V, I = 60 pA. Each spectrum exhibits zero conductance at 0 V, with the bottom spectrum presented unshifted to serve as the baseline; the other spectra are vertically shifted for clarity.

One band is centered at approximately +0.2 V, while the other is centered around -0.2 V. These bands are separated by an energy gap of about 160 meV. These bands compare well with previous works done on 1T-$TaSe_2$ monolayer grown on a graphene substrate, the positions of the bands being at 0.2 V and $-0.33V$ [74,134]. The close resemblance between the positions of the bands observed in our measurements and those reported for 1T-$TaSe_2$ on graphene strengthens the argument that these bands belong to the monolayer.

Subsequently, the band centered at approximately +0.2 V can be identified as the upper Hubbard band (UHB), and the band around -0.2 V as the lower Hubbard band (LHB) of the 1T-$TaSe_2$ monolayer. The separation between these bands and the presence of UHB and LHB are indicative of a Mott insulating state, which is consistent with the known behavior of 1T-$TaSe_2$.

4.4.2 Loss of the Mott gap

Having established the existence of a Mott insulating phase in the 1T-$TaSe_2$ monolayer as discussed in the previous section, we now explore how the conductance spectrum and the I(V) characteristics of this phase are influenced by varying set point currents.

Figure 4.12a presents the I(V) measurements with varying set point currents, within a bias range of -0.5 V to 0.5 V. The inset in Figure 4.12b shows a schematic diagram of the STM circuit, which helps in understanding the resistances involved. At low set point currents, the STM tip is

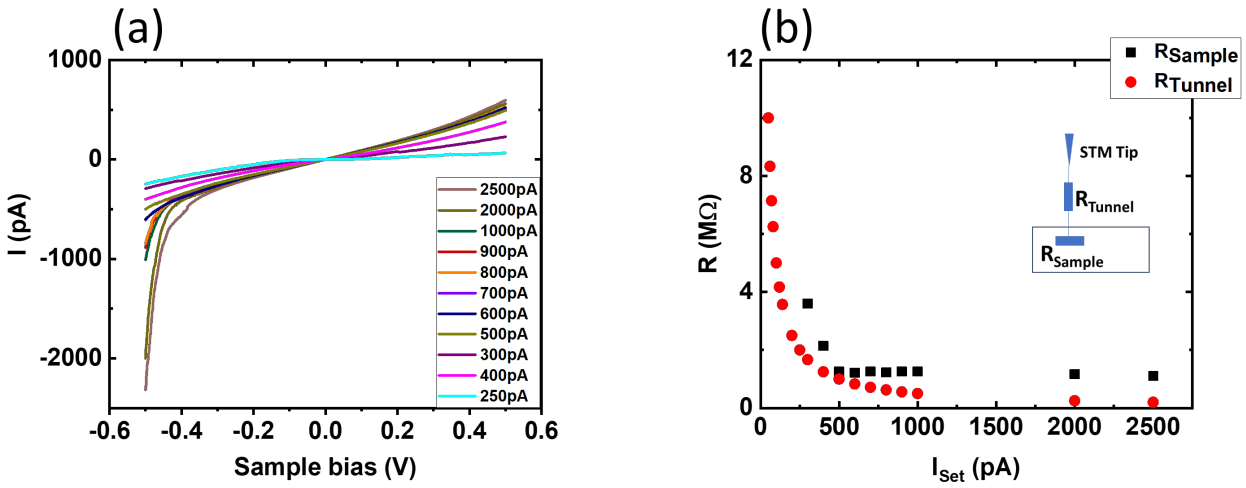

Figure 4.12: (a) I(V) characteristics acquired at different setpoint current. (b) Tunneling and sample resistances measured at different setpoint current.

far from the sample, and tunneling resistance dominates. Within this high tunneling resistance regime due to the larger distance between the tip and the sample, the I(V) curves reflect the energy gap characteristic of the Mott insulating phase of 1T-$TaSe_2$. As the set point current is increased, the distance between the STM tip and the sample decreases, which reduces the tunneling resistance. Figure 4.12b illustrates the evolution of the tunneling resistance and the resistance calculated from the I(V) curves as a function of the set point current. It is important to note that the tunneling resistance is determined over a larger voltage range, given by the feedback voltage of 0.5 V, while the resistance calculated from the I(V) curves is measured over a smaller range around 0V. Notably, at set point currents above approximately 500 pA, the resistance calculated from the I(V) curves becomes relatively constant. This indicates that the tunneling resistance is no longer the dominating factor and implies that the measurements are primarily influenced by the sample resistance. Consequently, the originally observed gap in the I(V) curves (Figure 4.12a) diminishes and eventually vanishes, leading to a more metallic-like behavior. This suggests that the system undergoes a transition, likely related to the influence of the sample resistance on the measurements.

The combined analysis of the I(V) curves and the resistance behavior sheds light on the complex interplay between tunneling and sample resistances and how they dictate the observed electronic properties of 1T-$TaSe_2$.

Moving forward, we turn our attention to how the differential conductance evolves with varying set point currents. In Figure 4.13, we present the dI/dV curves for a range of set point currents between 60 pA and 800 pA. This range was selected to emphasize the critical region where the Mott gap begins to fade, thereby enabling a detailed analysis of changes in the differential conductance at the onset of the metallic phase.

From Figure 4.13, it is evident that the Mott gap reduces in magnitude as the set point current increases. This observation is consistent with the analysis conducted with I(V) curves and reinforces the notion of a transition from a Mott insulating phase to a metallic state as the tip-sample distance is reduced. Moreover, this set of dI/dV measurements offers an in-depth spectroscopic insight into the electronic structure of monolayer 1T-$TaSe_2$, highlighting the critical role of tip-sample distance in governing the observed electronic properties.

To provide context to our observations, it is beneficial to draw comparisons with findings from existing literature. One study on 6H-SiC(0001)-3x3 exhibits transitions in the I(V) curves similar to those we observed in 1T-$TaSe_2$ as the tunneling current increased [147]. However, before delving into the specifics, it is important to understand the electronic structure of 6H-

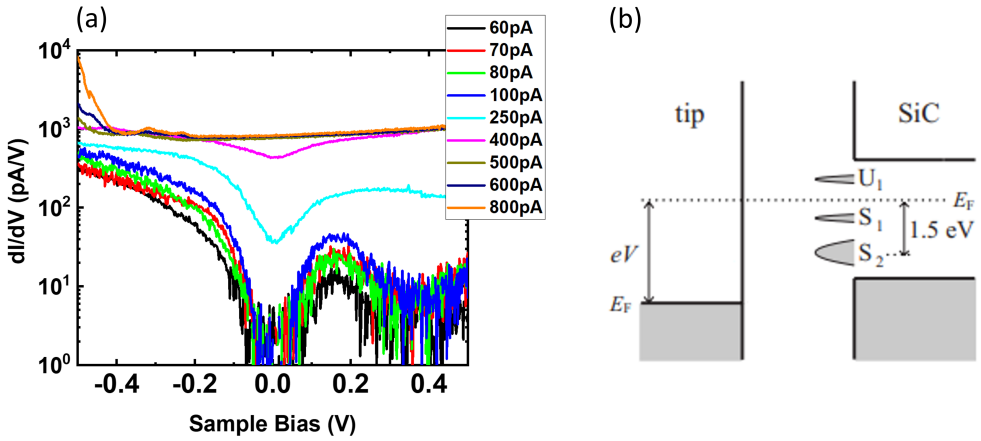

Figure 4.13: (a) dI(V)/dV spectra acquired at different setpoint current. (b) Schematic of the tunnel barrier between the STM tip and the 6H-SiC sample [147].

SiC(0001)-3x3, which is presented in Figure 4.13b. In 6H-SiC(0001)-3x3, the U1 and S1 states are surface electronic states located inside the gap. Here, U1 denotes an upper state and S1 denotes a lower state. These states originate from strongly localized and correlated electronic states, akin to the UHB and LHB in 1T-$TaSe_2$.

In the this study, a linear behavior was observed at small tip-surface distances for positive voltages, indicative of high resistance across the surface state U1. In contrast, negative voltages exhibited a nonlinear behavior at small tip-surface distances, pointing to an additional current contribution beyond the high resistance of the S1 state. This additional current is associated with an even lower state, S2, which exhibits lower resistance. Importantly, the characteristics observed in the U1 and S1 states in 6H-SiC(0001)-3x3 bear similarity to those of the UHB and LHB states in 1T-$TaSe_2$ monolayer.

In the context of the 1T-$TaSe_2$ monolayer, our observations hint at the possibility of an electric field-driven phase transition, where the decreasing tip-to-sample distance could be acting as the driving force behind this transition. Such phenomena are not exclusive to 1T-$TaSe_2$, as electric field-induced phase transitions have been reported in other materials, particularly in TMDs. For instance, in $MoTe_2$, an electric field has been demonstrated to trigger a phase transition, resulting in a transformation of its electronic properties [148, 149]. Another explanation could lie in the screening of the correlation effects by the proximity of the metal tip. As U decreases, both bands merge to form a single band.

4.4.3 Sheet resistance of 1T-$TaSe_2$ monolayer

The STM and STS experiments show the existence of a current through the 1T-$TaSe_2$ monolayer in an energy range where GaP does not conduct at 77 K. This current is injected by the STM and collected by the top metal spring of the sample holder in contact with the 1T-$TaSe_2$ epilayer. As both contacts are a few millimeter apart, it means that the 1T-TaSe2 monolayer extends to the macroscopic scale. Therefore, it is pertinent to expand our understanding by probing its electrical behavior at a macroscopic scale. This larger-scale examination is crucial for validating the broader electronic continuity and homogeneity of the monolayer, complementing the microscopic insights gained earlier. In this section, we present 4-probe resistance measurements conducted at varying temperatures to characterize the macroscopic electrical transport properties of the 1T-$TaSe_2$ monolayer. These measurements were carried out by Yevheniia Chernukha, a postdoc in our research group.

The sample under investigation consisted of a 1T-$TaSe_2$ monolayer sandwiched between a semi-insulating GaP substrate and a 30 nm thick selenium capping layer. This tri-layer

structure, illustrated in Figure 4.14a, ensured minimal interference from the substrate and preserved the integrity of the 1T-$TaSe_2$ monolayer. Following the sample preparation, the monolayer was contacted with four gold probes penetrating the selenium capping layer, as depicted in the image in Figure 4.14b. These measurements were executed in a cryogenic environment under vacuum conditions. The selenium capping layer was verified to possess good insulating behavior, which is crucial for the accuracy of the measurements. A significant current of maximum 9 μA was applied through the top probes, and the voltage drop was ascertained across the bottom ones as shown in Figure 4.14b. Utilizing the four-point probe technique, the resistance was computed using Ohm's Law, thus allowing for the exclusion of contact resistances from the measurements.

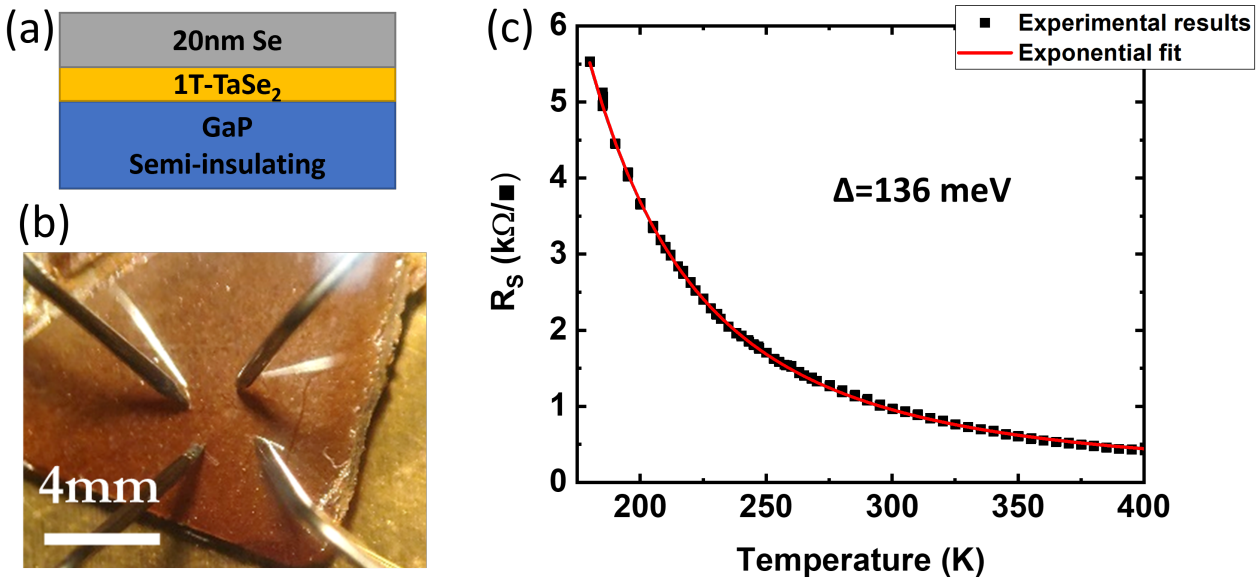

Figure 4.14: (a) Schematic of the structure configuration. (b) Illustration of the measurement configuration with gold probes contacting the $TaSe_2$ layer through a selenium cap. (c) Sheet resistance as a function of temperature.

The primary objective of these measurements was to analyze the temperature dependence of the sheet resistance (R_S) of the 1T-$TaSe_2$ monolayer between 200 K and 400 K, as depicted in Figure 4.14c. The sheet resistance (R_S), which was deduced from the electrical resistance measured with a van der Pauw configuration ($R_S = \frac{2\pi R}{\ln 2}$), revealed an exponential decrease with increasing temperature. By fitting the data to the standard activated behavior $R \propto \exp(\Delta/2k_BT)$, an energy gap of 136 meV was extracted. Intriguingly, this energy gap aligns remarkably well with the results obtained from the tunneling spectroscopy discussed earlier at 77 K, attesting to the consistency of the material electronic properties across different length scales, from nanoscale to millimeter scale. Importantly, the high resistance and its temperature dependence are indicative of an insulating phase, which corroborates the earlier findings of a Mott insulating state through STS measurements.

The compatibility of the 1T-$TaSe_2$ monolayer with both conducting and insulating substrates, as demonstrated through 4-probe resistance measurements, opens avenues for innovative electrode geometries in future device applications. Moreover, the success in contacting the 2D layer through the capping layer offers the potential for alternative electrode designs in 2D heterostructures. This compatibility, coupled with the consistent electronic properties observed across different length scales, sets the stage for the development of advanced materials and devices with adapted electronic properties.

4.5 Conclusion

In conclusion, this chapter has presented a detailed study of the structural and electronic properties of 1T-$TaSe_2$ monolayer, with a particular emphasis on the material grown on the GaP substrate. The MBE growth process has facilitated the successful deposition of the TMD monolayer. The comprehensive utilization of various characterization techniques, including RHEED, LEED, XPS, and STM/STS, has not only confirmed the formation of the TMD monolayer, but also revealed its intricate properties.

We have confirmed the existence of a charge density wave, a significant electronic property in 1T-$TaSe_2$. STM/STS measurements have provided further insights into the structure of the CDW, indicating the presence of the SOD pattern, a signature of the 1T phase. Additionally, the observation of the Moiré pattern, a phenomenon not previously reported in 1T-$TaSe_2$, adds another dimension to the complexity of its electronic properties.

The pivotal finding of this work is the clear evidence that the 1T-$TaSe_2$ monolayer on GaP exhibits the characteristics of a Mott insulator. This significant finding was confirmed through both STM/STS and 4-probe measurements. STM/STS provided local electronic insights, while 4-probe measurements validated the macroscopic insulating behavior and established the electronic continuity of the insulating layer. Furthermore, a possible aspect revealed by our study is the influence of the STM tip proximity on the electronic properties of 1T-TaSe2. This proximity effect is compatible with the presence of a resistive semiconductor/metal switch at the nanoscale, suggesting a dynamic interplay between the STM tip and the material electronic state.

The fact that the 1T-$TaSe_2$ monolayer is electronically isolated from the GaP substrate is an encouraging indication for future studies. This isolation enables the possibility of measuring in-plane electronic transport properties without substrate interference. This study thus lays the groundwork for subsequent explorations into investigating unique properties such as the quantum spin liquid state [78].

Building on the previous chapter, which explored phase transitions in $GaMo_4S_8$ for neuromorphic computing, a crucial outcome of this work on 1T-$TaSe_2$ is the identification of potential phase transitions in this material with profound implications for the field of neuromorphic computing.

Chapter 5

Conclusion

This dissertation presented an in-depth analysis of two distinct Mott insulators: $GaMo_4S_8$ crystals and monolayer 1T-$TaSe_2$.

Our study of $GaMo_4S_8$ focused on the material response to external electric fields in ultra high vacuum. A pivotal aspect of our methodological approach dealt with the use of STM tip electrodes which can be arbitrarily positionned on the surface of the crystals with a precise control of their separation. We have shown that the contact resistance between the STM tip and $GaMo_4S_8$ significantly influenced our measurements and interpretations of the threshold electric field when the phase transition occurs. Our results highlighted the importance of considering electrode-sample interactions in experimental setups, when the size of the electrode is reduced. We found that, despite the important values of the contact resistances and their variations with electrode sizes, the threshold electric field of the volatile Mott transition is around 1 kV/cm, similar to the value reported in the case of extended contacts, underlining the intrinsic character of the electric field induced Mott transition. Furthermore, we observed an increase in the delay time of the transition as the distance between electrodes grew, suggesting a spatial component in the transition process. This indicates a direct relationship between the propagation time of the phase change and the inter-electrode distance, adding a crucial dimension to our understanding of phase transitions in Mott insulators. Additionally, our experiments revealed the formation of MoS_2 filaments under conditions of high localized temperature, pointing to the necessity to better limit the current density after the transition, especially in the case where the interelectrode distance becomes smaller than few microns.

In the case of monolayer 1T-$TaSe_2$, our research confirmed its status as a Mott insulator when grown on GaP substrates. In comparison with 1T-TaSe2 grown on graphite, this discovery is quite appealing because the monolayer is continuous and electronically decoupled from the GaP substrate. Such an isolation allowed for an accurate portrayal of 1T-$TaSe_2$ inherent electronic properties, free from substrate interference, and an electron conduction confined to the monolayer only. The detection of a resistive semiconductor/metal switch at the nanoscale within 1T-$TaSe_2$ opens intriguing possibilities for its application use in nanoscale electronic devices. However, further experiments are required to fully characterize the nature of this resistive switch and to investigate the potential for volatile and nonvolatile transitions, as observed in Mott insulators crystals. This aspect of our research highlights the importance of the substrate choice in studying the intrinsic properties of 2D materials.

Our studies on $GaMo_4S_8$ and 1T-$TaSe_2$ reveal critical insights into the behavior of Mott insulators. In $GaMo_4S_8$, the discovery of neuron-like functions at room temperature opens prospects for neuromorphic computing, illustrating its potential in emulating biological synaptic activities. Additionally, the research on 1T-$TaSe_2$ has notably confirmed its robust Mott insulator status on GaP substrates at room temperature, which can contribute to the advancement of neuromorphic computing at the 2D scale.

Bibliography

[1] Masatoshi Imada, Atsushi Fujimori, and Yoshinori Tokura. Metal-insulator transitions. *Reviews of modern physics*, 70(4):1039, 1998.

[2] Nevill Mott. *Metal-insulator transitions*. CRC Press, 2004.

[3] Nevill F Mott. The basis of the electron theory of metals, with special reference to the transition metals. *Proceedings of the Physical Society. Section A*, 62(7):416, 1949.

[4] Weiwei Li, Jueli Shi, Kelvin HL Zhang, and Judith L MacManus-Driscoll. Defects in complex oxide thin films for electronics and energy applications: challenges and opportunities. *Materials Horizons*, 7(11):2832–2859, 2020.

[5] Patrick A Lee, Naoto Nagaosa, and Xiao-Gang Wen. Doping a mott insulator: Physics of high-temperature superconductivity. *Reviews of modern physics*, 78(1):17, 2006.

[6] Alberto Camjayi, C Acha, R Weht, MG Rodríguez, B Corraze, E Janod, L Cario, and Marcelo Javier Rozenberg. First-order insulator-to-metal mott transition in the paramagnetic 3d system $GaTa_4Se_8$. *Physical review letters*, 113(8):086404, 2014.

[7] Gabriel Kotliar, Sergej Y Savrasov, Kristjan Haule, Viktor S Oudovenko, O Parcollet, and CA Marianetti. Electronic structure calculations with dynamical mean-field theory. *Reviews of Modern Physics*, 78(3):865, 2006.

[8] Silke Biermann. Dynamical mean field theory-based electronic structure calculations for correlated materials. *First Principles Approaches to Spectroscopic Properties of Complex Materials*, pages 303–345, 2014.

[9] Etienne Janod, Julien Tranchant, Benoit Corraze, Madec Querré, Pablo Stoliar, Marcelo Rozenberg, Tristan Cren, Dimitri Roditchev, Vinh Ta Phuoc, Marie-Paule Besland, et al. Resistive switching in mott insulators and correlated systems. *Advanced Functional Materials*, 25(40):6287–6305, 2015.

[10] Hidehiko Kuwamoto, JM Honig, and J Appel. Electrical properties of the $(V_{1-x}Cr_x)_2O_3$ system. *Physical Review B*, 22(6):2626, 1980.

[11] Mumtaz M Qazilbash, Markus Brehm, Byung-Gyu Chae, P-C Ho, Gregory O Andreev, Bong-Jun Kim, Sun Jin Yun, AV Balatsky, MB Maple, Fritz Keilmann, et al. Mott transition in VO_2 revealed by infrared spectroscopy and nano-imaging. *Science*, 318(5857):1750–1753, 2007.

[12] SR Hassan, A Georges, and HR Krishnamurthy. Sound velocity anomaly at the mott transition: Application to organic conductors and V_2O_3. *Physical review letters*, 94(3):036402, 2005.

[13] DN Borisenko, NN Kolesnikov, IM Shmytko, NA Tulina, AV Zotov, I Yu Borisenko, and VA Tulin. Synthesizing new AM_4X_8 memristive materials for electronic applications. *Bulletin of the Russian Academy of Sciences: Physics*, 85:959–961, 2021.

[14] Regina Pocha, Dirk Johrendt, and Rainer Pöttgen. Electronic and structural instabilities in GaV_4S_8 and $GaMo_4S_8$. *Chemistry of materials*, 12(10):2882–2887, 2000.

[15] Regina Pocha, Dirk Johrendt, Bingfang Ni, and Mohsen M Abd-Elmeguid. Crystal structures, electronic properties, and pressure-induced superconductivity of the tetrahedral cluster compounds $GaNb_4S_8$, $GaNb_4Se_8$, and $GaTa_4Se_8$. *Journal of the American Chemical Society*, 127(24):8732–8740, 2005.

[16] Helen Müller, Winfried Kockelmann, and Dirk Johrendt. The magnetic structure and electronic ground states of mott insulators GeV_4S_8 and GaV_4S_8. *Chemistry of materials*, 18(8):2174–2180, 2006.

[17] Julia Mokdad, Georg Knebel, Christophe Marin, J-P Brison, V Ta Phuoc, Rodolphe Sopracase, Claire Colin, and Daniel Braithwaite. Structural, magnetic, and insulator-to-metal transitions under pressure in the GaV_4S_8 mott insulator: A rich phase diagram up to 14.7 gpa. *Physical Review B*, 100(24):245101, 2019.

[18] Mohsen Abd-Elmeguid, B Ni, Daniel I. Khomskii, Regina Pocha, Dirk Johrendt, X Wang, and K Syassen. Transition from mott insulator to superconductor in $GaNb_4Se_8$ and $GaTa_4Se_8$ under high pressure. *Physical review letters*, 93(12):126403, 2004.

[19] V Ta Phuoc, C Vaju, Benoît Corraze, Rodolphe Sopracase, A Perucchi, C Marini, Paolo Postorino, Miriam Chligui, Stefano Lupi, Etienne Janod, et al. Optical conductivity measurements of $GaTa_4Se_8$ under high pressure: Evidence of a bandwidth-controlled insulator-to-metal mott transition. *Physical review letters*, 110(3):037401, 2013.

[20] Eugen Dorolti, Laurent Cario, Benoît Corraze, Etienne Janod, Cristian Vaju, Hyun-Joo Koo, Erjun Kan, and Myung-Hwan Whangbo. Half-metallic ferromagnetism and large negative magnetoresistance in the new lacunar spinel $GaTi_3VS_8$. *Journal of the American Chemical Society*, 132(16):5704–5710, 2010.

[21] Etienne Janod, Eugen Dorolti, Benoit Corraze, Vincent Guiot, Sabrina Salmon, Viorel Pop, Frederic Christien, and Laurent Cario. Negative colossal magnetoresistance driven by carrier type in the ferromagnetic mott insulator GaV_4S_8. *Chemistry of Materials*, 27(12):4398–4404, 2015.

[22] Ádám Butykai, Sándor Bordács, István Kézsmárki, Vladimir Tsurkan, Alois Loidl, Jonathan Döring, Erik Neuber, Peter Milde, Susanne C Kehr, and Lukas M Eng. Characteristics of ferroelectric-ferroelastic domains in néel-type skyrmion host GaV_4S_8. *Scientific reports*, 7(1):44663, 2017.

[23] Laurent Cario, Julien Tranchant, Benoit Corraze, and Etienne Janod. Chapter 10 - correlated transition metal oxides and chalcogenides for mott memories and neuromorphic applications. In Panagiotis Dimitrakis, Ilia Valov, and Stefan Tappertzhofen, editors, *Metal Oxides for Non-volatile Memory*, Metal Oxides, pages 307–360. Elsevier, 2022.

[24] Pablo Stoliar, Laurent Cario, Etiene Janod, Benoit Corraze, Catherine Guillot-Deudon, Sabrina Salmon-Bourmand, Vincent Guiot, Julien Tranchant, and Marcelo Rozenberg. Universal electric-field-driven resistive transition in narrow-gap mott insulators. *Advanced materials*, 25(23):3222–3226, 2013.

[25] Matthew J Hollander, Yu Liu, Wen-Jian Lu, Li-Jun Li, Yu-Ping Sun, Joshua A Robinson, and Suman Datta. Electrically driven reversible insulator–metal phase transition in 1T-TaS_2. *Nano letters*, 15(3):1861–1866, 2015.

[26] Jerry L Hudgins. Wide and narrow bandgap semiconductors for power electronics: A new valuation. *Journal of Electronic materials*, 32:471–477, 2003.

[27] Jerry L Hudgins, Grigory S Simin, Enrico Santi, and M Asif Khan. An assessment of wide bandgap semiconductors for power devices. *IEEE Transactions on power electronics*, 18(3):907–914, 2003.

[28] Vincent Guiot, Laurent Cario, Etienne Janod, Benoît Corraze, V Ta Phuoc, Marcelo Rozenberg, Pablo Stoliar, Tristan Cren, and Dimitri Roditchev. Avalanche breakdown in $GaTa_4Se_{8-x}Te_x$ narrow-gap mott insulators. *Nature communications*, 4(1):1722, 2013.

[29] Cristian Vaju, Laurent Cario, Benoit Corraze, Etienne Janod, Vincent Dubost, Tristan Cren, Dimitri Roditchev, Daniel Braithwaite, and Olivier Chauvet. Electric-pulse-driven electronic phase separation, insulator-metal transition, and possible superconductivity in a mott insulator. *Advanced Materials (Deerfield Beach, Fla.)*, 20(14):2760–2765, 2008.

[30] Vincent Dubost, Tristan Cren, Cristian Vaju, Laurent Cario, Benoît Corraze, Etienne Janod, François Debontridder, and Dimitri Roditchev. Resistive switching at the nanoscale in the mott insulator compound $GaTa_4Se_8$. *Nano letters*, 13(8):3648–3653, 2013.

[31] Pablo Stoliar, Marcelo Rozenberg, Etienne Janod, Benoit Corraze, Julien Tranchant, and Laurent Cario. Nonthermal and purely electronic resistive switching in a mott memory. *Physical Review B*, 90(4):045146, 2014.

[32] Ryuji Okazaki, Yasuo Nishina, Yukio Yasui, Fumihiko Nakamura, Takashi Suzuki, and Ichiro Terasaki. Current-induced gap suppression in the mott insulator Ca_2RuO_4. *Journal of the Physical Society of Japan*, 82(10):103702, 2013.

[33] Yoav Kalcheim, Alberto Camjayi, Javier Del Valle, Pavel Salev, Marcelo Rozenberg, and Ivan K Schuller. Non-thermal resistive switching in mott insulator nanowires. *Nature communications*, 11(1):2985, 2020.

[34] H Fröhlich. On the theory of dielectric breakdown in solids. *Proceedings of the Royal Society of London. Series A. Mathematical and Physical Sciences*, 188(1015):521–532, 1947.

[35] Pascale Diener, Etienne Janod, B Corraze, M Querré, C Adda, Maryline Guilloux-Viry, Stéphane Cordier, Alberto Camjayi, Marcelo Rozenberg, MP Besland, et al. How a dc electric field drives mott insulators out of equilibrium. *Physical Review Letters*, 121(1):016601, 2018.

[36] Coline Adda, Benoit Corraze, Pablo Stoliar, Pascale Diener, Julien Tranchant, Agathe Filatre-Furcate, Marc Fourmigué, Dominique Lorcy, Marie-Paule Besland, Etienne Janod, et al. Mott insulators: A large class of materials for leaky integrate and fire (LIF) artificial neuron. *Journal of Applied Physics*, 124(15), 2018.

[37] Laurent Cario, Cristian Vaju, Benoit Corraze, Vincent Guiot, and Etienne Janod. Electric-field-induced resistive switching in a family of mott insulators: Towards a new class of rram memories. *Advanced Materials*, 22(45):5193–5197, 2010.

[38] Federico Tesler, Coline Adda, Julien Tranchant, Benoit Corraze, Etienne Janod, Laurent Cario, Pablo Stoliar, and Marcelo Rozenberg. Relaxation of a spiking mott artificial neuron. *Physical Review Applied*, 10(5):054001, 2018.

[39] Julien Tranchant, Etienne Janod, Benoit Corraze, Marie-Paule Besland, and Laurent Cario. From resistive switching mechanisms in AM_4Q_8 mott insulators to mott memories. In *2015 IEEE International Memory Workshop (IMW)*, pages 1–4. IEEE, 2015.

[40] Julien Tranchant, Jury Sandrini, Etienne Janod, Davide Sacchetto, Benoit Corraze, Marie-Paule Besland, Jaafar Ghanbaja, Giovanni De Micheli, Pierre-Emmanuel Gaillardon, and Laurent Cario. Control of resistive switching in mott memories based on TiN/AM_4Q_8/TiN MIM devices. *ECS Transactions*, 75(32):3, 2017.

[41] Vincent Dubost, Tristan Cren, François Debontridder, Dimitri Roditchev, Cristian Vaju, Vincent Guiot, Laurent Cario, Benoît Corraze, and Etienne Janod. Electric pulse induced electronic patchwork in the mott insulator $GaTa_4Se_8$. 2012.

[42] Danylo Babich, Julien Tranchant, Coline Adda, Benoit Corraze, Marie-Paule Besland, Peter Warnicke, Daniel Bedau, Patricia Bertoncini, Jean-Yves Mevellec, Bernard Humbert, et al. Lattice contraction induced by resistive switching in chromium-doped V_2O_3: a hallmark of mott physics. *arXiv preprint arXiv:2105.05093*, 2021.

[43] Pablo Stoliar, Julien Tranchant, Benoit Corraze, Etienne Janod, Marie-Paule Besland, Federico Tesler, Marcelo Rozenberg, and Laurent Cario. A leaky-integrate-and-fire neuron analog realized with a mott insulator. *Advanced Functional Materials*, 27(11):1604740, 2017.

[44] Coline Adda, Laurent Cario, Julien Tranchant, Etienne Janod, Marie-Paule Besland, Marcelo Rozenberg, Pablo Stoliar, and Benoit Corraze. First demonstration of "leaky integrate and fire" artificial neuron behavior on $(v_{0.95}cr_{0.05})_2o_3$ thin film. *MRS Communications*, 8(3):835–841, 2018.

[45] Yuan Cao, Valla Fatemi, Ahmet Demir, Shiang Fang, Spencer L Tomarken, Jason Y Luo, Javier D Sanchez-Yamagishi, Kenji Watanabe, Takashi Taniguchi, Efthimios Kaxiras, et al. Correlated insulator behaviour at half-filling in magic-angle graphene superlattices. *Nature*, 556(7699):80–84, 2018.

[46] Cesare Tresca, C Brun, T Bilgeri, G Menard, V Cherkez, R Federicci, D Longo, F Debontridder, M D'angelo, D Roditchev, et al. Chiral spin texture in the charge-density-wave phase of the correlated metallic pb/si (111) monolayer. *Physical Review Letters*, 120(19):196402, 2018.

[47] C Tresca, T Bilgeri, G Ménard, V Cherkez, R Federicci, D Longo, M Hervé, F Debontridder, P David, D Roditchev, et al. Importance of accurately measuring ldos maps using scanning tunneling spectroscopy in materials presenting atom-dependent charge order: The case of the correlated pb/si (111) single atomic layer. *Physical Review B*, 107(3):035125, 2023.

[48] Mohammadmehdi Torkzadeh. *Local Spectroscopy of two-dimensional correlated materials*. Theses, Sorbonne Université, March 2023.

[49] Charles Sayers. *Charge density wave phenomena in trigonal transition metal dichalcogenides*. PhD thesis, University of Bath, 2020.

[50] Ruitao Lv, Joshua A Robinson, Raymond E Schaak, Du Sun, Yifan Sun, Thomas E Mallouk, and Mauricio Terrones. Transition metal dichalcogenides and beyond: synthesis, properties, and applications of single-and few-layer nanosheets. *Accounts of chemical research*, 48(1):56–64, 2015.

[51] Yung-Chang Lin, Dumitru O Dumcenco, Ying-Sheng Huang, and Kazu Suenaga. Atomic mechanism of the semiconducting-to-metallic phase transition in single-layered MoS_2. *Nature nanotechnology*, 9(5):391–396, 2014.

[52] P Fazekas and E Tosatti. Charge carrier localization in pure and doped 1T-TaS_2. *Physica B+ C*, 99(1-4):183–187, 1980.

[53] F Jr Di Salvo, DE Moncton, and JV Waszczak. Electronic properties and superlattice formation in the semimetal $TiSe_2$. *Physical Review B*, 14(10):4321, 1976.

[54] Jerome R Long, Samuel P Bowen, and NE Lewis. Anomalous resistivity of iodine-free 2H-$NbSe_2$. *Solid State Communications*, 22(6):363–366, 1977.

[55] CF Van Bruggen and C Haas. Magnetic susceptibility and electrical properties of VS_2 single crystals. *Solid State Communications*, 20(3):251–254, 1976.

[56] C. Brun, J. C. Girard, Z. Z. Wang, J. Marcus, J. Dumas, and C. Schlenker. Charge-density waves in rubidium blue bronze $rb_{0.3}Moo_3$ observed by scanning tunneling microscopy. *Phys. Rev. B*, 72:235119, Dec 2005.

[57] Christophe Brun, Zhao-Zhong Wang, and Pierre Monceau. Scanning tunneling microscopy at the $nbse_3$ surface: Evidence for interaction between $\mathbf{q_1}$ and $\mathbf{q_2}$ charge density waves in the pinned regime. *Phys. Rev. B*, 80:045423, Jul 2009.

[58] Mongur Hossain, Zhaoyang Zhao, Wen Wen, Xinsheng Wang, Juanxia Wu, and Liming Xie. Recent advances in two-dimensional materials with charge density waves: synthesis, characterization and applications. *Crystals*, 7(10):298, 2017.

[59] Mattia Mulazzi, Ashish Chainani, Naoyuki Katayama, Ritsuko Eguchi, Masaharu Matsunami, H Ohashi, Y Senba, Minoru Nohara, M Uchida, H Takagi, et al. Absence of nesting in the charge-density-wave system 1T-VS_2 as seen by photoelectron spectroscopy. *Physical Review B*, 82(7):075130, 2010.

[60] Kun Xu, Pengzuo Chen, Xiuling Li, Changzheng Wu, Yuqiao Guo, Jiyin Zhao, Xiaojun Wu, and Yi Xie. Ultrathin nanosheets of vanadium diselenide: a metallic two-dimensional material with ferromagnetic charge-density-wave behavior. *Angewandte Chemie*, 125(40):10671–10675, 2013.

[61] VG Tissen, MR Osorio, Jean-Pascal Brison, NM Nemes, Mar García-Hernández, Laurent Cario, Pierre Rodiere, Sebastian Vieira, and Hermann Suderow. Pressure dependence of superconducting critical temperature and upper critical field of 2H-NbS_2. *Physical Review B*, 87(13):134502, 2013.

[62] Jatis K Dash, Liang Chen, Peter H Dinolfo, Toh-Ming Lu, and Gwo-Ching Wang. A method toward fabricating semiconducting 3R-NbS_2 ultrathin films. *The Journal of Physical Chemistry C*, 119(34):19763–19771, 2015.

[63] T Valla, AV Fedorov, PD Johnson, PA Glans, C McGuinness, KE Smith, EY Andrei, and H Berger. Quasiparticle spectra, charge-density waves, superconductivity, and electron-phonon coupling in 2H-$NBSe_2$. *Physical review letters*, 92(8):086401, 2004.

[64] LJ Li, WJ Lu, Y Liu, Z Qu, LS Ling, and YP Sun. Influence of defects on charge–density–wave and superconductivity in 1T-TaS_2 and 2H-TaS_2 systems. *Physica C: Superconductivity*, 492:64–67, 2013.

[65] Yijun Yu, Fangyuan Yang, Xiu Fang Lu, Ya Jun Yan, Yong-Heum Cho, Liguo Ma, Xiaohai Niu, Sejoong Kim, Young-Woo Son, Donglai Feng, et al. Gate-tunable phase transitions in thin flakes of 1T-$TaSe_2$. *Nature nanotechnology*, 10(3):270–276, 2015.

[66] R Samnakay, D Wickramaratne, TR Pope, RK Lake, TT Salguero, and AA Balandin. Zone-folded phonons and the commensurate–incommensurate charge-density-wave transition in 1T-$TaSe_2$ thin films. *Nano letters*, 15(5):2965–2973, 2015.

[67] Michio Naito and Shoji Tanaka. Electrical transport properties in 2 h-nbs2,-nbse2,-tas2 and-tase2. *Journal of the Physical Society of Japan*, 51(1):219–227, 1982.

[68] B Dardel, M Grioni, D Malterre, P Weibel, Y Baer, and F Levy. Spectroscopic observation of charge-density-wave-induced changes in the electronic structure of 2H-$TaSe_2$. *Journal of Physics: Condensed Matter*, 5(33):6111, 1993.

[69] Parviz Hajiyev, Chunxiao Cong, Caiyu Qiu, and Ting Yu. Contrast and raman spectroscopy study of single-and few-layered charge density wave material: 2H-$TaSe_2$. *Scientific reports*, 3(1):2593, 2013.

[70] Jl A Wilson, FJ Di Salvo, and S Mahajan. Charge-density waves and superlattices in the metallic layered transition metal dichalcogenides. *Advances in Physics*, 24(2):117–201, 1975.

[71] Pia C Börner, Michael Kiarie Kinyanjui, T Björkman, Tibor Lehnert, Arkady V Krasheninnikov, and Ute Kaiser. Observation of charge density waves in free-standing 1T-$TaSe_2$ monolayers by transmission electron microscopy. *Applied Physics Letters*, 113(17), 2018.

[72] Yi Chen, Wei Ruan, Jeffrey D Cain, Ryan L Lee, Salman Kahn, Caihong Jia, Alex Zettl, and Michael F Crommie. Observation of a multitude of correlated states at the surface of bulk 1T-$TaSe_2$ crystals. *Physical Review B*, 106(7):075153, 2022.

[73] Wenhao Zhang, Zongxiu Wu, Kunliang Bu, Ying Fei, Yuan Zheng, Jingjing Gao, Xuan Luo, Zheng Liu, Yu-Ping Sun, and Yi Yin. Reconciling the bulk metallic and surface insulating state in 1T-$TaSe_2$. *Physical Review B*, 105(3):035110, 2022.

[74] Yi Chen, Wei Ruan, Meng Wu, Shujie Tang, Hyejin Ryu, Hsin-Zon Tsai, Ryan L Lee, Salman Kahn, Franklin Liou, Caihong Jia, et al. Strong correlations- and orbital texture in single-layer 1T-$TaSe_2$. *Nature Physics*, 16(2):218–224, 2020.

[75] Ning Tian, Zhe Huang, Bo Gyu Jang, Shuaifei Guo, Ya-Jun Yan, Jingjing Gao, Yijun Yu, Jinwoong Hwang, Cenyao Tang, Meixiao Wang, et al. Dimensionality-driven metal to mott insulator transition in two-dimensional 1T-$TaSe_2$. *National Science Review*, page nwad144, 2023.

[76] Yuki Nakata, Katsuaki Sugawara, Ashish Chainani, Hirofumi Oka, Changhua Bao, Shaohua Zhou, Pei-Yu Chuang, Cheng-Maw Cheng, Tappei Kawakami, Yasuaki Saruta, et al. Robust charge-density wave strengthened by electron correlations in monolayer 1T-$TaSe_2$ and 1T-$NbSe_2$. *Nature Communications*, 12(1):5873, 2021.

[77] ZI Popov, NS Mikhaleva, MA Visotin, AA Kuzubov, S Entani, H Naramoto, S Sakai, PB Sorokin, and PV Avramov. The electronic structure and spin states of 2d graphene/VX_2 (X=S, Se) heterostructures. *Physical Chemistry Chemical Physics*, 18(48):33047–33052, 2016.

[78] Wei Ruan, Yi Chen, Shujie Tang, Jinwoong Hwang, Hsin-Zon Tsai, Ryan L Lee, Meng Wu, Hyejin Ryu, Salman Kahn, Franklin Liou, et al. Evidence for quantum spin liquid behaviour in single-layer 1t-tase2 from scanning tunnelling microscopy. *Nature Physics*, 17(10):1154–1161, 2021.

[79] Keiji Ueno, Toshihiro Shimada, Koichiro Saiki, and Atsushi Koma. Heteroepitaxial growth of layered transition metal dichalcogenides on sulfur-terminated gaas {111} surfaces. *Applied physics letters*, 56(4):327–329, 1990.

[80] Lin Jiao, Hong Jun Liu, JL Chen, Ya Yi, WG Chen, Yuan Cai, JN Wang, XQ Dai, Ning Wang, Wing Kin Ho, et al. Molecular-beam epitaxy of monolayer mose2: growth characteristics and domain boundary formation. *New Journal of Physics*, 17(5):053023, 2015.

[81] Debora Pierucci, Aymen Mahmoudi, Mathieu Silly, Federico Bisti, Fabrice Oehler, Gilles Patriarche, Frédéric Bonell, Alain Marty, Céline Vergnaud, Matthieu Jamet, et al. Evidence for highly p-type doping and type ii band alignment in large scale monolayer wse 2/se-terminated gaas heterojunction grown by molecular beam epitaxy. *Nanoscale*, 14(15):5859–5868, 2022.

[82] Gerd Binnig, Heinrich Rohrer, Ch Gerber, and Edmund Weibel. Surface studies by scanning tunneling microscopy. *Physical review letters*, 49(1):57, 1982.

[83] Gerd Binnig and Heinrich Rohrer. Scanning tunneling microscopy—from birth to adolescence. *Reviews of modern physics*, 59(3):615, 1987.

[84] Ahmed Soliman. Scanning tunneling microscopy (stm). 2000.

[85] Daniel R Bes. *Quantum mechanics: a modern and concise introductory course*. Springer, 2007.

[86] Nathali Alexandra Franchina Vergel. *Dirac antidot superlattices for electrons in III-V semiconductors*. PhD thesis, Université de Lille (2018-2021), 2020.

[87] Maxime Berthe. *Electronic transport in quantum confined systems*. PhD thesis, Université des Sciences et Technologie de Lille-Lille I, 2007.

[88] Jerry Tersoff and Donald R Hamann. Theory of the scanning tunneling microscope. *Physical Review B*, 31(2):805, 1985.

[89] L Limot, J Kröger, R Berndt, A Garcia-Lekue, and WA Hofer. Atom transfer and single-adatom contacts. *Physical review letters*, 94(12):126102, 2005.

[90] N Néel, J Kröger, L Limot, Thomas Frederiksen, Mads Brandbyge, and R Berndt. Controlled contact to a C60 molecule. *Physical review letters*, 98(6):065502, 2007.

[91] N Néel, J Kröger, L Limot, K Palotas, WA Hofer, and R Berndt. Conductance and kondo effect in a controlled single-atom contact. *Physical review letters*, 98(1):016801, 2007.

[92] William Sacks. Tip orbitals and the atomic corrugation of metal surfaces in scanning tunneling microscopy. *Physical review B*, 61(11):7656, 2000.

[93] Randall Feenstra, WA Thompson, and AP Fein. Real-space observation of π-bonded chains and surface disorder on Si (111) 2× 1. *Physical review letters*, 56(6):608, 1986.

[94] Randall Feenstra, Joseph A Stroscio, and AP Fein. Tunneling spectroscopy of the Si (111) 2× 1 surface. *Surface science*, 181(1-2):295–306, 1987.

[95] Davide Sciacca. *Structure and electronic properties of Ge-based 2D crystals*. PhD thesis, Université de Lille (2018-2021), 2021.

[96] Anita Roychowdhury, MA Gubrud, R Dana, JR Anderson, CJ Lobb, FC Wellstood, and M Dreyer. A 30 mk, 13.5 t scanning tunneling microscope with two independent tips. *Review of scientific instruments*, 85(4):043706, 2014.

[97] Zhouhang Wang. Challenges and advances in instrumentation of uhv lt multi-probe spm system. In *Atomic Scale Interconnection Machines: Proceedings of the 1st AtMol European Workshop Singapore 28th-29th June 2011*, pages 53–79. Springer, 2012.

[98] Shuji Hasegawa, Ichiro Shiraki, Fuhito Tanabe, Rei Hobara, Taizo Kanagawa, Takehiro Tanikawa, Iwao Matsuda, Christian L Petersen, Torben M Hansen, Peter Boggild, et al. Electrical conduction through surface superstructures measured by microscopic four-point probes. *Surface Review and Letters*, 10(06):963–980, 2003.

[99] Bert Voigtländer, Vasily Cherepanov, Stefan Korte, Arthur Leis, David Cuma, Sven Just, and Felix Lüpke. Invited review article: Multi-tip scanning tunneling microscopy: Experimental techniques and data analysis. *Review of Scientific Instruments*, 89(10), 2018.

[100] John R Arthur. Molecular beam epitaxy. *Surface science*, 500(1-3):189–217, 2002.

[101] JR Arthur Jr. Interaction of ga and as2 molecular beams with gaas surfaces. *Journal of Applied Physics*, 39(8):4032–4034, 1968.

[102] JR Arthur and JJ LePore. Gaas, gap, and gaas x p 1- x epitaxial films grown by molecular beam deposition. *Journal of Vacuum Science and Technology*, 6(4):545–548, 1969.

[103] John E Davey and Titus Pankey. Epitaxial gaas films deposited by vacuum evaporation. *Journal of Applied Physics*, 39(4):1941–1948, 1968.

[104] AY Cho and JR Arthur. Bmolecular beam epitaxy,[progr. *Solid State Chem*, 10:157–191, 1975.

[105] Jian-Ming Jin. *The finite element method in electromagnetics*. John Wiley & Sons, 2015.

[106] Walter Frei. Combining Adaptive Mesh Refinement with Data Filtering — comsol.com. `https://www.comsol.com/blogs/combining-adaptive-mesh-refinement-with-data-filtering/`, 2021. [Accessed 13-Jun-2023].

[107] Introduction to Solvers and Studies. `https://doc.comsol.com/5.5/doc/com.comsol.help.comsol/comsol_ref_solver.27.002.html`, 2015. [Accessed 12-Jun-2023].

[108] Simulation Tools for Solving Wave Electromagnetics Problems. `https://www.comsol.com/blogs/simulation-tools-for-solving-wave-electromagnetics-problems/`, 2015. [Accessed 13-Jun-2023].

[109] COMSOL Multiphysics. Comsol multiphysics user guide (version 4.3 a). *COMSOL, AB*, 39, 2012.

[110] Madec Querré, Benoit Corraze, Etienne Janod, Marie Paule Besland, Julien Tranchant, Michel Potel, Stephane Cordier, Valérie Bouquet, Maryline Guilloux-Viry, and Laurent Cario. Electric pulse induced resistive switching in the narrow gap mott insulator $GaMo_4S_8$. *Key Engineering Materials*, 617:135–140, 2014.

[111] HH Berger. Contact resistance and contact resistivity. *Journal of the Electrochemical Society*, 119(4):507, 1972.

[112] Jordan R Frick. *Non-Linear Charge Transport in the Mott Insulator α-RuCl3 and Related Materials*. North Carolina State University, 2021.

[113] R. G. Mazur and D. H. Dickey. A spreading resistance technique for resistivity measurements on silicon. *Journal of The Electrochemical Society*, 113(3):255, mar 1966.

[114] Takashi Oka and Naoto Nagaosa. Interfaces of correlated electron systems: proposed mechanism for colossal electroresistance. *Physical review letters*, 95(26):266403, 2005.

[115] H Koussir, Isabelle Lefebvre, Maxime Berthe, Y Chernukha, J Tranchant, B Corraze, Etienne Janod, Laurent Cario, B Grandidier, and Pascale Diener. Nanoprobe study of the electric field driven insulator-to-metal transition in $GaMo_4S_8$. In *Journal of Physics: Conference Series*, volume 2164, page 012046. IOP Publishing, 2022.

[116] CF Bayer, Eberhard Bär, Uwe Waltrich, Dirk Malipaard, and Andreas Schletz. Simulation of the electric field strength in the vicinity of metallization edges on dielectric substrates. *IEEE Transactions on Dielectrics and Electrical Insulation*, 22(1):257–265, 2015.

[117] David J Griffiths. Introduction to electrodynamics, 2005.

[118] Hefei Liu, Tong Wu, Xiaodong Yan, Jiangbin Wu, Nan Wang, Zhonghao Du, Hao Yang, Buyun Chen, Zhihan Zhang, Fanxin Liu, et al. A tantalum disulfide charge-density-wave stochastic artificial neuron for emulating neural statistical properties. *Nano Letters*, 21(8):3465–3472, 2021.

[119] Vincent Dubost, Tristan Cren, Cristian Vaju, Laurent Cario, Benoît Corraze, Etienne Janod, François Debontridder, and Dimitri Roditchev. Electric-field-assisted nanostructuring of a mott insulator. *Advanced Functional Materials*, 19(17):2800–2804, 2009.

[120] C Vaju, Laurent Cario, Benoît Corraze, Etienne Janod, Vincent Dubost, Tristan Cren, D Roditchev, D Braithwaite, and Olivier Chauvet. Electric-pulse-induced resistive switching and possible superconductivity in the mott insulator $GaTa_4Se_8$. *Microelectronic Engineering*, 85(12):2430–2433, 2008.

[121] E Souchier, C Vaju, V Guiot, B Corraze, E Janod, J Tranchant, P Mazoyer, M-P Besland, and L Cario. Resistive switching driven by electric field in the mott insulators AM_4X_8 (A=Ga, Ge; M=V, Nb, Ta; X= S, Se): Towards a new class of non-volatile rram memory. In *2011 3rd IEEE International Memory Workshop (IMW)*, pages 1–4. IEEE, 2011.

[122] Hong Li, Qing Zhang, Chin Chong Ray Yap, Beng Kang Tay, Teo Hang Tong Edwin, Aurelien Olivier, and Dominique Baillargeat. From bulk to monolayer MoS_2: evolution of raman scattering. *Advanced Functional Materials*, 22(7):1385–1390, 2012.

[123] Changgu Lee, Hugen Yan, Louis E Brus, Tony F Heinz, James Hone, and Sunmin Ryu. Anomalous lattice vibrations of single-and few-layer MoS_2. *ACS nano*, 4(5):2695–2700, 2010.

[124] J Orenstein and AJ Millis. Advances in the physics of high-temperature superconductivity. *Science*, 288(5465):468–474, 2000.

[125] SA Nikolaev, IV Solovyev, and SV Streltsov. Quantum spin liquid and cluster mott insulator phases in the Mo_3O_8 magnets. *npj Quantum Materials*, 6(1):25, 2021.

[126] Wei Zhao, Jie Pan, Yuqiang Fang, Xiangli Che, Dong Wang, Kejun Bu, and Fuqiang Huang. Metastable MoS_2: crystal structure, electronic band structure, synthetic approach and intriguing physical properties. *Chemistry–A European Journal*, 24(60):15942–15954, 2018.

[127] FJ Di Salvo, RG Maines, JV Waszczak, and RE Schwall. Preparation and properties of 1T-$TaSe_2$. *Solid State Communications*, 14(6):497–501, 1974.

[128] Caio C Silva, Daniela Dombrowski, Abdus Samad, Jiaqi Cai, Wouter Jolie, Joshua Hall, Paul TP Ryan, Pardeep K Thakur, David A Duncan, Tien-Lin Lee, et al. Structure of monolayer 2H-TaS_2 on Au(111). *Physical Review B*, 104(20):205414, 2021.

[129] NV Podberezskaya, SA Magarill, NV Pervukhina, and SV Borisov. Crystal chemistry of dichalcogenides MX_2. *Journal of Structural Chemistry*, 42:654–681, 2001.

[130] HE Brauer, HI Starnberg, LJ Holleboom, HP Hughes, and VN Strocov. Na and cs intercalation of 2H-$TaSe_2$ studied by photoemission. *Journal of Physics: Condensed Matter*, 13(44):9879, 2001.

[131] K Rossnagel. On the origin of charge-density waves in select layered transition-metal dichalcogenides. *Journal of Physics: Condensed Matter*, 23(21):213001, 2011.

[132] K Horiba, K Ono, JH Oh, T Kihara, S Nakazono, M Oshima, O Shiino, HW Yeom, A Kakizaki, and Y Aiura. Charge-density wave and three-dimensional fermi surface in 1T-$TaSe_2$ studied by photoemission spectroscopy. *Physical Review B*, 66(7):073106, 2002.

[133] Daniel Wolverson, Benjamin Smith, Enrico Da Como, Charles Sayers, Gary Wan, Luca Pasquali, and Mattia Cattelan. First-principles estimation of core level shifts for Hf, Ta, W, and Re. *The Journal of Physical Chemistry C*, 126(21):9135–9142, 2022.

[134] Haicheng Lin, Wantong Huang, Kun Zhao, Shuang Qiao, Zheng Liu, Jian Wu, Xi Chen, and Shuai-Hua Ji. Scanning tunneling spectroscopic study of monolayer 1T-TaS_2 and 1T-$TaSe_2$. *Nano Research*, 13:133–137, 2020.

[135] Ying Fei, Zongxiu Wu, Wenhao Zhang, and Yi Yin. Understanding the mott insulating state in 1T-TaS_2 and 1T-$TaSe_2$. *AAPPS Bulletin*, 32(1):20, 2022.

[136] Hong Wang, Yu Chen, Chao Zhu, Xuewen Wang, Hongbo Zhang, Siu Hon Tsang, Hongling Li, Jinjun Lin, Ting Yu, Zheng Liu, et al. Synthesis of atomically thin 1T-$TaSe_2$ with a strongly enhanced charge-density-wave order. *Advanced Functional Materials*, 30(34):2001903, 2020.

[137] Hyejin Ryu, Yi Chen, Heejung Kim, Hsin-Zon Tsai, Shujie Tang, Juan Jiang, Franklin Liou, Salman Kahn, Caihong Jia, Arash A Omrani, et al. Persistent charge-density-wave order in single-layer $TaSe_2$. *Nano letters*, 18(2):689–694, 2018.

[138] Ke Xu, Peigen Cao, and James R Heath. Scanning tunneling microscopy characterization of the electrical properties of wrinkles in exfoliated graphene monolayers. *Nano letters*, 9(12):4446–4451, 2009.

[139] Xuan Song, Liwei Liu, Yaoyao Chen, Han Yang, Zeping Huang, Baofei Hou, Yanhui Hou, Xu Han, Huixia Yang, Quanzhen Zhang, et al. Atomic-scale visualization of chiral charge density wave superlattices and their reversible switching. *Nature Communications*, 13(1):1843, 2022.

[140] Einar Bjerkelund, Arne Kjekshus, Åke Nilsson, Jan Sandström, H Theorell, R Blinc, S Paušak, L Ehrenberg, and J Dumanović. On the structural properties of the $Ta_{1+x}Se_2$ phase. *Acta Chem Scand*, 21:513–526, 1967.

[141] Houda Koussir, Yevheniia Chernukha, Corentin Sthioul, Emmanuel Haber, Nemanja Peric, Louis Biadala, Pierre Capiod, Maxime Berthe, Isabelle Lefebvre, X Wallart, et al. Large-area epitaxial mott insulating 1T-$TaSe_2$ monolayer on GaP(111)B. *Nano Letters*, 2023.

[142] Wei-Min Zhao, Li Zhu, Zhengwei Nie, Qi-Yuan Li, Qi-Wei Wang, Li-Guo Dou, Ju-Gang Hu, Lede Xian, Sheng Meng, and Shao-Chun Li. Moiré enhanced charge density wave state in twisted 1T-$TiTe_2$/1T-$TiSe_2$ heterostructures. *Nature Materials*, 21(3):284–289, 2022.

[143] Sara Shabani, Dorri Halbertal, Wenjing Wu, Mingxing Chen, Song Liu, James Hone, Wang Yao, Dmitri N Basov, Xiaoyang Zhu, and Abhay N Pasupathy. Deep moiré potentials in twisted transition metal dichalcogenide bilayers. *Nature Physics*, 17(6):720–725, 2021.

[144] Chun Ning Lau, Marc W Bockrath, Kin Fai Mak, and Fan Zhang. Reproducibility in the fabrication and physics of moiré materials. *Nature*, 602(7895):41–50, 2022.

[145] Manoj Singh, Boning Yu, James Huber, Bishnu Sharma, Ghilles Ainouche, Ling Fu, Jasper van Wezel, and Michael C Boyer. Lattice-driven chiral charge density wave state in 1T-TaS_2. *Physical Review B*, 106(8):L081407, 2022.

[146] L Perfetti, A Georges, Serge Florens, S Biermann, S Mitrovic, H Berger, Y Tomm, H Höchst, and M Grioni. Spectroscopic signatures of a bandwidth-controlled mott transition at the surface of 1T-$TaSe_2$. *Physical review letters*, 90(16):166401, 2003.

[147] G Baffou, AJ Mayne, G Comtet, and G Dujardin. State selective electron transport through electronic surface states of 6H-Si C (0001)-3× 3. *Physical Review B*, 77(16):165320, 2008.

[148] Feng Zhang, Huairuo Zhang, Sergiy Krylyuk, Cory A Milligan, Yuqi Zhu, Dmitry Y Zemlyanov, Leonid A Bendersky, Benjamin P Burton, Albert V Davydov, and Joerg Appenzeller. Electric-field induced structural transition in vertical $MoTe_2$-and $Mo_{1-x}W_xTe_2$-based resistive memories. *Nature materials*, 18(1):55–61, 2019.

[149] Tingxin Li, Shengwei Jiang, Lizhong Li, Yang Zhang, Kaifei Kang, Jiacheng Zhu, Kenji Watanabe, Takashi Taniguchi, Debanjan Chowdhury, Liang Fu, et al. Continuous mott transition in semiconductor moiré superlattices. *Nature*, 597(7876):350–354, 2021.

List of publications

Koussir, H., Lefebvre, I., Berthe, M., Chernukha, Y., Tranchant, J., Corraze, B., Janod, E., Cario, L., Grandidier, B. and Diener, P., 2022, March. Nanoprobe study of the electric field driven insulator-to-metal transition in $GaMo_4S_8$. In *Journal of Physics: Conference Series* (Vol. 2164, No. 1, p. 012046). IOP Publishing.

Koussir, H., Chernukha, Y., Sthioul, C., Haber, E., Peric, N., Biadala, L., Capiod, P., Berthe, M., Lefebvre, I., Wallart, X., Grandidier, B. and Diener, P., 2023. Large-area epitaxial Mott insulating 1T-TaS_2 monolayer on GaP (111)B. *Nano Letters*, 23(20), pp.9413-9419.

Nanoprobe study of the electric field driven insulator-to-metal transition in $GaMo_4S_8$

To cite this article: H. Koussir *et al* 2022 *J. Phys.: Conf. Ser.* **2164** 012046

Nanoprobe study of the electric field driven insulator-to-metal transition in $GaMo_4S_8$

H. Koussir[1], I. Lefebvre[1], M. Berthe[1], Y. Chernukha[1], J.Tranchant[2], B. Corraze[2], E. Janod[2], L. Cario[2], B. Grandidier[1] and P. Diener[1]

[1] Univ. Lille, CNRS, Centrale Lille, Univ. Polytechnique Hauts-de-France, Junia-ISEN, UMR 8520 - IEMN, F-59000 Lille, France
[2] Institut des Matériaux Jean Rouxel (IMN), Université de Nantes, CNRS, 2 Rue de la Houssinière, BP32229, 44322 Nantes Cedex 3, France

E-mail: pascale.diener@junia.com

Abstract. The resistive switching observed under electric pulses in Mott materials has a high potential for micro and nanoelectronics. Here we report on the study of the resistive switching observed at the surface of single crystals of the canonical Mott semiconductor $GaMo_4S_8$. The study is made using a multiprobe setup with 4 nanopositionable tips under the supervision of a high resolution scanning electron microscop. We find a resistivity of $38\,\Omega.cm$ by four-point probe measurements, in agreement with the literature. The volatile insulator to metal transition is studied with a two probes configuration for interelectrode distances varying between 4 and 200 microns. Finite element simulations are performed to determine the spatial distribution of the electric field prior to the transition. Our results are in agreement with i) an intrinsic voltage threshold of 60 mV independent of the interelectrode distance ii) a maximum electric field close to the electrodes and iii) a threshold electric field of 0.2 kV/cm.

1. Introduction

Mott materials exhibit an amazingly rich physics, with interesting perspectives for the micro/nanoelectronics industry [1, 2, 3]. This paper focuses on the electric field driven, volatile, insulator to metal transition observed in canonical narrow gap (0.1 - 0.5 eV) Mott insulators [4]. A voltage pulse induces an electronic avalanche specific to Mott insulators that allows the out of equilibrium system to explore a metastable metallic state [5]. The specific dynamics of the system is used to implement integrated artificial neurons [6]. In this context, the study of the transition at the nanoscaleis of high importance for the downscaling of future Mottronic devices using this transition.

2. Results

The $GaMo_4S_8$ single crystals are obtained using the method described in [5]. They are cleaved and glued with a conductive epoxy to a gold plated, p-doped silicon substrate. We checked that the sample substrate interface is sufficiently resistive in order to have a negligible contribution of the substrate to all measured sample resistances. The electrical properties have been obtained using the Nanoprobe, which consist of four Scanning Tunneling Microscop (STM) tips in an ultra high vacuum chamber, monitored under the supervision of a high resolution scanning electron microscop (SEM). The sharp tungsten tips are prepared using an electrochemical etching, and

annealed under vacuum to ensure a metallic apex. To check the quality of the tip-sample contact, current voltage measurements between each tip and the grounded substrate are performed and only tips showing a linear characteristic, associated with an ohmic contact, were considered. The sample resistance R_S is measured with the four-point probe method to avoid additional contact resistances, and with the sample substrate disconnected from the ground. Figure 1a shows a

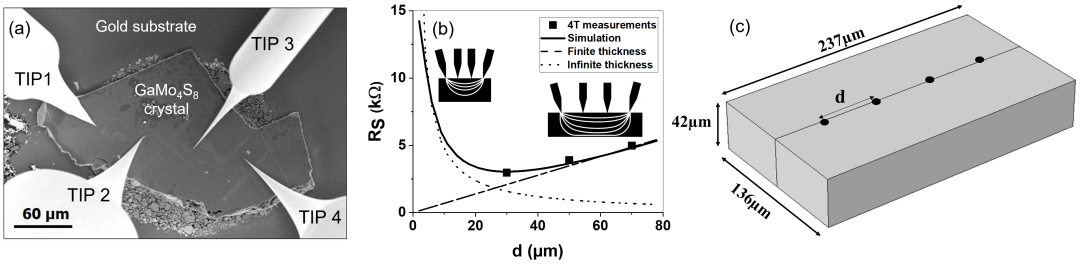

Figure 1. a) SEM picture of the $GaMo_4S_8$ single crystal S1 and the tips in the four-point probe configuration. b) Sample resistance R_S as a function of the interelectrode distance d. The experimental data are compared to simulations and to the expected analytic dependence at small d (*Infinite thickness*) and large d(*Finite thickness*). The insert shows a picture of the lines of current. c) Sample geometry used for COMSOL simulations.

typical SEM picture of a single crystal and the four STM tips. Figure 1b exhibits the variation of R_S in sample S1 for several interelectrode distances d from 30 to 70 μm. The resistance is expected to increase linearly with interelectrode distance for large values of d, and to decrease such as $R \propto 1/d$ for small d values [9]. These two limiting behaviour are pictured in Figure 1b: the first corresponds to the finite thickness case and the second corresponds to the semi infinite thickness case. Our data are expected to be in between the two regimes because the thickness is of the order of d.

Finite element simulations with COMSOL Multiphysics have been performed to fit the data, with the sample resistivity as a free parameter. Figure 1c show the sample geometry used for the simulations. The best fit, shown in Fig. 1b is obtained using a resistivity of $38\,\Omega cm$. This value is in excellent agreement with the resistivity of $40\,\Omega cm$ reported previously on single crystals of the same batch [5]. We have also compared four probes measurements $R_{4P} = R_S$ and two probes measurements $R_{2P} = R_S + 2R_c$ at the same position to estimate the contact resistance R_c at tip-sample interfaces. We find a reproducible $R_c \simeq 300k\Omega$. This value is well above the typical values ($< 1k\Omega$) obtained with the same setup on equivalent narrow gap semiconductors. Such a high contact resistance may be due to the presence of interface states specific to strongly correlated electronic systems, as discussed in [10].

We now focus on the electrical response of the sample at higher voltage using a two probes configuration and the sample floating. Figure 2a shows a typical current voltage curve measured at the surface of a $GaMo_4S_8$ single crystal. Transitions appear as a saturation of the current at threshold voltages $V^* = \pm 12,0\,V$. V^* has been measured for two samples, S2 and S3, and for different interelectrode distances. As the measurements are performed with a two probes configuration, the voltage V_S across the sample differs from V^*, due to the potential drop at the contacts. Figure 2b gives the equivalent circuit of the measured resistance between the two electrodes, $R = R_S + 2R_C$, and indicates the measured voltage threshold V^* and the voltage threshold inside the sample V_S^*. V_S^* is calculated from the voltage divider relationship $V_S^* = V^*.R_S/R$. R is determined from a linear fit in the low field, ohmic regime, as shown in the insert of Figure 1a. R_S is determined from the simulation of the resistance in S2 and S3 following the procedure used for sample S1, with the same resistivity value.

Figure 2 (c-d-e) show R, V^* and V_S^* as a function of the interelectrode distance d. In the two probes configuration, the relatively high total resistance, above $600\,k\Omega$ is mainly due to the contact resistances. The measured threshold voltage weakly increases with d for distances approximately below $50\,\mu m$, ranging from $12\,V$ to $16\,V$ and becomes independent of d above this distance. In another hand, the sample threshold voltage is $V_S^* \simeq 60 \pm 20\,mV$ with no clear dependence as a function of d.

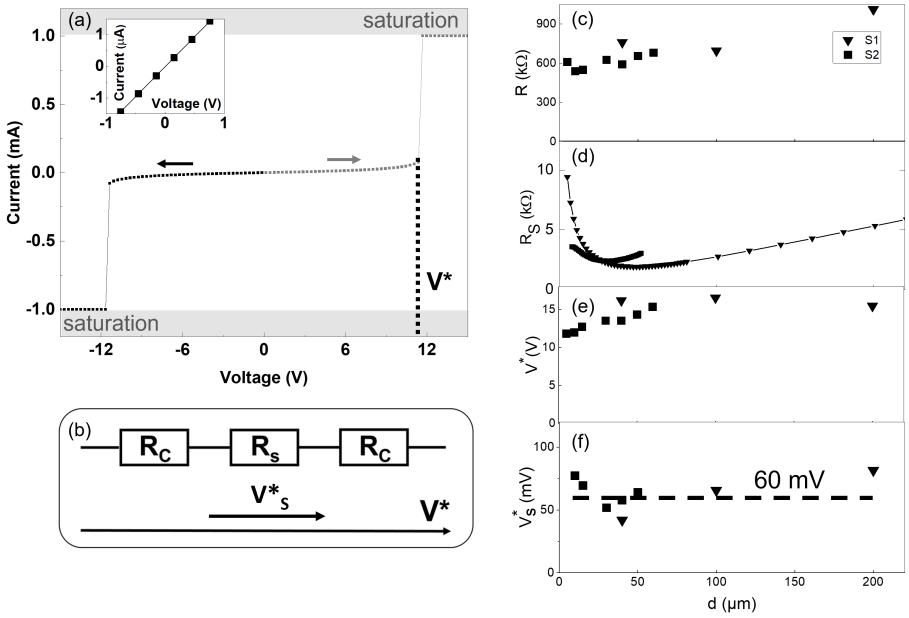

Figure 2. a) Typical current-voltage curve. V^* is the threshold voltage. Arrows indicates the voltage sweep directions. Grey areas indicate the values for which the measured current saturates. Insert: low voltage fit to determine the resistance R. b) Equivalent circuit in the two tip configuration with the contact resistances R_C and sample resistance R_S. V^* is reached for a voltage V_S^*. c,d,e,f) R, R_S, V^* and V_S^* as a function of the interelectrode distance d.

The determination of the electric field threshold E^* from V_S^* depends on the electrodes geometry. According to the literature, the insulator to metal transition occurs as soon as one sample area reaches the threshold electric field [11]. The transition then propagates from near to far up to the creation of a metallic path between the electrodes. E^* then corresponds to the maximal value of the electric field seen locally by the sample for an applied voltage $V = V_S^*$.

Figure 3 presents the simulation of the distribution of the electrical field in the sample, for an applied voltage of $60\,mV$ corresponding to V_S^*. As shown in figure 3a, the electrodes are metal contact defined as disks of radius $r = 1\,\mu m$ at the surface, separated by a distance d. An adaptative mesh as been used to resolve the field distribution. Figure 3b exhibits a typical profile of the electric field along the direction of the applied electric field, at the surface and at $500\,nm$ below. Three characteristic electric fields are labeled E_D, E_E and E_M in the figure. E_D corresponds to a divergence of the electric field at the so called triple point, because it is the junction of the sample, electrode and vacuum. E_E is located below the electrode, at the contact center, and E_M is in the middle of the interelectrode distance.

One could attribute the threshold value E^* to the electric field found at the diverging point E_D. However, we believe that E_D is not the relevant electric field, principally because our experiments show a reproducible value for the voltage threshold, independent of the probe-sample contact. In contrast E_D is expected to depends strongly on the contact geometry with

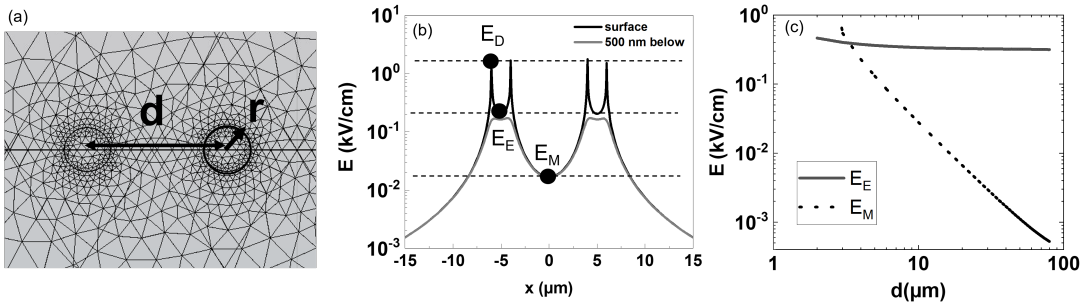

Figure 3. Comsol simulations of the electric field map in the sample for an applied voltage of $60\,mV$ a) Electrode geometry and adaptive mesh used for the simulations. d is the interelectrode distance and $r = 1\,\mu m$ is the radius of the metallic disks corresponding to the contacts. b) Electric field profile at the surface and 500 nm below. c) E_E and E_M as a function of d.

minimal values for obtuse angle contacts [12]. We rather attribute the threshold electric field to E_E, which is the maximum electric field point as soon as the divergences are excluded. Indeed, E_E corresponds to a plateau as shown figure 3b and its value varies slowly when going below the sample surface. E_E is also independent of the interelectrode distance, as shown in Figure 3c. This is compatible with the literature, because the electric field threshold is expected to be an intensive parameter. According to this analysis, we find $E^* = E_E \simeq 0.2\,kV/cm$, which compares well with the value of approximately $0.1\,kV/cm$ at ambient temperature deduced from [5]. In complement, figure 3c shows a change of regime below $d < 3\mu m$, where an increase of the electric field is expected when the electric field E_M between the electrode becomes preponderant.

3. Conclusion

The resistive switching probed at the surface of $GaMo_4S_8$ has been rationalized using Comsol simulations. The values obtained for the resistivity and the electric field threshold compare well with the literature. This study provides a framework for analysis of the resistive switching as a function of the electrodes geometry.

4. Acknowledgments

This work was supported by the RENATECH network, I-SITE ULNE (R-20-004), Hauts-de-France region and the French National Research Agency (ANR-21-CE24-0001-01).

5. References

[1] Takagi H and Hwang H Y 2010 *Science* **327** 1601–02
[2] Basov D N, Averitt R D and Hsieh D 2017 *Nat. Mater.* **16** 1077–88
[3] Wang Y, Kang K M, Kim M, Lee H S, Waser R, Wouters D, Dittmann R, Yang J J and Park H H 2019 *Materials Today* **28** 63–80
[4] Janod E. *et al. Adv. Func. Mater.* 2015 **25** 6287-305
[5] Diener P *et al.* 2018 *Phys. Rev. Lett.* **121** 016601
[6] Adda C *et al. J. Appl. Phys.* 2018 **124** 152124
[7] Dubost V, Cren T, Vaju C, Cario L, Corraze B, Janod E, Debontridder F. and Roditchev D 2013 *Nano Lett.* **13** 3648-53
[8] Durand C, Capiod P, Berthe M, Nys JP, Krzeminski C, Stiévenard D, Delerue C and Grandidier B 2014 *Nano Lett.* **14** 5636–40
[9] Miccoli I, Edler F, Pfnür H and Tegenkamp C 2015*J. Phys.: Condens. Matter* **27** 223201
[10] Oka T and Nagaosa N 2005 *Phys. Rev. Lett.* **95** 266403
[11] Stoliar P, Cario L, Janod E, Corraze B, Guillot-Deudon C, Salmon-Bourmand S, Guiot V, Tranchant J, and Rozenberg M 2013 *Adv. Mater.* **25** 3222-6
[12] Bayer C, Baer E, Waltrich U, Malipaard D and Schletz A 2015 *IEEE Trans. Dielectr. Electr. Insul.* **22** 257-65

NANO LETTERS

pubs.acs.org/NanoLett Letter

Large-Area Epitaxial Mott Insulating 1T-$TaSe_2$ Monolayer on GaP(111)B

H. Koussir, Y. Chernukha, C. Sthioul, E. Haber, N. Peric, L. Biadala, P. Capiod, M. Berthe, I. Lefebvre, X. Wallart, B. Grandidier, and P. Diener*

Cite This: *Nano Lett.* 2023, 23, 9413–9419 Read Online

ACCESS | Metrics & More | Article Recommendations | Supporting Information

ABSTRACT: Two-dimensional Mott materials have recently been reported in the dichalcogenide family with high potential for Mottronic applications. Nevertheless, their widespread use as a single or few layers is hampered by their limited device integration resulting from their growth on graphene, a metallic substrate. Here, we report on the fabrication of 1T-$TaSe_2$ monolayers grown by molecular beam epitaxy on semiconducting gallium phosphide substrates. At the nanoscale, the charge density wave reconstruction and a moiré pattern resulting from the monolayer interaction with the substrate are observed by scanning tunneling microscopy. The fully open gap unveiled by tunneling spectroscopy, which can be further manipulated by the proximity of a metal tip, is confirmed by transport measurements from micrometric to millimetric scales, demonstrating a robust Mott insulating phase at up to 400 K.

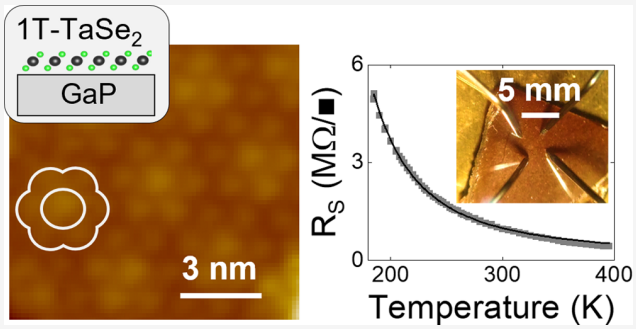

KEYWORDS: *monolayer 1T-$TaSe_2$, molecular beam epitaxy, Mott semiconductors, charge density wave, moiré*

Mott materials such as cuprates, ruthenates, or nickelates exhibit an amazingly rich physics, with several competing electronic orders such as superconductivity, charge density waves (CDW), and magnetic orders.[1−3] In some of them, in particular the narrow-gap Mott insulators, the Mott insulator−metal transitions can be triggered by optical and electric pulses with interesting perspectives for the micro- and nanoelectronics industry.[4−7] The benchmark dichalcogenide Mott material is 1T-TaS_2.[8] Just like other compounds of the MX_2 family (M = Nb, Ta, Mo, W; X = S, Se, Te), TaS_2 exhibits a lamellar hexagonal structure, with strong in-plane interactions that favor the appearance of CDW orders. In particular, the 1T polytype exhibits a CDW which is commensurate with the lattice (C-CDW) below 190 K. At this threshold, a gap appears, which is generally attributed to a CDW-driven Mott transition:[9] part of the electrons are frozen by the CDW, leaving a half-filled band at the Fermi energy, split into lower (LHB) and upper (UHB) Hubbard bands due to electronic repulsion. The correlated metal state can be recovered upon external stimuli,[10,11] but the low critical temperature limits the potential of TaS_2 for applications.

In contrast, the C-CDW survives in the selenium-based bulk compound 1T-$TaSe_2$ up to 437 K.[12] While this crystal does not develop a Mott−Hubbard band splitting because of stronger interlayer coupling than in TaS_2, an insulating behavior has been found for the surface layer and single layer grown on bilayer graphene.[13−16] Angle-resolved photoemission and scanning tunneling spectroscopy studies indicated the existence of a Mott gap up to 250 K for the surface layer[17] and up to 450 K for the single layer.[18]

Such a high temperature is essential for the development of Mottronic devices. But the growth of a 1T-$TaSe_2$ single layer on graphene, which has a much higher conductivity, hinders the study of electrical transport in the Mott crystal, calling for the use of more resistive substrates with reduced proximity effects.[19,20] Exfoliated 1T-$TaSe_2$ layers on an insulating SiO_2 layer has recently been obtained, giving valuable information on the thickness dependence of the Mott gap.[21] However, the SiO_2 surface is known to be prone to charge trapping with strong impact on the stability of the electrical properties.[22,23] Additionally, two key points must be addressed for the development of future devices. First, large $TaSe_2$ films are required, and their on-wafer process must be compatible with the microelectronics industry. Second, dichalcogenide materials, in particular 1T-$TaSe_2$, are known to be easily oxidized.[24,25] An effective in situ encapsulation method at the end of the growth is thus mandatory.

Received: July 26, 2023
Revised: October 6, 2023
Published: October 11, 2023

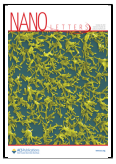

In principle, the two-dimensional structure of 1T-$TaSe_2$ allows for van der Waals epitaxy on passivated conventional semiconductor substrates. As a result, dichalcogenide thin films[26] and, more recently, single layers have been grown with molecular beam epitaxy (MBE) on GaAs.[27−29] Based on these achievements, we report the successful MBE growth of a 1T-$TaSe_2$ monolayer on a Se-terminated GaP(111)B substrate. While electron diffraction techniques and photoemission spectroscopy indicate the growth of the 1T polytype, the $TaSe_2$/GaP heterostructure was subsequently protected with a thin Se capping layer. First, low-temperature scanning tunneling microscopy (STM) performed after the sublimation of the Se cap reveals the following features: (i) the expected "Star of David" (SD) superlattice caused by the C-CDW, (ii) a superimposed Moiré pattern induced by the interaction of the monolayer with the GaP substrate, and (iii) a Mott gap in differential conductance spectroscopy at 77 K, which vanishes when spectroscopic measurements are acquired at smaller tip−sample distances. Then, four-point probe transport measurements of 1T-$TaSe_2$ monolayers grown on semi-insulating GaP substrates and still encapsulated with a resistive Se layer show a temperature-dependent characteristic of a Mott insulator up to 400 K. 1T-$TaSe_2$ on GaP thus offers a prolific playground for low-dimensionality Mott physics, CDW, and moiré related phenomena, as well as for the development of large-scale Mottronic devices at ambient temperature.

The growth experiments were carried out using an ultrahigh-vacuum system consisting of MBE chambers for the growth of III−V compounds and transition-metal dichalcogenides. The $TaSe_2$ layer was grown at 600 °C by simultaneously supplying Ta and Se on an atomically smooth Se-treated GaP(111)B-(1 × 1) surface (Figure S1). Both n-type and insulating GaP substrates were used for the following studies. The Se passivation and growth steps were monitored by in situ reflection high-energy electron diffraction (RHEED), as shown Figure 1a−d. The observation of a streaky RHEED pattern upon the growth of $TaSe_2$ reveals the formation of a smooth and well-ordered epilayer on the GaP substrate. The epilayer is aligned in-plane with the substrate and becomes more ordered upon annealing at 700 °C in a Se-rich atmosphere.

The low-energy electron diffraction (LEED) pattern measured at room temperature with an electron energy of 50 eV is displayed in Figure 1e. The image has the expected hexagonal symmetry, and the spots called "$TaSe_2$" and "GaP" are attributed to the $TaSe_2$ layer and GaP(111)B surface, respectively. This pattern together with the RHEED ones show that the hexagonal cell of $TaSe_2$ aligns with that of GaP according to the relations $[0001]TaSe_2//[\bar{1}\,\bar{1}\,\bar{1}]$ GaP out of plane and $[11\bar{2}0]TaSe_2//[1\bar{1}0]$GaP and $[1\bar{1}00]TaSe_2//[11\bar{2}]$GaP in the plane. A moiré pattern is visible, and its analysis indicates the growth of a thin epilayer with a $(11 \times 11)TaSe_2/(10 \times 10)_{GaP}$ structure, yielding a $TaSe_2$ lattice parameter of 3.5 ± 0.1 Å. This value, also confirmed by X-ray diffraction (Figure S2), is close to the 1T-$TaSe_2$ bulk lattice parameter of 3.48 Å.[30] While the core level survey measured with X-ray photoelectron spectroscopy (XPS) at room temperature shows the high purity of the $TaSe_2$ layer (Figure S3), examination of the Ta 4f core level reveals a spin−orbit doubling of the 7/2 and 5/2 lines, which can be further decomposed into three components (Figure 1f). These triplets support the existence of three different Ta sites, consistent with the nonequivalent Ta atoms in the SD structure of the C-CDW phase. Moreover, the symmetry of the peaks, which differs from the asymmetry observed for the 2H-$TaSe_2$ phase, and their position as well as their separation agree with previous XPS analysis of bulk 1T-$TaSe_2$ (Table S1), further corroborating the epitaxy of the 1T-$TaSe_2$ polytype.[31]

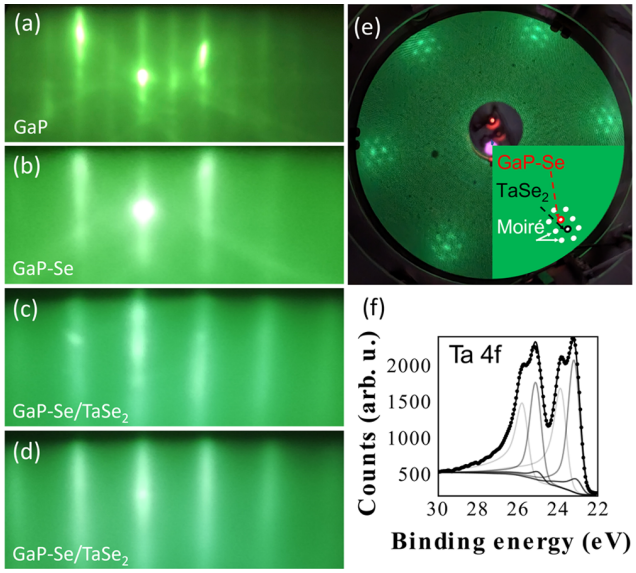

Figure 1. RHEED patterns acquired along the [11−2] azimuth for (a) the clean GaP(111)B surface, (b) the Se-treated GaP(111)B surface, (c) the growth of the $TaSe_2$ monolayer, and (d) the annealed monolayer. (e) LEED pattern of the $TaSe_2$/GaP heterostructure. The diffraction spots related to the GaP, $TaSe_2$, and moiré lattices are highlighted in red, black, and white, respectively. (f) XPS spectrum of Ta 4f measured with a photon energy of 1486.7 eV. The thin lines correspond to fits obtained with the parameters given in Table S1.

Figure 2 displays typical STM images of a $TaSe_2$ epilayer grown on a n-type GaP substrate (doping concentration of $2 \times 10^{18}cm^{-3}$) after the sample transfer through air and the subsequent sublimation of the Se cap in the preparation chamber of the STM system. The large-scale image of Figure 2a shows a majority of atomic terraces with two distinct features, a quasi-periodic flower-shaped pattern (evidenced by a white flower), which is superimposed on small protrusions (green triangles). These features are reproducibly observed on the whole surface, indicating full coverage of the GaP(111)B surface with $TaSe_2$. From the height profile in Figure 2b, we measure a step height of 3.1 ± 0.1 Å between the terraces. We note the existence of rare islands with very limited sizes, which show a height of 6.3 ± 0.1 Å (Figure S4). In these islands, the small protrusions are clearly visible, but the flower-shaped pattern is not observed whatever the bias is. As the interlayer spacing in bulk 1T-$TaSe_2$ is 6.27 Å, the terraces cannot consist of stacked layers of 1T-$TaSe_2$. Instead, a monatomic step height of 3.15 Å between the GaP (111) planes[32] implies that the GaP terraces are covered with a monolayer of $TaSe_2$.

Figure 2c shows a high-resolution STM image where the atoms of the top Se layer are atomically resolved, corresponding to an atomic lattice of 3.5 ± 0.1 Å, as expected for $TaSe_2$. The Se atoms form a bright triangular pattern rotated by an angle of 13.9° from the atomic unit cell. This pattern is at the origin of the small protrusions visible in the large scale STM image of Figure 2a. Such a superstructure is due to the SD contraction of the CDW order in the 1T phase, giving rise to a superlattice[12,15] also observed in 1T-TaS_2 and 1T-$NbSe_2$.[33,34]

https://doi.org/10.1021/acs.nanolett.3c02813
Nano Lett. 2023, 23, 9413−9419

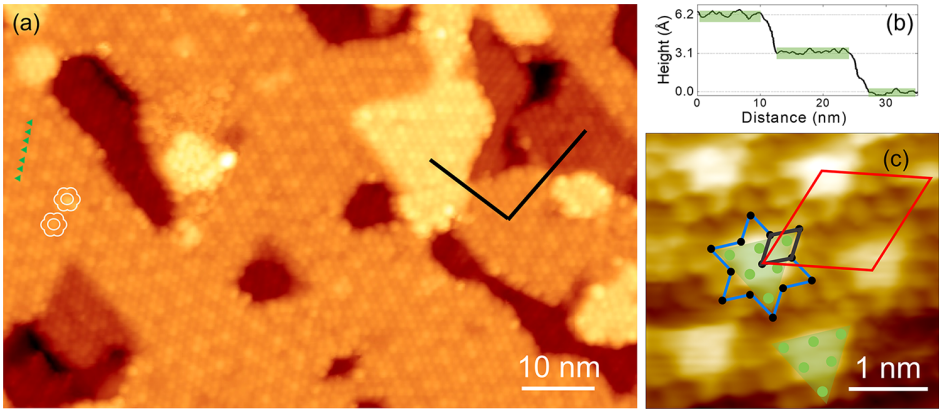

Figure 2. (a) Large-scale STM image of the $TaSe_2$ monolayer. The flowerlike reconstruction is highlighted in white, and the CDW-related protrusions are highlighted with green triangles. Feedback parameters: V_S = +1.5 V, I_t = 15 pA. (b) Height profile acquired along the black line in (a). (c) High-resolution STM image where the top Se atoms of the $TaSe_2$ layer are resolved. Feedback parameters: V_S = −0.5 V, I_t = 70 pA. The Se and Ta positions are indicated by green and black atoms, respectively, and the CDW SD pattern is indicated by a blue star. The green triangles indicate the ensemble of top Se atoms corresponding to the small periodic protrusions in (a). The black and red diamonds delineate the atomic and CDW unit cells, respectively.

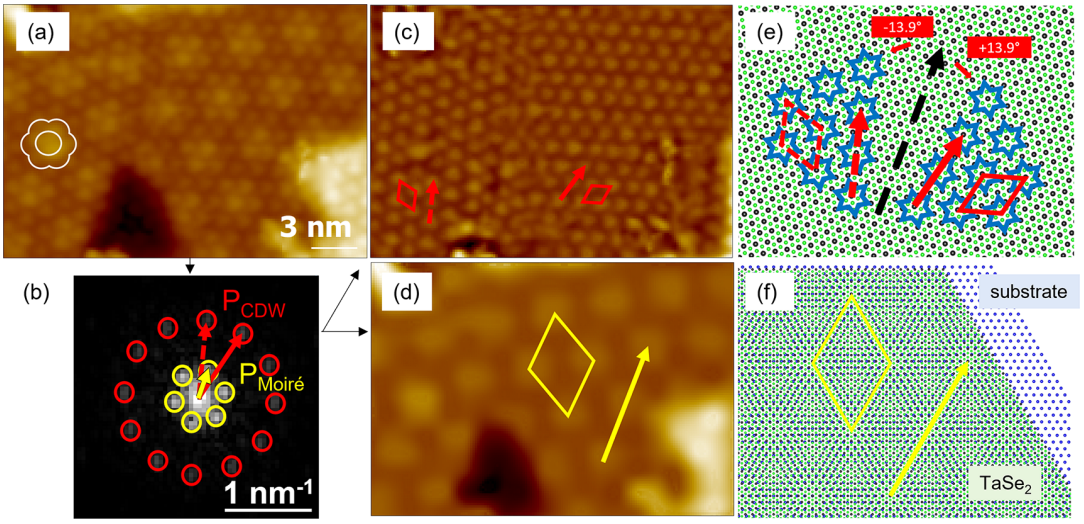

Figure 3. (a) STM image of the quasiperiodic flower-shaped superstructure observed in the 1T-$TaSe_2$ monolayer on GaP(111)B. Feedback parameters: V_S = +3.0 V, I_t = 20 pA. (b) FFT image of image (a). The spots circled in red correspond to the CDW reconstruction, and the spots circled in yellow are related to the moiré pattern. (c, d) Inverse FFT corresponding to the CDW and the moiré spots, respectively. (e) Schematic of the two possible chiral CDW orientations. The CDW unit cell is indicated as a red diamond, in either a continuous or dotted line for the two chiralities. (f) Schematic of the moiré formed by the superposition of the Se-terminated GaP substrate and the $TaSe_2$ single layer. The yellow line gives the moiré unit cell. The arrows in (b−f) underline the CDW (red) and moiré (yellow) lattice orientations. The black and green dots in (e, f) are the Ta and Se atoms, respectively, and the blue dots in (f) are the atoms at the surface of the GaP substrate (Se atoms from the GaP passivation).

Figure 3a displays an STM image at an intermediate resolution scale, in which the additional flower-shaped superstructure is highlighted. The fast Fourier transform (FFT) of Figure 3a, shown in Figure 3b, is composed of two series of peaks, denoted P_{CDW} and $P_{moiré}$. Their origin is revealed by applying inverse FFT to each series of peaks. The inverse FFT of the P_{CDW} peaks is displayed in Figure 3c and that corresponding to the $P_{moiré}$ peaks in Figure 3d. As shown in Figure 3c, the P_{CDW} peaks relate to a hexagonal lattice having a periodicity of 13.2 ± 0.4 Å that is attributed to the SD lattice parameter. Two distinct domains are visible, having the same hexagonal lattice and rotating with respect to each other by an angle of 27.8°. As sketched in Figure 3e, these domains correspond to the two equivalent chiral orientations of the SD lattice: the alignment of SDs on the surface can be tilted by either +13.9 or −13.9° compared to the atomic lattice.[35] Each chiral hexagonal domain gives rise to 6 peaks in the FFT, rotated by approximately 28° with respect to the others.

Moreover, the $P_{moiré}$ peaks are rotated by an angle of 14° compared to both series of P_{CDW} peaks, indicating that the moiré pattern is aligned with the $TaSe_2$ atomic lattice. As shown in Figure 3d, $P_{moiré}$ peaks are related to a hexagonal lattice with a periodicity of 38.6 Å. This superlattice is consistent with a moiré lattice formed by the superposition of the $TaSe_2$ layer and the GaP substrate, as sketched in Figure 3f. In this schematic, the top atoms of the substrate (Se passivation) have a unit cell of 3.85 Å, as expected for the GaP (111) surface, and the $TaSe_2$ layer has a unit cell of 3.50

https://doi.org/10.1021/acs.nanolett.3c02813
Nano Lett. 2023, 23, 9413−9419

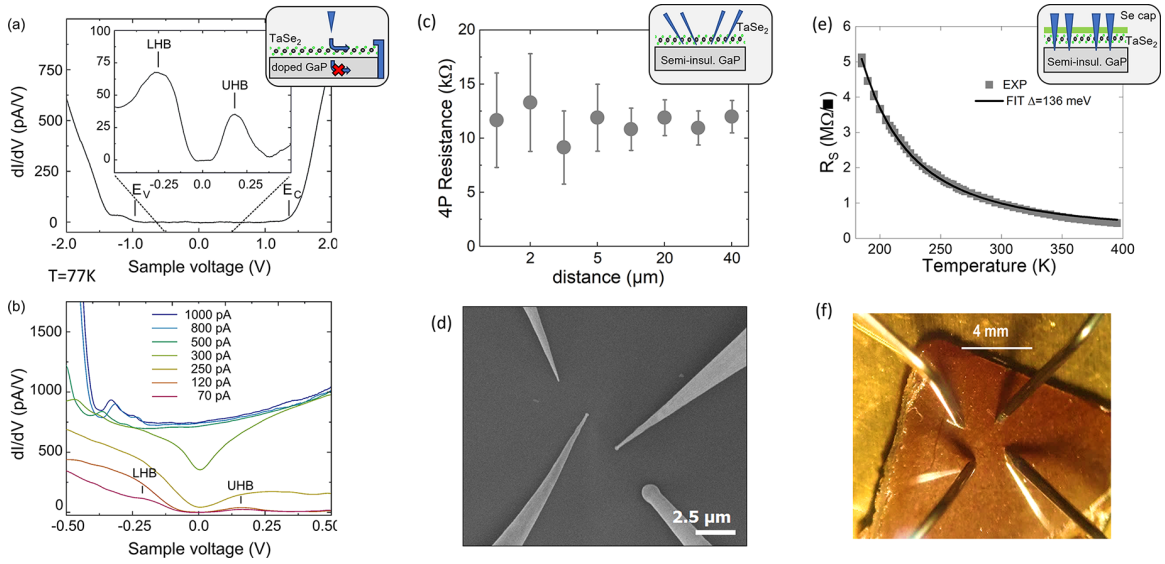

Figure 4. (a) Tunneling spectroscopy of the 1T-$TaSe_2$/GaP(111)B heterostructure. The valence and conduction band edges of the GaP substrate are indicated by vertical segments, labeled E_V and E_C. Feedback parameters: V_S = −2.0 V, I_t = 200 pA. Central inset: dI/dV spectrum acquired in a narrower energy window with different feedback parameters: V_S = −0.5 V, I_t = 20 pA. The peaks related to the lower and upper Hubbard bands are respectively labeled LHB and UHB. Top inset: illustration of the measurement configuration, with the tip tunneling on the 1T-$TaSe_2$ layer grown on a doped GaP substrate. Both the $TaSe_2$ epilayer and the doped GaP substrate are in electrical contact with the ground. The arrows indicate the allowed (without a cross) and forbidden (with a cross) paths for the electrons at energies below the band gap of GaP. (b) Tunneling spectroscopy performed on the same site at different set point currents indicated in the graph. (c) Room-temperature four-probe resistance as a function of the equidistant interelectrode distance measured in UHV. Inset: illustration of the corresponding measurement configuration. (d) Scanning electron microscopy of the four aligned and equally spaced STM tips in contact with the $TaSe_2$ layer, used for (c). (e) Sheet resistance R_S as a function of temperature measured in Se-capped $TaSe_2$ (symbols) compared with the fit described in the text (line). Inset: illustration of the transport measurement configuration. The $TaSe_2$ monolayer grown on a semi-insulating GaP substrate is protected with a Se cap, and the four electrodes are contacted across the cap. (f) Optical image of the sample and electrodes used in (e).

Å, similar to the measured value. The obtained moiré unit cell of 38.5 Å corresponds to 10 unit cells for the GaP surface and 11 $TaSe_2$ unit cells, in quantitative agreement with moiré observed in the LEED pattern (Figure 1e).

Surprisingly, the observed CDW lattice size of 13.2 ± 0.4 Å is larger than the value of 12.6 Å expected for a ($\sqrt{13} \times \sqrt{13}$ R13.9°) CDW lattice commensurable with the bulk $TaSe_2$ atomic lattice. As shown by Lin et al. in the case of $TiTe_2$ on a $PtTe_2$ substrate, a van der Waals interaction with the substrate can be at the origin of a strong modification of the CDW order present in the $TiTe_2$ monolayer.[36] The observed CDW lattice size of the $TaSe_2$ monolayer is indeed between $\sqrt{13}a_0$ = 12.6 Å and $\sqrt{13}b_0$ = 13.9 Å with a_0 and b_0 being the in-plane $TaSe_2$ and GaP(111) lattice parameters, respectively. It suggests a stretching of the CDW modulation in the $TaSe_2$ monolayer due to its proximity to the GaP substrate.

As this interaction can strongly modify the Mott gap,[36,37] tunneling spectroscopy was further performed. Figure 4a exhibits typical spectra. For feedback conditions with a large sample bias of −2.0 V, the differential conductance shows a region extending between −1.0 and +1.3 V, where the signal is below the noise level, the Fermi level being set at zero bias. Curiously, the width of this region corresponds to the theoretical band gap of GaP at 77 K (2.26 eV). Moreover, the increase of the differential conductance below −1.0 V is at odds with the dispersive bands in 1T-$TaSe_2$ monolayers grown on bilayer graphene as found in this energy range by angle-resolved photoemission spectroscopy.[18] Therefore, we attribute the increase of the signal below −1.0 V and above +1.3 V to the contribution of the valence and conduction bands of GaP. The position of the Fermi energy 1.3 eV below the conduction band of GaP indicates a depletion layer at the surface of the n-doped substrate, consistent with the band bending deduced from photoemission measurements (Figures S5 and S6). It is worth noting that STM images (Figure 2c) and spectroscopic measurements on the 1T-$TaSe_2$ monolayer can be still performed with a sample bias within the band gap of GaP. It means that the electrons predominantly propagate through the $TaSe_2$ monolayer to reach the collecting electrode located at the sample edge, a few millimeters away from the STM tip, as illustrated by the inset of Figure 4a. Setting the feedback condition for the sample bias at −0.5 V yields a differential conductance with a zero-conductance region of 0.13 ± 0.02 eV. The gap is surrounded by two peaks centered at −0.22 and +0.21 eV, with a Fermi energy in the middle of the gap, as expected for an undoped Mott semiconductor. The energy separation between the peaks of the LHB and UHB Hubbard bands, arising from the Coulomb repulsion in the monolayer, is 0.43 eV. The observed gap amplitude and positions of the Hubbard peaks are very similar to those reported for 1T-$TaSe_2$ single layers on a graphene bilayer,[15,38] indicating a negligible substrate perturbation and strong electronic correlations in $TaSe_2$. Based on spatially resolved tunneling spectroscopy (Figure S7), the LHB and UHB peaks are detected across the entire SD pattern. In contrast to previous results obtained at 4 K on 1T-$TaSe_2$ grown on bilayer graphene,[15] the amplitude of the UHB peak decreases at the center of the SD pattern but does not disappear. This could be attributed to a larger spatial extension of the electronic state at 77 K.

Interestingly, increasing the set point current causes a broadening of the LHB and UHB bands, which ends up with

https://doi.org/10.1021/acs.nanolett.3c02813
Nano Lett. 2023, 23, 9413−9419

the disappearance of the Mott gap for set point currents higher than 250 pA (Figure 4b). In this regime, the $I(V)$ characteristics show a metallic behavior, which strongly departs from the zero-current region measured around 0 V when the STM tip is far from the surface (Figure S8). This result is consistent with the behavior of the Mott−Hubbard surface states of 6H-SiC(0001), where the states do not shift but are broadened upon increasing set point currents.[39] The increasing proximity of the metallic tip modifies the electron repulsion in the bands[40] and, hence, gives rise to a transition between the two competing phases.

To confirm the macroscopic continuity of the $TaSe_2$ monolayer, four-probe transport measurements were performed at both micrometric and millimetric scales. For these experiments, an insulating GaP substrate is used to avoid an electrical conduction through the substrate. The micrometric measurements were performed with a multiple probe STM, in UHV at room temperature, after the sublimation of the Se cap. A linear arrangement of equidistant STM tips, as seen in the SEM image of Figure 4d, yields a 4P resistance that does not significantly vary with the tip separation (Figure 4c). Despite the roughness of the surface caused by the GaP terraces and the defects observed on each terrace, the electron conduction which is confined in the two-dimensional $TaSe_2$ monolayer does not degrade over tens of micrometers. This is consistent with the low temperature STM experiments, where the electrons can only escape from the sample by reaching the few-millimeter-remote top contact applied to the $TaSe_2$ monolayer. This property indicates a strong robustness of transport to defects.

Temperature-dependent resistance measurements have also been performed on the millimetric scale (Figure 4e,f). While the $TaSe_2$ epilayer is contacted with four golden probes through a 30 nm thick selenium cap in ambient air, the transport properties are further measured in a cryogenic setup under a vacuum to avoid any degradation of the sample when it is overexposed to air. All measured current−voltage characteristics exhibit an Ohmic behavior (Figure S9), from which the temperature-dependent sheet resistance R_S is deduced for a four-probe square configuration.[41] As shown in Figure 4e, the sheet resistance R_S decreases exponentially with temperatures between 200 and 400 K. Comparison of R_S with that of a sample consisting of a selenium cap without the $TaSe_2$ monolayer clearly shows that the variation of R_S is caused by the intrinsic property of the 1T-$TaSe_2$ monolayer (Figure S8). The fit with a standard activated law $R \propto \exp(\Delta/2k_BT)$ gives an energy gap of Δ = 136 meV. This is in remarkable agreement with the results from tunneling spectroscopy at 77 K, especially regarding the huge difference of the probed area, from the nanoscale to the milimeter scale. Such a result demonstrates that the 1T-$TaSe_2$ monolayer is in the Mott insulating state not only at low temperature but also at room temperature.

To conclude, 1T-$TaSe_2$ epitaxial monolayers have been grown by MBE on both doped and insulating GaP substrates. The atomic superstructure observed by STM is due to a combination of a moiré pattern with the substrate and CDW reconstruction in both chiral orientations. A Mott insulating gap is observed both at the nanoscale by STS and at the millimetric scale by four-point measurements, up to 400 K. The possibility to obtain similar 2D crystals on either conducting or insulating GaP substrates, with an efficient selenium encapsulation, is suitable for both lateral and transverse electrode geometries in future device applications. Besides unveiling stimulating results on the moiré and Mott-CDW physics, the long-range electrical transport and the manipulation of the Mott gap in tunneling spectroscopy at the local scale pave the way toward the growth of large-scale 2D Mott materials and their integration in functional devices at ambient temperature.

■ ASSOCIATED CONTENT

Supporting Information

The Supporting Information is available free of charge at https://pubs.acs.org/doi/10.1021/acs.nanolett.3c02813.

Experimental methods and additional experimental results (PDF)

■ AUTHOR INFORMATION

Corresponding Author

P. Diener − *Univ. Lille, CNRS, Centrale Lille, Univ. Polytechnique Hauts-de-France, Junia-ISEN, UMR 8520 - IEMN, F-59000 Lille, France;* orcid.org/0000-0002-9685-2982; Email: pascale.diener@junia.com

Authors

H. Koussir − *Univ. Lille, CNRS, Centrale Lille, Univ. Polytechnique Hauts-de-France, Junia-ISEN, UMR 8520 - IEMN, F-59000 Lille, France*

Y. Chernukha − *Univ. Lille, CNRS, Centrale Lille, Univ. Polytechnique Hauts-de-France, Junia-ISEN, UMR 8520 - IEMN, F-59000 Lille, France*

C. Sthioul − *Univ. Lille, CNRS, Centrale Lille, Univ. Polytechnique Hauts-de-France, Junia-ISEN, UMR 8520 - IEMN, F-59000 Lille, France*

E. Haber − *Univ. Lille, CNRS, Centrale Lille, Univ. Polytechnique Hauts-de-France, Junia-ISEN, UMR 8520 - IEMN, F-59000 Lille, France*

N. Peric − *Univ. Lille, CNRS, Centrale Lille, Univ. Polytechnique Hauts-de-France, Junia-ISEN, UMR 8520 - IEMN, F-59000 Lille, France*

L. Biadala − *Univ. Lille, CNRS, Centrale Lille, Univ. Polytechnique Hauts-de-France, Junia-ISEN, UMR 8520 - IEMN, F-59000 Lille, France;* orcid.org/0000-0002-1953-9095

P. Capiod − *Univ. Lille, CNRS, Centrale Lille, Univ. Polytechnique Hauts-de-France, Junia-ISEN, UMR 8520 - IEMN, F-59000 Lille, France*

M. Berthe − *Univ. Lille, CNRS, Centrale Lille, Univ. Polytechnique Hauts-de-France, Junia-ISEN, UMR 8520 - IEMN, F-59000 Lille, France*

I. Lefebvre − *Univ. Lille, CNRS, Centrale Lille, Univ. Polytechnique Hauts-de-France, Junia-ISEN, UMR 8520 - IEMN, F-59000 Lille, France*

X. Wallart − *Univ. Lille, CNRS, Centrale Lille, Univ. Polytechnique Hauts-de-France, Junia-ISEN, UMR 8520 - IEMN, F-59000 Lille, France*

B. Grandidier − *Univ. Lille, CNRS, Centrale Lille, Univ. Polytechnique Hauts-de-France, Junia-ISEN, UMR 8520 - IEMN, F-59000 Lille, France;* orcid.org/0000-0001-6131-7309

Complete contact information is available at: https://pubs.acs.org/10.1021/acs.nanolett.3c02813

https://doi.org/10.1021/acs.nanolett.3c02813
Nano Lett. 2023, 23, 9413−9419

Notes

The authors declare no competing financial interest.

■ ACKNOWLEDGMENTS

This work was partly funded by the RENATECH network (PCMP-PCP and CMNF), I-SITE ULNE (R-20-004), Hauts-de-France region, and the French National Research Agency (ANR-21-CE24-0030 Tunne2D and ANR-21-CE24-0001-01 Nanodyn). A CC-BY public copyright license has been applied by the authors to the present document and will be applied to all subsequent versions up to the Author Accepted Manuscript arising from this submission, in accordance with the grant's open access conditions.

■ REFERENCES

(1) Lee, P. A.; Nagaosa, N.; Wen, X.-G. Doping a Mott insulator: Physics of high-temperature superconductivity. *Rev. Mod. Phys.* **2006**, *78*, 17−85.
(2) Li, D.; Lee, K.; Wang, B. Y.; Osada, M.; Crossley, S.; Lee, H. R.; Cui, Y.; Hikita, Y.; Hwang, H. Y. Superconductivity in an infinite-layer nickelate. *Nature* **2019**, *572*, 624−627.
(3) Yatsuzuka, H.; Haraguchi, Y.; Matsuo, A.; Kindo, K.; Katori, H. A. Spin-glass transition in the spin−orbit-entangled Jeff = 0 Mott insulating double-perovskite ruthenate. *Sci. Rep* **2022**, *12*, 2429.
(4) Takagi, H.; Hwang, H. Y. An Emergent Change of Phase for Electronics. *Science* **2010**, *327*, 1601−1602.
(5) Basov, D. N.; Averitt, R. D.; Hsieh, D. Towards properties on demand in quantum materials. *Nat. Mater.* **2017**, *16*, 1077−1088.
(6) Pickett, M. D.; Medeiros-Ribeiro, G.; Williams, R. S. A scalable neuristor built with Mott memristors. *Nat. Mater.* **2013**, *12*, 114−117.
(7) Ran, Y.; Pei, Y.; Zhou, Z.; Wang, H.; Sun, Y.; Wang, Z.; Hao, M.; Zhao, J.; Chen, J.; Yan, X. A review of Mott insulator in memristors: The materials, characteristics, applications for future computing systems and neuromorphic computing. *Nano Res.* **2023**, *16*, 1165−1182.
(8) Sipos, B.; Kusmartseva, A. F.; Akrap, A.; Berger, H.; Forró, L.; Tutiš, E. From Mott state to superconductivity in 1T-TaS2. *Nat. Mater.* **2008**, *7*, 960−965.
(9) Ritschel, T.; Trinckauf, J.; Koepernik, K.; Büchner, B.; Zimmermann, M. v.; Berger, H.; Joe, Y. I.; Abbamonte, P.; Geck, J. Orbital textures and charge density waves in transition metal dichalcogenides. *Nature Phys.* **2015**, *11*, 328−331.
(10) Stojchevska, L.; Vaskivskyi, I.; Mertelj, T.; Kusar, P.; Svetin, D.; Brazovskii, S.; Mihailovic, D. Ultrafast Switching to a Stable Hidden Quantum State in an Electronic Crystal. *Science* **2014**, *344*, 177−180.
(11) Yoshida, M.; Suzuki, R.; Zhang, Y.; Nakano, M.; Iwasa, Y. Memristive phase switching in two-dimensional 1T-TaS2 crystals. *Sci. Adv.* **2015**, *1*, No. e1500606.
(12) Wilson, J. A.; Di Salvo, F. J.; Mahajan, S. Charge-Density Waves in Metallic, Layered, Transition-Metal Dichalcogenides. *Phys. Rev. Lett.* **1974**, *32*, 882−885.
(13) Perfetti, L.; Georges, A.; Florens, S.; Biermann, S.; Mitrovic, S.; Berger, H.; Tomm, Y.; Höchst, H.; Grioni, M. Spectroscopic Signatures of a Bandwidth-Controlled Mott Transition at the Surface of 1T-TaSe2. *Phys. Rev. Lett.* **2003**, *90*, 166401.
(14) Nakata, Y.; Yoshizawa, T.; Sugawara, K.; Umemoto, Y.; Takahashi, T.; Sato, T. Selective Fabrication of Mott-Insulating and Metallic Monolayer TaSe2. *ACS Appl. Nano Mater.* **2018**, *1*, 1456−1460.
(15) Chen, Y.; et al. Strong correlations and orbital texture in single-layer 1T-TaSe 2. *Nat. Phys.* **2020**, *16*, 218−224.
(16) Chen, Y.; Ruan, W.; Cain, J. D.; Lee, R. L.; Kahn, S.; Jia, C.; Zettl, A.; Crommie, M. F. Observation of a multitude of correlated states at the surface of bulk 1T-TaSe2 crystals. *Phys. Rev. B* **2022**, *106*, 075153.
(17) Colonna, S.; Ronci, F.; Cricenti, A.; Perfetti, L.; Berger, H.; Grioni, M. Mott Phase at the Surface of 1T-TaSe2 Observed by Scanning Tunneling Microscopy. *Phys. Rev. Lett.* **2005**, *94*, 036405.
(18) Nakata, Y.; Sugawara, K.; Chainani, A.; Oka, H.; Bao, C.; Zhou, S.; Chuang, P.-Y.; Cheng, C.-M.; Kawakami, T.; Saruta, Y.; Fukumura, T.; Zhou, S.; Takahashi, T.; Sato, T. Robust charge-density wave strengthened by electron correlations in monolayer 1T-TaSe2 and 1T-NbSe2. *Nat. Commun.* **2021**, *12*, 5873.
(19) Chen, Y.; Wu, L.; Xu, H.; Cong, C.; Li, S.; Feng, S.; Zhang, H.; Zou, C.; Shang, J.; Yang, S. A.; Loh, K. P.; Huang, W.; Yu, T. Visualizing the Anomalous Charge Density Wave States in Graphene/NbSe2 Heterostructures. *Adv. Mater.* **2020**, *32*, 2003746.
(20) Dreher, P.; Wan, W.; Chikina, A.; Bianchi, M.; Guo, H.; Harsh, R.; Mañas-Valero, S.; Coronado, E.; Martínez-Galera, A. J.; Hofmann, P.; Miwa, J. A.; Ugeda, M. M. Proximity Effects on the Charge Density Wave Order and Superconductivity in Single-Layer NbSe2. *ACS Nano* **2021**, *15*, 19430−19438.
(21) Tian, N.; et al. Dimensionality-driven metal to Mott insulator transition in two-dimensional 1T-TaSe2. *National Science Review* **2023**, nwad144.
(22) Illarionov, Y. Y.; Rzepa, G.; Waltl, M.; Knobloch, T.; Grill, A.; Furchi, M. M.; Mueller, T.; Grasser, T. The role of charge trapping in MoS2/SiO2 and MoS2/hBN field-effect transistors. *2D Mater.* **2016**, *3*, 035004.
(23) Illarionov, Y. Y.; Knobloch, T.; Jech, M.; Lanza, M.; Akinwande, D.; Vexler, M. I.; Mueller, T.; Lemme, M. C.; Fiori, G.; Schwierz, F.; Grasser, T. Insulators for 2D nanoelectronics: the gap to bridge. *Nat. Commun.* **2020**, *11*, 3385.
(24) Tsai, H.-S.; Liu, F.-W.; Liou, J.-W.; Chi, C.-C.; Tang, S.-Y.; Wang, C.; Ouyang, H.; Chueh, Y.-L.; Liu, C.; Zhou, S.; Woon, W.-Y. Direct Synthesis of Large-Scale Multilayer TaSe2 on SiO2/Si Using Ion Beam Technology. *ACS Omega* **2019**, *4*, 17536−17541.
(25) Samnakay, R.; Wickramaratne, D.; Pope, T. R.; Lake, R. K.; Salguero, T. T.; Balandin, A. A. Zone-Folded Phonons and the Commensurate-Incommensurate Charge-Density-Wave Transition in 1T-TaSe2 Thin Films. *Nano Lett.* **2015**, *15*, 2965−2973.
(26) Tsoutsou, D.; Aretouli, K. E.; Tsipas, P.; Marquez-Velasco, J.; Xenogiannopoulou, E.; Kelaidis, N.; Aminalragia Giamini, S.; Dimoulas, A. Epitaxial 2D MoSe2 (HfSe2) Semiconductor/2D TaSe2Metal van der Waals Heterostructures. *ACS Appl. Mater. Interfaces* **2016**, *8*, 1836−1841.
(27) Chen, M.-W.; Ovchinnikov, D.; Lazar, S.; Pizzochero, M.; Whitwick, M. B.; Surrente, A.; Baranowski, M.; Sanchez, O. L.; Gillet, P.; Plochocka, P.; Yazyev, O. V.; Kis, A. Highly Oriented Atomically Thin Ambipolar MoSe2 Grown by Molecular Beam Epitaxy. *ACS Nano* **2017**, *11*, 6355−6361.
(28) Ohtake, A.; Sakuma, Y. Two-Dimensional WSe2/MoSe2 Heterostructures Grown by Molecular-Beam Epitaxy. *J. Phys. Chem. C* **2021**, *125*, 11257−11261.
(29) Pierucci, D.; Mahmoudi, A.; Silly, M.; Bisti, F.; Oehler, F.; Patriarche, G.; Bonell, F.; Marty, A.; Vergnaud, C.; Jamet, M.; Boukari, H.; Lhuillier, E.; Pala, M.; Ouerghi, A. Evidence for highly p-type doping and type II band alignment in large scale monolayer WSe2/Se-terminated GaAs heterojunction grown by molecular beam epitaxy. *Nanoscale* **2022**, *14*, 5859−5868.
(30) Bjerkelund, E.; Kjekshus, A.; Nilsson, A.; Sandstron, J.; Theorell, H.; Blinc, R.; Pausak, S.; Ehrenberg, L.; Dumanovic, J. On the Structural Properties of the Ta1xSe2 Phase. *Acta Chem. Scand.* **1967**, *21*, 513−526.
(31) Horiba, K.; Ono, K.; Oh, J. H.; Kihara, T.; Nakazono, S.; Oshima, M.; Shiino, O.; Yeom, H. W.; Kakizaki, A.; Aiura, Y. Charge-density wave and three-dimensional Fermi surface in 1T-TaSe2 studied by photoemission spectroscopy. *Phys. Rev. B* **2002**, *66*, 073106.
(32) Hattori, K.; Ishihara, K.; Miyatake, Y.; Matsui, F.; Takeda, S.; Daimon, H.; Komori, F. GaP(111)reconstructed surface studied with STM and LEED. *Surf. Sci.* **2003**, *525*, 57−65.

https://doi.org/10.1021/acs.nanolett.3c02813
Nano Lett. 2023, 23, 9413−9419

(33) Wu, Z.; Bu, K.; Zhang, W.; Fei, Y.; Zheng, Y.; Gao, J.; Luo, X.; Liu, Z.; Sun, Y.-P.; Yin, Y. Effect of stacking order on the electronic state of 1T-TaS2. *Phys. Rev. B* **2022**, *105*, 035109.
(34) Liu, L.; et al. Direct identification of Mott Hubbard band pattern beyond charge density wave superlattice in monolayer 1T-NbSe2. *Nat. Commun.* **2021**, *12*, 1978.
(35) Song, X.; et al. Atomic-scale visualization of chiral charge density wave superlattices and their reversible switching. *Nat. Commun.* **2022**, *13*, 1843.
(36) Lin, M.-K.; Hlevyack, J.; Chen, P.; Liu, R.-Y.; Mo, S.-K.; Chiang, T.-C. Charge Instability in Single-Layer TiTe2Mediated by van der Waals Bonding to Substrates. *Phys. Rev. Lett.* **2020**, *125*, 176405.
(37) Zhang, W.; Wu, Z.; Bu, K.; Fei, Y.; Zheng, Y.; Gao, J.; Luo, X.; Liu, Z.; Sun, Y.-P.; Yin, Y. Reconciling the bulk metallic and surface insulating state in 1T-TaSe2. *Phys. Rev. B* **2022**, *105*, 035110.
(38) Lin, H.; Huang, W.; Zhao, K.; Qiao, S.; Liu, Z.; Wu, J.; Chen, X.; Ji, S.-H. Scanning tunneling spectroscopic study of monolayer 1T-TaS2 and 1T-TaSe2. *Nano Res.* **2020**, *13*, 133−137.
(39) Baffou, G.; Mayne, A. J.; Comtet, G.; Dujardin, G. State selective electron transport through electronic surface states of 6H-SiC(0001)-3 × 3. *Phys. Rev. B* **2008**, *77*, 165320.
(40) Nguyen, T. H.; Mahieu, G.; Berthe, M.; Grandidier, B.; Delerue, C.; Stiévenard, D.; Ebert, P. Coulomb Energy Determination of a Single Si Dangling Bond. *Phys. Rev. Lett.* **2010**, *105*, 226404.
(41) Miccoli, I.; Edler, F.; Pfnür, H.; Tegenkamp, C. The 100th anniversary of the four-point probe technique: the role of probe geometries in isotropic and anisotropic systems. *J. Phys.: Condens. Matter* **2015**, *27*, 223201.

https://doi.org/10.1021/acs.nanolett.3c02813
Nano Lett. 2023, 23, 9413−9419